

Two-dimensional atomically bridged nanoporous silicate-based membranes for gas separation

Présentée le 9 juillet 2021

Faculté des sciences de base
Chaire Gaznat en procédés de séparation avancés
Programme doctoral en chimie et génie chimique

pour l'obtention du grade de Docteur ès Sciences

par

Mostapha DAKHCHOUNE

Acceptée sur proposition du jury

Prof. B. Smit, président du jury
Prof. K. V. Agrawal, directeur de thèse
Prof. J. Caro, rapporteur
Prof. Z. Lai, rapporteur
Prof. K. Sivula, rapporteur

To my parents
Saida El Qaidi and Hassan Dakhchoune

Acknowledgment

I would like to express my deep gratitude to Prof. Kumar Varoon Agrawal for having put his faith in me by accepting me as his second Ph. D. at the LAS laboratory back in December 2016. Prof. Kumar has drawn for me a real example of how cutting-edge research is performed and seeded in me the curiosity of the research. I had some dark moments where I really could not see the light at the end of the tunnel, but the strength with which he encouraged me in seeing positiveness and try more, motivated me to advance further and harvest happiness upon the results were coming true. He has been an excellent supervisor, and his great scientific advice was vital during the Ph. D. journey. I am also thankful for his thoughtful career support.

I am very grateful to Prof. Jürgen Caro, Prof. Berend Smit, Prof. Zhiping Lai, and Prof. Kevin Sivula for serving as the jury committee for my Ph. D. thesis.

Unique and special gratitude goes to Dr. L. F. Villalobos (Paco), who has accompanied me during these four years and has fully supported me scientifically. On the personal side, I cannot forget the great coffee/**salty** breaks that we had together where great ideas were being conceived. Speaking of salt, I must mention the mind behind it, and the name of Dr. D. J. Babu (now Deepu Sar) comes up. His brilliant scientific guidance and companionship are a must-have for any lab. The time spent with Dr. Huang Shiqi is indelible from the very first set up of the lab until her last day in the lab. Her strength, courage, and perseverance in research are a real example for all women and men. Thanks to Dr. Guangwei He for being always there at any time to help me turn off ovens, switch gases, etc., besides being an excellent scientist together with his wife, Prof. Jing Zhao. Thanks to Mojtaba Rezaei for sharing great talks full of hope when hope in our projects was not there at all. Thanks to Mohamad Tohidi, even if he spent only little time with us in Sion, we bonded very strongly that he was already pouring salt in your coffee with nonchalance the few times he was coming to Sion. Special thanks go to our musician Wan-Chi Lee with whom my Chinese language improved remarkably up to recognizing the 4 Chinese accents. I'll never forget when I called her on the phone pretending to be the IT guy (of course with Deepu as master poppit) and blaming her for using unlicensed game versions (for the record, it is not true). I have to specially thank Kuang-Jung from the Taiwanese community with whom I have spent wonderful moments and had great talks, especially those related to large areas. Thanks to my great 2D sub-group mate Heng-Yu Chi, a great chemist besides having the superpower of finding all the possible typos in the manuscript (Chapeau). Thanks to Shaoxian Lee, who delights us with only his forehead in the zoom-group meetings. Thanks to my official french teacher, Luc Bondaz, for the time spent together around Sion doing language Tandems at night. A special thank you goes to Dr. Nikunj Dudani, a reference

friend during my stay here in Switzerland. Speaking of vital friends, I must mention my housemate, Dr. Pranit Iyengar, with whom I have shared sweet moments (watching Friends together) and sour moments (complaining about the Ph.D. life and how to handle frustration).

I could go on and on picking on each of the great scientists that have surrounded me and contributed to making this journey enjoyable and rewarding both scientifically and personally. For this, I would like to collectively thank all the other lab members Dr. Marina Micari, Piotr Gebolis, Dr. Jian Hao, Dr. Liu Qi, Dr. Cédric Van Goethem, Dr. Kangning Zhao and Dr. Xuekui Duan. Finally, many thanks to our ex. secretary Catherine Regamey who has made the transition from Italy and Switzerland very smooth and always supported me with all the needed in Valais. Many thanks also to Delphine Echenard, who got straightaway on board, making Cathie's departure less painful.

All the scientific work would not have been possible without the help of the platform scientist Dr. Pascal Schouwink, Dr. Emad Oveisi, Dr. Mounir Mensi, Dr. Aurélien Bornet, and Dr. Claudia Avalos.

Many thanks go to the mechanical workshop team Stéphane Voeffray and Robin Délèze who accommodated any possible project unimaginable. Together with them, I would like to thank Fabio Taddei, the IT team Cédric Passerini and Jean Perruchoud, and the chemical store pioneers Laurent Seydoux and Annabelle Coquoz. Finally, I want to thank the whole janitorial team, whose contribution to learning French was considerable.

I am very grateful to my Italian friends Cipri, Franci, Fosso, and Briki for driving over a thousand kilometers to attend my Ph. D. defense.

I am very grateful to Beatrice Innocenti, who has been supporting and baring me for the last ten years demonstrating to be the one-of-a-kind life companion that I would have asked for.

All my possible energies go to sincerely thank my family for their unconditioned love and support.

Abstract

The synthesis of molecular-sieving two-dimensional zeolitic membranes by the assembly of crystalline building blocks without resorting to the secondary growth process is highly desirable. The precise pore size for molecular sieving, ultrathin thickness, and high thermal and chemical stability make zeolite nanosheets attractive for a number of gas separation applications. However, preparing ultrathin membranes in a scalable way can only be achieved with a secondary growth-free approach, and this remains a grand challenge. Overall, there are four major drawbacks for the synthesis and scale-up of these type of membranes: i) the preservation of the crystallinity of the nanosheets after exfoliation; ii) the non-reproducibility of the secondary growth method; iii) the development of low-cost and scalable support for the ultrathin films, and iv) the implementation of a facile and scalable membrane fabrication methods.

This dissertation focuses on the development of ultrathin zeolitic membranes employing 0.8-nm-thick crystalline nanosheets from the sodalite zeolite precursor RUB-15 that hosts hydrogen-sieving six-membered rings (6-MRs) of SiO_4 tetrahedra. The hydrothermal synthesis of the layered RUB-15 followed by the cation exchange chemistry to increase the d spacing between the layers facilitated the polymer blend-based exfoliation of the layered precursor leading to the first report of highly crystalline RUB-15 nanosheets where the 6-MRs were clearly visible with high-resolution transmission electron microscopy. Highly dispersed RUB-15 nanosheets in polar solvents allowed their facile assembly *via* vacuum filtration into 100-300 nm-thick continuous films on top of porous supports. Detailed transport studies of such as-filtered membranes revealed the presence of two different transport pathways for gas molecules: 1) the H_2 -selective 6-MRs and 2) the interlayer galleries, which allow He, H_2 , and CO_2 molecules to permeate freely. The latter dominated the transport in as-filtered films, which displayed a molecular cutoff of 3.6 Å yielding a H_2/N_2 and H_2/CH_4 selectivities above 20. Non- H_2 -selective pathways [interlayer galleries] were eliminated by topotactic condensation of the terminal silanol groups. Upon calcination, defective $[\text{SiO}_3][\text{O}^-]$ units were converted into fully coordinated silicon tetrahedra $[\text{SiO}_4]$, diminishing the interlayer gaps and yielding H_2/CO_2 selectivities above 100, demonstrating the effective suppression of the interlayer transport and highlighting the selective role of the 6-MRs in the temperature range 25-300 °C. This is the first report of high-performance two-dimensional zeolitic membranes without the need for the secondary growth process able to efficiently sieve light gases.

The scale-up of thin supported membranes relies on the quality of the underlying support. A scalable polymeric support was developed to support uniform RUB-15 films. The support was synthesized *via* non-solvent induced phase separation (NIPS) of polybenzimidazole AM Fumion® polymer on a low-cost stainless steel mesh. The support possesses a smooth surface, high porosity, and thermal and mechanical stability. However, the high calcination temperature of RUB-15 membranes prohibits its employment as support. For this, two new routes for removing the residual template and surfactant were developed to enable the use of the polymeric PBI-AM supports for the future scale up of RUB-15 membranes. In-situ XRD studies revealed that a mild calcination temperature of 330 °C was sufficient to eliminate the organic molecules trapped in the gallery space and seal the interlayer unselective pathways if it was done for a sufficient amount of time. Alternatively, we developed a room-temperature, liquid-extraction-based process where diluted solutions of acetic acid were filtered on a pre-filtered film to remove the organic molecules in the gallery spacings. The effectiveness of the new calcination process together with the PBI-AM support yielded molecular sieving membranes capable of separating H₂/CO₂ with selectivities in the range of 20-35 and permeances up to 400 GPU under testing temperatures in the range 25-250 °C. Preliminary permeation results on the membranes activated with *in-situ* acid treatment displayed similar promising results. The key features of the developed support would enable its application in a wider range of membrane applications where self-standing membranes cannot be synthesized.

Finally, a nanoporous carbon- (NPC) based membrane was developed, which displayed extremely large H₂ permeance with a Knudsen H₂/CO₂ selectivity. A techno-economic analysis was performed to evaluate the potential impact on the overall cost for pre-combustion carbon capture using different membrane stage configurations. Combining the ultra-permeable carbon-based membrane with the ultra-selective RUB-15 membrane in consecutive stages offer an attractive and versatile solution for pre-combustion carbon capture. Besides their promising application in pre-combustion carbon capture, the carbon-based membranes were ideal mechanical reinforcements for the crack-free synthesis of nanoporous single-layer graphene membranes.

Table of Contents

Acknowledgment	III
Chapter 1. Introduction.....	1
1.1. Thermodynamics of separations: Challenges and opportunities	1
1.2. Membrane separation principles.....	5
1.3. Industrial membranes for gas separations	7
1.4. Solution-diffusion transport.....	8
1.5. Nanoporous and nanochannel transports.....	9
1.6. Synthesis and separation mechanism of 2D nanosheets.....	10
1.6.1. Transport through nanoporous zeolites	11
1.6.2. Transport through nanoporous MOFs	14
1.6.3. Transport through graphene oxide nanochannels	17
1.7. Opportunities for zeolite membranes compared to polymeric membranes	19
1.8. Zeolites: Limitations and opportunities	21
1.9. Zeolites for H ₂ /CO ₂ separation	22
1.10. Importance of the support for commercialization of zeolitic membranes	24
1.11. Process simulation	27
1.12. Thesis outline.....	28
Chapter 2. Gas-sieving zeolitic membranes fabricated by condensation of precursor nanosheets	31
1. Introduction	31
2. Methods	33
2.1. Materials	33
2.2. Synthesis of layered RUB-15.	33
2.3. Swelling of RUB-15 layers	33
2.4. Exfoliation of swollen RUB-15	34
2.5. Purification of exfoliated RUB-15 nanosheets by DGC.....	34
2.6. Acid-treatment of purified RUB-15 nanosheets	34
2.7. Assembly of nanosheets into a membrane	34
2.8. Preparation of calcined RUB-15-based nanosheets membranes	35
2.9. Preparation of calcined RUB-15-based nanosheets membranes using diluted sol-gel derived silica solution.....	35
2.10. Gas permeation.....	35
2.11. Ab-initio calculations.	37
2.12. Characterization.....	37
3. Results and discussions	39
3.1. Gas diffusion through 6-Membered Si-tetrahedra rings	39
3.2. Synthesis of single layer RUB-15 nanosheets	42

3.3. Nanosheets membrane assembly and condensation	53
4. Conclusions	66
Appendix I.....	66
Chapter 3. Gas-sieving zeolitic membranes on scalable polymeric support obtained with mild calcination temperatures and <i>in-situ</i> acidic detemplation	68
1. Introduction	69
2. Methods	72
2.1. Materials	72
2.2. Layered RUB-15 hydrothermal synthesis.	72
2.3. CTAB-based swelling of RUB-15 layers.	72
2.4. RUB-15 exfoliation.	73
2.5. Nanosheets extraction from polymeric matrix.	73
2.6. Sulfuric acid treatment of RUB-15 nanosheets	73
2.7. PBI-AM support preparation	73
2.8. Assembly of nanosheets into a membrane with mild calcination temperature.....	74
2.9. Assembly of nanosheets into a membrane with acidic extraction	74
2.10. Gas permeation.....	74
2.11. Characterization.....	75
3. Results and discussions	75
3.1. PBI-AM support fabrication and assembly of RUB-15 nanosheets	75
3.2. <i>In-situ</i> XRD of mild thermal detemplation.....	80
3.3. Gas separation RUB-15@PBI-AM calcined at 330 °C	83
3.4. <i>In-situ</i> detemplation of RUB-15@PBI-AM membranes	84
4. Conclusions	87
Appendix I.....	88
Chapter 4. Block-copolymer templated nanoporous carbon membrane for ultrafast hydrogen purification	89
1. Introduction	89
2. Methods	91
2.1. Synthesis of nanoporous carbon film	91
2.2. Characterization.....	92
2.3. Gas permeation measurements	92
2.4. Method for techno-economic analysis.....	93
2.4.1. Model.....	93
2.4.2. Inputs and parameters	96
3. Results and discussions	97
3.1. Fabrication of nanoporous carbon membranes.....	97
3.2. NPC morphology as a function of turanose/copolymer ratio	100
3.3. Chemical composition and structure of the NPC film.....	101

3.4. Gas transport properties from NPC membrane	104
3.5. Interlamellar liquid transport.....	106
3.6. Techno-economic analysis for pre-combustion carbon capture	109
4. Conclusions	113
Chapter 5: Summary and perspective.....	114
1. Summary of the thesis	114
2. Perspective.....	118
References.....	123

Chapter 1. Introduction

Adapted with permission from Mostapha Dakhchoune, Two-dimensional Material Membranes for Gas Separation, Chimia, 74, 4, 2020, 263-269. <https://doi.org/10.2533/chimia.2020.263>. Copyright © M. Dakhchoune 2020.

1.1. Thermodynamics of separations: Challenges and opportunities

Why do we need to spend energy to separate chemicals?

The answer can be found by understanding the thermodynamics of mixtures. The Gibbs free energy G , of a multicomponent mixture of c components, is a function of temperature T , pressure P , and each species mole number N_i with $i=1 \dots c$, as shown in Eq. 1-2:

$$dG = \left(\frac{\partial G}{\partial T}\right)_{P, N_i} dT + \left(\frac{\partial G}{\partial P}\right)_{T, N_i} dP + \sum_{i=1}^c \left(\frac{\partial G}{\partial N_i}\right)_{T, P, N_{j \neq i}} dN_i \quad (1)$$

$$dG = -S dT + V dP + \sum_{i=1}^c \bar{G}_i dN_i \quad (2)$$

Where \bar{G}_i is the partial molar Gibbs energy of i^{th} component.

The total Gibbs free energy at constant pressure and temperature of a mixture with two components is given by Eq. 3:

$$G = n_1 \bar{G}_1 + n_2 \bar{G}_2 \quad (3)$$

where n_i is the number of moles of the i^{th} component. For simplicity, let us consider an ideal gas component mixture. The molar Gibbs energy of an ideal gas is expressed by Eq. 4:

$$\bar{G}_i = \bar{G}_i^\circ + RT \ln \frac{P}{P^\circ} = \mu_i = \mu_i^\circ + RT \ln \frac{P_i}{1 \text{ bar}} \quad (4)$$

where \bar{G}° is the standard molar Gibbs free energy at pressure P° (e.g., for an ideal gas is 1 bar), P is the pressure of the system P_i is the partial pressure μ_i is the chemical potential μ_i° is the standard the chemical potential at 1 bar, and R is the ideal gas constant. All these quantities are specific to the i^{th} component.

A system of two ideal gases 1 and 2 at the same temperature and pressure possess an initial ($t=0$) Gibbs free energy expressed by Eq. 5:

$$G_{t0} = n_1(\mu_1^\circ + RT \ln P) + n_2(\mu_2^\circ + RT \ln P) \quad (5)$$

When the two gases are mixed together, their partial pressure decreases and, in the final state ($t=f$), the Gibbs free energy is given by Eq. 6:

$$G_{tf} = n_1(\mu_1^\circ + RT \ln P_1) + n_2(\mu_2^\circ + RT \ln P_2) \quad (6)$$

Finally, the Gibbs free energy of the mixing $\Delta_{mix} G$, is obtained by Eq. 7:

$$\Delta_{mix} G = G_{tf} - G_{t0} = n_1 RT \ln x_1 + n_2 RT \ln x_2 \quad (7)$$

where x_i is the molar fraction of the i^{th} component. By definition, the molar fraction is a quantity ≤ 1 , which means that the effect of mixing results in a negative Gibbs free energy of mixing. Note that in the case of non-ideal systems, the molar fractions x_i will be replaced by the activity a_i , of the species, which is related to the molar fraction by the activity coefficient γ_i , according to Eq. 8:

$$a_i = \gamma_i(T, P, \underline{x}) x_i \quad (8)$$

where \underline{x} is the molar fraction of each component.

The above derivation shows how the mixing of components is a spontaneous process contrarily to the separation process, which requires the input of a minimum theoretical energy into the system to overcome the thermodynamic limitations. Understanding the minimum amount of energy required to separate a given mixture provides a baseline for comparison between new technologies and helps to guide future research efforts towards less energy-demanding applications. The minimum theoretical energy required for a given separation is obtained when operated under the condition of “reversible thermodynamic process”, which means that the energy to be paid is equal in magnitude to the energy of mixing ($\Delta_{mix} G$) with the opposite sign.¹ Actual chemical separation plants do not operate under the assumption of “reversible thermodynamic process”, consuming more energy than the theoretical minimum values.

Industrial separation processes have a remarkable energy and environmental footprint and account for more than 20% of all in-plant industrial energy use.² Thermally-driven separations (distillation, drying, evaporation) are well established in the chemical industry; however, they are highly energy-intensive since they rely on the latent heat of vaporization of the components in the mixture. Distillation, drying, and evaporation account for 49%, 20%, and 11% of industrial energy consumption, respectively.² This is due to the intrinsic inefficiency of thermal processes. For instance, thermodynamic distillation efficiency ranges from 18% for the air separation (cryogenic distillation) to 12% in crude oil refining, and it is only 5% in olefin/paraffin separation (C_2 and C_3 separations).^{3,4}

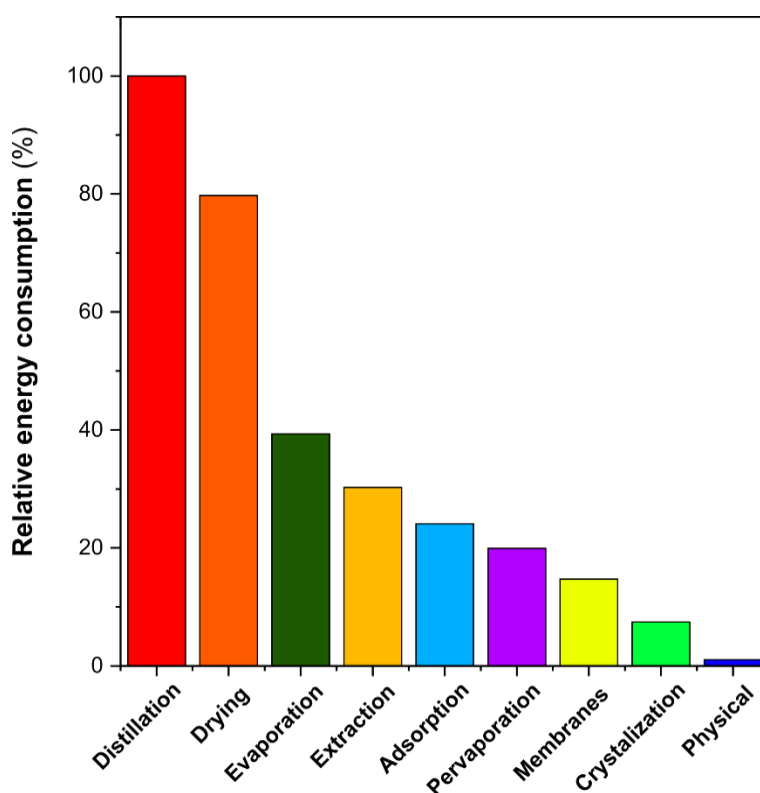


Figure 1.1. Relative energy use by various separation technologies. Data obtained from reference [2].

The independence from thermally-driven separation would cut down the cost of separation, which currently accounts for 40-70% of both capital and operating costs in the industry.^{5,6} Figure 1.1 reports the major separation technologies, which can be classified in two main categories based on the presence/absence of phase-change during the separation. Higher energy consumptions are accompanied by phase change, which is common in thermally-driven separations, while a decrease in consumption is witnessed with single-phase separations.

The scarcity of resources, together with global climate change, triggered extensive research towards the implementation of energy-efficient separation processes. Membrane-based separations are an energy-efficient technology predicted to drastically cut down the separation cost by up to 90% when compared to conventional distillation.^{7,8} They possess inherent advantages such as being a continuous process, have small capital cost, are environmentally friendly, have a small footprint due to their modular design, and generally do not present waste streams.

Despite the potential advantages of membranes-based separations compared to conventional distillation, the complete replacement of the latter with membranes is still far from being possible. For instance, distillation is capable of fractioning crude oil into a myriad of compounds with extremely different viscosities in the presence of impurities and of chemically aggressive substances, which would make the implementation of membranes very challenging. Moreover, current materials used for membranes are generally incapable of sieving multiple components but are rather optimized for a specific binary mixture.⁸

A great example that is worth mentioning and learning from, where membranes have largely replaced thermally-driven separations, is water desalination. The increasing scarcity of drinkable water had become one of the most serious global challenges, with one-third of the world's population already lacking access to clean water. This number is expected to increase to 75% in the following decades.⁹ The need to implement new energy-efficient technologies to produce fresh water has led to remarkable developments in the last decades in the field of membrane-based reverse osmosis (RO), where seawater is being pressurized above its osmotic pressure against a semi-permeable polymeric membrane capable of separating water molecules by retaining the hydrated salt ions. The success of RO membranes and their worldwide implementation is due to lower costs per m³ of fresh water produced in comparison to the evaporation-based process.¹ The theoretical lowest amount of energy needed to produce fresh water from the sea is again given by the Gibbs free energy of mixing, and it is a function of the osmotic pressure of the salt-water solution Π_s , and the water molar volume \bar{V}_w , as shown in Eq. 9:¹

$$w_{min} = -RT \ln(\gamma_w x_w) = \Pi_s \bar{V}_w \quad (9)$$

For instance, the minimum theoretical specific energy needed for a 50% water recovery from seawater (3.5 w/w% NaCl and 15 °C) is 1.06 kWh/m³, while current reverse osmosis plants require only ~2 kWh/m³ under the same conditions, which explains their worldwide spread.¹

1.2. Membrane separation principles

A membrane is a semi-permeable layer, which favors the transport of one component over others based on different mechanisms and under different driving forces that vary depending on the separation process (pressure, temperature, concentration, electrical potential, etc.). A feed containing a mixture of components is passed on top of the semi-permeable layer, which allows the preferential transport of one or more components across the membrane generating a permeate stream, while the non-permeated feed results in a retentate stream, which can be further processed (Figure 1.2a).

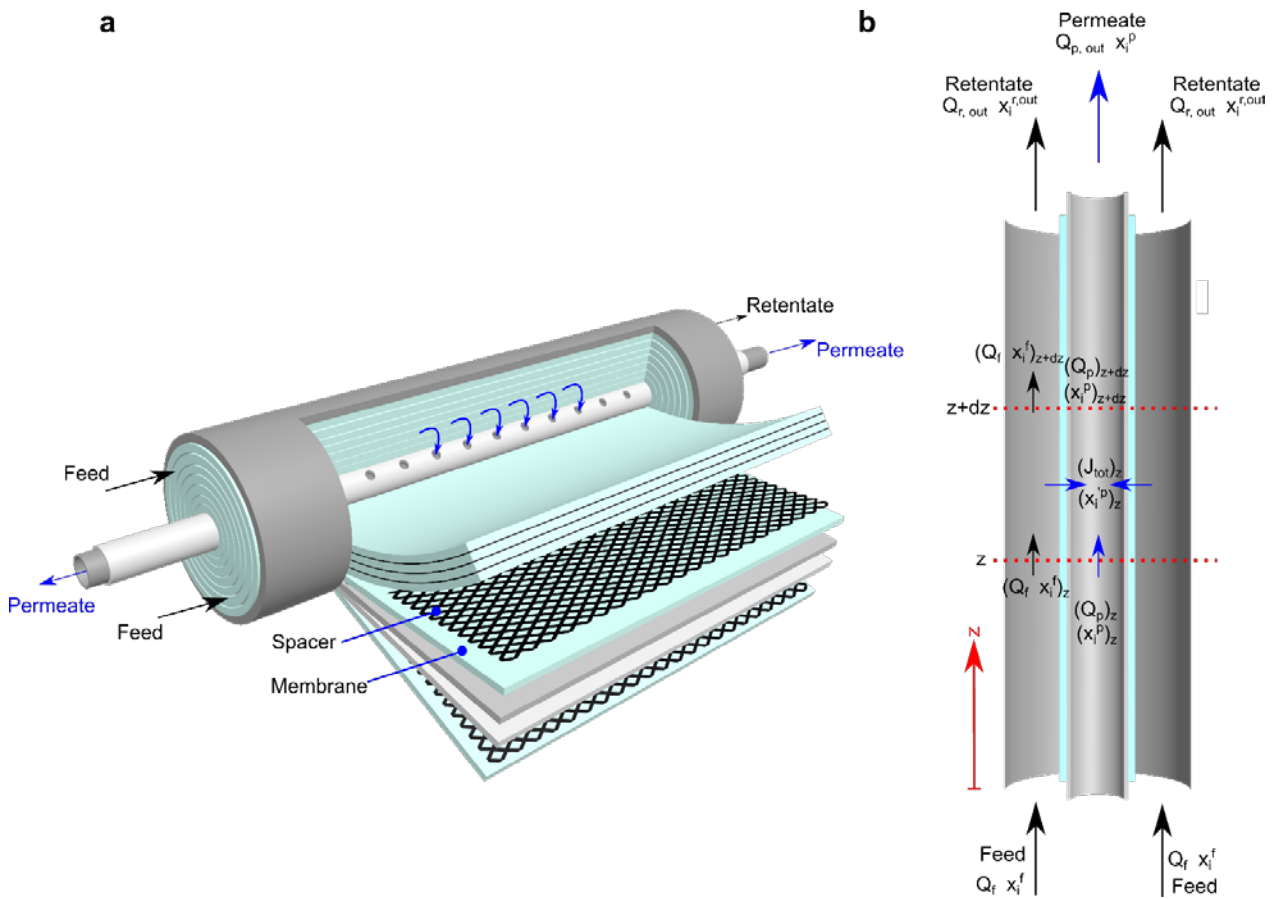


Figure 1.2. a) Schematic illustration of a spiral wound membrane module. b) Schematic representation of streams in a membrane element with feed, permeate, retentate, and their relative compositions in a co-current configuration. Where x_i is the composition of the component of interest, r, f, and p subscripts/superscripts are related to retentate, feed, and permeate, respectively. J_{tot} is total flux ($\text{mol m}^{-2} \text{s}^{-1}$) permeating the membrane between z and $z+dz$ sections.

The mass transport rate of a component across a membrane can be described as a function of the driving force across the membrane thickness and the permeance (i.e., the flux of a component normalized by the membrane area and the transmembrane pressure) according to Eq. 10:

$$J = -\mathbf{P} \frac{dX}{dz} \quad (10)$$

where J is the flux across the membrane, \mathbf{P} is a phenomenological coefficient expressing the permeance of the membrane, and $\frac{dX}{dz}$ is the variation of the driving force along with the membrane thickness.^{10,11} The driving force is dependent on the separation process and can be expressed in terms of hydrostatic pressure P , chemical potential μ_i , concentration C_i , activity a_i , partial pressure p_i , fugacity f_i , and electrochemical potential μ_i^E .

For gas separation, the driving force to transport gaseous species across the membrane is the chemical potential difference between feed and permeate. The difference in the chemical potential corresponds to a gradient in the fugacity of gases (or partial pressure in the case of ideal assumption), which can be originated either *via* feed compression or *via* vacuum of the permeate side.

The constitutive flux equations across the membrane for a gas mixture at any section z of the membrane (Figure 1.2b) is given by Eq. 11-13:

$$J_i = \mathbf{P} (P_f x_i^f - P_p x_i'^p) \quad \forall i = 1, \dots, N_c \quad (11)$$

$$J_i = J_{tot} x_i'^p \quad \forall i = 1, \dots, N_c \quad (12)$$

$$J_{tot} = \sum_{i=1}^{N_c} J_i \quad (13)$$

where \mathbf{P} is the permeance ($\text{mol m}^{-2} \text{s}^{-1} \text{Pa}^{-1}$) and P_f and P_p are the feed and permeate pressures, respectively. x_i^f and $x_i'^p$ are the feed and permeate compositions at the section z . J_i is the molar flux of the i^{th} component, while J_{tot} is the total flux. Equations 11-13 applied on an infinitesimal membrane volume $A_m dz$ together with the stoichiometric identities and mass balances describe the overall membrane system and identify streams flow rates and relative composition, and the membrane area needed for a given target separation.¹²

1.3. Industrial membranes for gas separations

The major breakthrough in membrane-based separations that allowed the development, twenty years later, of the first membrane for gas separation was achieved by Loeb and Sourirajan in 1961. Researchers struggled in achieving adequate fluxes through thick polymeric films, and when reducing the film thickness, an increase of flux was possible at the expense of decreased selectivities. Loeb and Sourirajan achieved by a simple method the synthesis of asymmetric membranes where a very thin, selective layer was formed atop of a thicker layer where the transport resistance was small.¹³

The development of asymmetric membrane technology allowed Monsanto company to launch the first membrane for gas separation based on a very thin polysulfone selective layer coated with a silicon layer to block unselective defects within the polymeric layer. The developed hollow fiber membrane was commercialized as PRISM membrane and adopted to tune the H₂ : CO₂ ratio in the syngas synthesis.^{14,15}

Following PRISM membranes, remarkable development was achieved in the membrane-based gas separation field, and its market is nowadays estimated at 1-1.5 billion/year. Separation of N₂ from air and the sweetening of natural gas (removal of CO₂ from natural gas) are the two major applications of this technology and account for more than two-thirds of the whole market.¹⁶

Table 1.1. Current industrial membranes for gas separation. Data obtained from Ref. [17].

Gas	Membranes		Selectivity	Permeance (GPU) ^a
N₂/Air	Polysulfone (Air products)		3-6	5-50
Nitrogen production	Polyimide (Air Liquide)	O ₂ /N ₂		
	Polycarbonate (Generon)			
	poly(phenylene oxide) (Aquila)			
CO₂/CH₄	Cellulose acetate (UOP)	CO ₂ /CH ₄	10-15	100-200
Natural gas sweetening				
H₂/N₂ or NH₃	Polysulfone (Air products)	H ₂ /N ₂	50-150	80-200
Hydrogen separation	Polyimide (Air Liquide)			
hydrocarbons (C ₃ /N ₂) (organic vapor recovery)	Silicon rubber (PDMS) (MTR)	C ₃ /N ₂	5-20	500-5000

^a 1 GPU = $3.3 \times 10^{-10} \text{ mol m}^{-2} \text{ s}^{-1} \text{ Pa}^{-1}$

Table 1.1 summarizes the major industrial applications of membranes, together with their performance of permeance and gas-pair selectivities.¹⁸ The current industrial market is dominated by polymeric membranes due to their ease of large-scale processing, which allows for high-surface areas per unit of volume (spiral wound configurations, Figure 1.2a) and low costs per m² of membrane area. However, polymeric membranes display moderate selectivities, low permeances, as well as poor chemical and thermal stability.¹⁹ Their low performance is due to their transport based on the solution-diffusion transport mechanism.

1.4. Solution-diffusion transport

Transport of gas molecules across polymeric membranes takes place *via* the solution-diffusion mechanism, which is summarized by Eqs. 14-15:²⁰

$$P_A = D_A S_A \quad (14)$$

$$\alpha_{(A/B)} = \frac{P_A}{P_B} = \left(\frac{D_A}{D_B} \right) \left(\frac{S_A}{S_B} \right) = \alpha_{D(A/B)} \alpha_{S(A/B)} \quad (15)$$

where P_A , D_A , and S_A are the permeability (permeability = permeance x membrane thickness), diffusivity, and solubility of component A within the polymeric phase, respectively. The subscript B refers to component B and $\alpha_{(A/B)}$ is the selectivity between components A and B (Note that Eq. 14-15 are valid when upstream pressure and concentration are much higher than the downstream ones). The solution-diffusion mechanism consists of the sorption of gas molecules in the upstream side of the membrane into the polymeric phase, followed by the diffusion along the direction of the driving force gradient, and, finally, the desorption from the polymer into the gas phase. The permeability and selectivity of the membrane are a function of a kinetic parameter, D, and a thermodynamic parameter, S. When molecules with similar solubility coefficients are separated, their selectivity in the polymer is mainly determined by the difference in their kinetic diameters. For instance, O₂/N₂ have low solubilities in polymers and present only 0.18 Å difference in kinetic diameter (O₂ = 3.46 Å, N₂ = 3.64 Å), which results in polymers with low selectivities (e.g., 3-6, Air Liquide), while for the separation of H₂/CH₄ where the difference is 0.9 Å (H₂ = 2.9 Å, CH₄ = 3.8 Å) polymers with selectivities up to 200 have been reported.²¹

Overall, polymeric membranes suffer from a trade-off between permeance and selectivity, where the increase of one of them happens at the expense of the other. Moreover, change in the fractional

free volume (FFV) of the polymer with time (aging), and the plasticization effects due to absorbed molecules (e.g., CO₂) limit their performance.^{22,23}

1.5. Nanoporous and nanochannel transports

Most inorganic membranes such as zeolites, metal-organic frameworks (MOFs), metals, etc. transport and separate molecules based on their kinetic diameters *via* a molecular sieving mechanism (other mechanisms such as surface diffusion can occur especially at low temperatures) where the molecular size difference plays a major role in the final selectivity between molecules. With micropores in the range of 0.2-0.8 nm, inorganic membranes display superior performance in terms of permeance, selectivity, thermal, mechanical and chemical stability compared to conventional polymeric membranes.^{18,24} Despite their remarkable advantages, most inorganic membranes are still in the research and development stage. Their major limitations include high-specific membrane costs, low processability, and brittleness. Such limitations often require the fabrication of rigid and specialized porous supports compatible with the delicate inorganic selective layers, and the synthesis cost of the support accounts for the majority of the overall membrane cost.^{25,26}

Contrarily to polymeric membranes where the gas transport occurs within the polymer FFV, polycrystalline porous inorganic membranes (e.g., zeolites, MOFs) impart well-defined and crystalline porous channels where gas-sieving takes place. Nevertheless, the precise control and scalability of crystal nucleation and growth remain a grand challenge.²⁷ For this reason, the development of membrane materials that are easily processable into thin films with high-sieving performance is an essential step for the continuous and sustainable development of inorganic membranes.

The Nobel-prize-awarded discovery of graphene by Geim and Novoselov in 2004 triggered an extensive research interest in two-dimensional (2D) materials for gas and liquid separations.²⁸ Among these, 2D nanosheets-based membranes have steadily acquired increasing relevance. Their assembly as building blocks into thin films makes them promising candidates for the next generation of membranes. The atom- or few-atoms-thick nanosheets could lead to higher fluxes since they minimize the diffusional path that a molecule travels to cross the membrane thickness. Moreover, their in-plane crystalline structure with highly-ordered pore arrays ensures high size-sieving selectivity.²⁹

2D nanosheet-based membranes can be classified in two main categories based on their transport mechanism: i) intrinsically non-porous nanosheets, which rely on different strategies to finetune the selective interlayer spacings (graphene oxide GO and reduced graphene oxide rGO,³⁰ MXenes,³¹ transition metal dichalcogenides TMDs,³² and layered double hydroxides, or LHDs³³) (Figure 1.3a); and ii) porous nanosheets where the transport of the molecules occurs parallel to the nanosheet thickness and through their pores (nanoporous graphene,³⁴ zeolites,³⁵ MOFs,³⁶ covalent organic frameworks COFs,³⁷ and graphitic carbon nitrides³⁸) (Figure 1.3b).

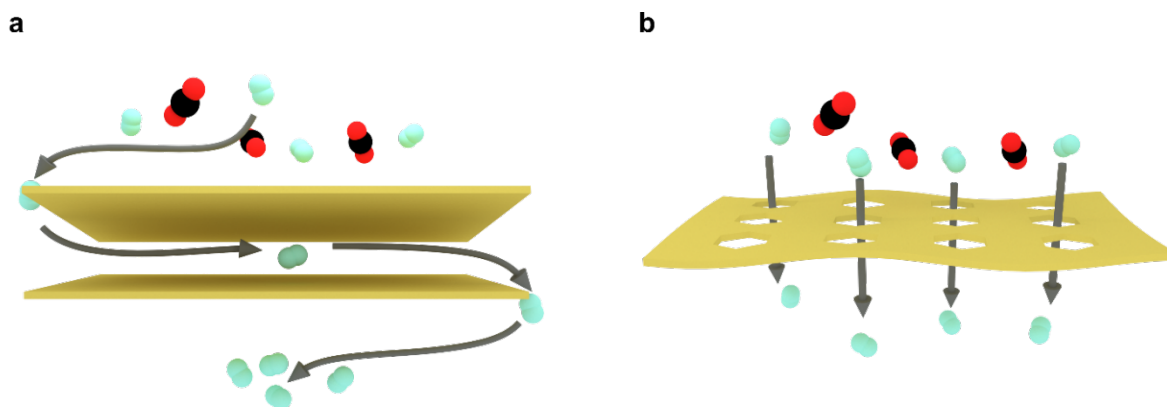


Figure 1.3. a) Non-porous nanosheets with molecular transport given by the finetuning of the interlayer spacing. b) Porous nanosheets where the transport occurs across the nanosheets through the porous framework.

1.6. Synthesis and separation mechanism of 2D nanosheets

The synthesis of 2D nanosheets with nanometer or sub-nanometer thickness will remarkably reduce the transport resistance with increased flux. Two major routes, top-down and bottom-up, are utilized to synthesize 2D nanosheets. The former relies on the difference between the in-plane and out-of-plane forces that keep atoms and layers together. Typically, weak Van der Waals interactions holding together stacked nanosheets can be overcome by different strategies such as ultrasound,³⁶ solvent-assisted exfoliation,³⁹ polymer intercalation coupled with external shear stress,³⁵ and freeze and thaw⁴⁰ exfoliation separating the single- or few-layered nanosheets. Restacking of the nanosheets, low exfoliation yields, and fragmentation represent some of the major drawbacks in the top-down strategy.⁴¹ The bottom-up route relies on the suppression of the orthogonal crystal growth either by reaction nanoconfinement (e.g., air-liquid and liquid-liquid interfaces,^{42,43} nanoreactors⁴⁴) or by the use of third-party molecules (e.g., surfactants), which direct the growth in the in-plane domains.⁴⁵ The need for substrates, interfaces, and surfactants hinders mass production in the bottom-up approach. Moreover, the resulting nanosheets are still relatively thick (5–50 nm).⁴⁶

The selection of either route depends on which features the nanosheets need to possess for the desired application. Both synthesis strategies can originate lateral sizes in the order of hundreds of μm ,^{43,47} and their assembly into membranes can be performed by several methods, such as pressure-assisted filtration,⁴⁸ spray coating,⁴⁹ casting,⁵⁰ layer-by-layer deposition,⁵¹ and hot-drop coating.⁵²

The selective pathways that the gas molecules travel through vary depending on the structural nature of the nanosheets, which can be porous (e.g., zeolites, MOFs, COFs, etc.) or nonporous (e.g., GO, TMDs, LHDs, etc.). The controlled stacking of the latter type of nanosheets produces nanochannels due to the interlayer repulsive interactions. The intercalation of guest molecules between the layers, besides creating empty interlayer pathways for the molecules, can facilitate their transport based on the different affinity between the guest molecules and the species being separated.^{53,54} Although membranes of a few nanometers in thickness can be fabricated, the distance traveled by a molecule in crossing the whole membrane thickness can be orders of magnitude longer, resulting in lower fluxes.³⁰ To shorten the molecule transport pathways, the use of intrinsically porous nanosheets allows perpendicular transport along the gas gradient concentration minimizing the transport resistance and resulting in higher productivity.

The synthesis of nanosheets-based membranes for gas separation has been successfully demonstrated for both porous and non-porous nanosheets, and major advancements for few representative materials will be highlighted in the next section for both types of channels.

1.6.1. Transport through nanoporous zeolites

Zeolites are alumino-silicates with tetrahedrally connected SiO_2 networks forming well-defined crystalline domains with pores ranging from 0.25 to more than 1 nm.⁵⁵ Zeolites have been used in many chemical processes because of their unique properties of well-defined pores, high porosity, chemical, and mechanical stability.⁵⁶ However, zeolites have only been applied as membranes in the context of organic stream dehydrations using LTA-type zeolite.^{57–59} To circumvent crystallization defects in polycrystalline zeolite membranes, thicknesses of up to tens of micrometers are required, which result in much higher transport resistances. In this regard, the use of 2D zeolite nanosheets as building blocks for gas separation has attracted much attention as high-performance molecular sieving membranes. Nanosheet crystallinity, uniform thickness, and high aspect ratio are vital requirements for the successful fabrication of high-performance membranes. Synthesis of nanosheets using conventional top-down solution-based exfoliation techniques (e.g., sonication) could not meet these criteria, as it results in defective nanosheets unsuitable for membrane fabrication. Tsapatsis and coworkers developed a polymer-based exfoliation technique

for ITQ-1 and multilamellar silicalite-1 zeolites, which delivered high-quality MWW and MFI nanosheets, respectively.³⁵ After the purification steps to isolate the nanosheets from the polymeric matrix and the removal of larger unexfoliated particles by centrifugation, the 1 or 1.5 unit-cell-thick zeolite nanosheets were assembled into thin membranes by vacuum filtration. Although successful fabrication of well *b*-oriented MFI nanosheets membranes was achieved (*c*-oriented for MWW), which exposes the shape-sieving 0.55 nm pore of MFI to the gas phase, no separation for the xylene isomers was reported due to the presence of non-selective pathways between the nanosheets (Figure 1.4a).

After performing a mild secondary growth step to seal these defects, the prepared membranes showed a p-xylene/o-xylene separation factor (SF) in the range of 40-70 and p-xylene permeance of $3 \times 10^{-7} \text{ mol m}^{-2} \text{ s}^{-1} \text{ Pa}^{-1}$ at 150 °C. The final membrane thickness was only 200 nm, which is an order of magnitude lower than conventional polycrystalline zeolite membranes.

The employment of secondary growth is considered to be a problematic step because it is an expensive and complicated process that hinders the scale-up for commercial applications affecting membrane reproducibility.⁶⁰ To bypass the solvothermal recrystallization step, the same group developed a gel-less secondary growth to seal non-selective pathways. MFI nanosheets were deposited on a porous Stöber silica layer by vacuum filtration, and a gel-less secondary growth was performed, resulting in a membrane thickness of 100 nm. The Stöber spheres acted as a silica source during the regrowth step, and the same *b*-orientation was maintained, producing a higher p-xylene/o-xylene SF compared to the previous study while maintaining similar fluxes.⁶¹

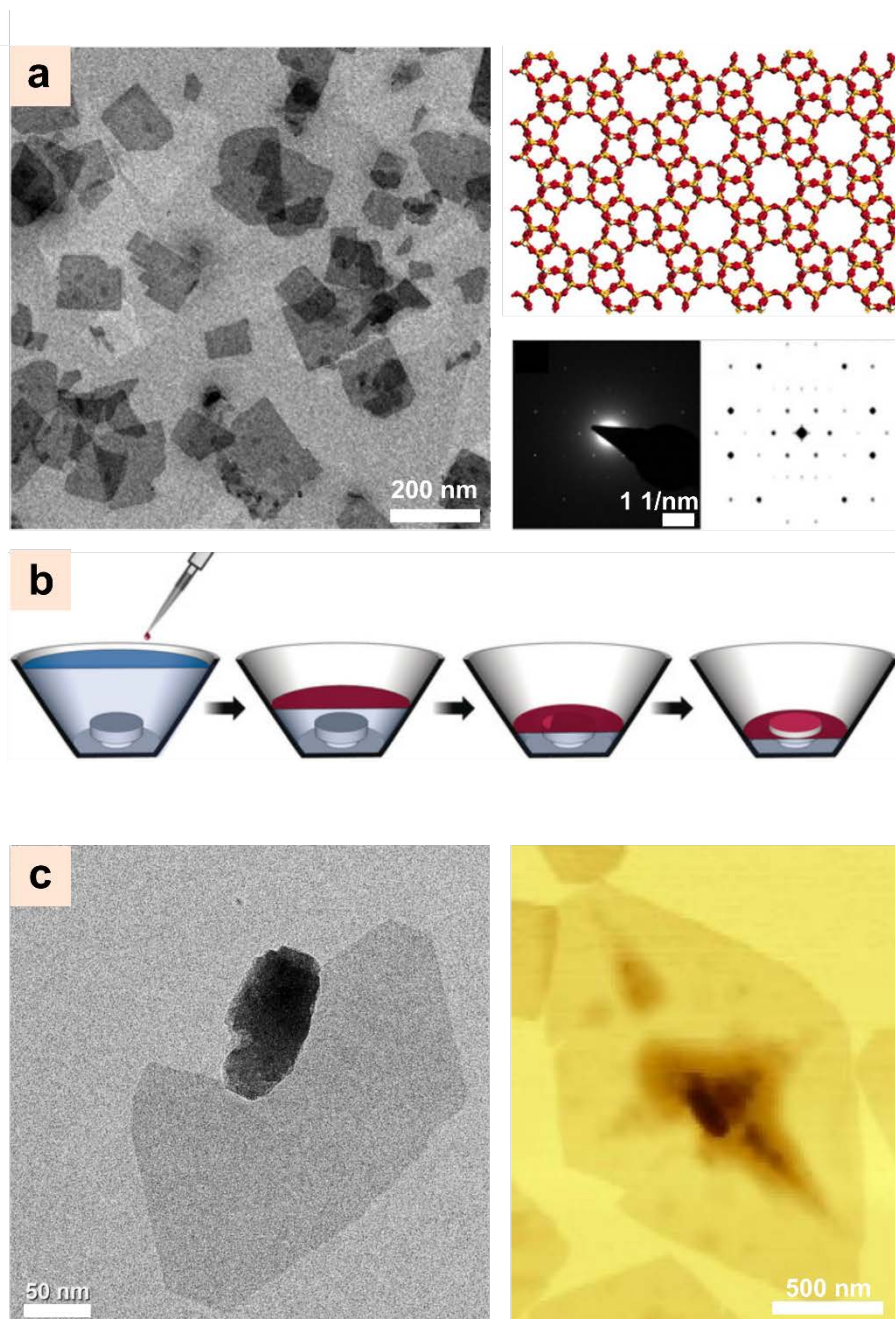


Figure 1.4. a) TEM image of a single MFI nanosheet and its crystal structure along the b axis. Electron diffraction pattern measured and simulated of MFI.³⁵ b) Illustration of MFI monolayer deposition in a conical reservoir. The liquid is slowly drained from the bottom to lower the level and compress the nanosheets.⁶² c) TEM and AFM images. Gradual and complete bottom-up growth of the MFI nanosheet around the seed.⁶³ Reprinted with permission. Ref. [35]: Copyright 2011, American Association for the Advancement of Science. Ref, [63]: Copyright 2017, John Wiley and Sons.

Another key step to further improve the membrane performance was the partial removal of the organic structure-directing agent (OSDA), which allowed the dispersion of the nanosheets in more environmentally friendly solvents such as water and ethanol, and offered the opportunity to stabilize the nanosheets at the air/water interface. The stabilization of monolayers of MFI nanosheets at the air/water interface of a conical reservoir, along with the slow withdrawal of water

from the bottom part, allowed the careful deposition of the nanosheets onto a porous Stöber silica layer, giving rise to very thin zeolite nanosheet-based films (Figure 1.4b). Subsequent exposure of the nanosheets layer to the gel-less secondary growth process delivered an unprecedented separation performance with a SF between xylene isomers over 10000 and a permeance of $2.9 \times 10^{-7} \text{ mol m}^{-2} \text{ s}^{-1} \text{ Pa}^{-1}$.^{51,62}

Bottom-up synthesis of MFI nanosheets can eliminate the structural defects that may arise from the top-down approach. Tsapatsis and coworkers achieved a breakthrough in synthesizing 5 nm-thick MFI nanosheets (2.5 unit cells) by appropriately suppressing the orthogonal growth with the use of bis-1,5(tripropyl ammonium)pentamethylene diiodide structure-directing agent (Figure 1.4c). Their pioneering work produced micrometer MFI nanosheets in lateral size, and their stacking onto a porous support with the previously developed gel-less secondary growth resulted in excellent performance for the xylene isomers separation.⁶⁴

Since the first synthesis of 2D membranes with MFI and MWW nanosheets, extensive work has been carried out by Tsapatsis and coworkers in developing very thin nanosheet layers without the need for solvothermal secondary growth. However, more research needs to be performed in this direction to completely eliminate the gel-less secondary growth. Moreover, increase in the exfoliation yields, synthesis of larger lateral nanosheet size, and the use of cheaper supports would facilitate the scale-up of these high-performance membranes.

1.6.2. Transport through nanoporous MOFs

Metal-organic frameworks (MOFs) are a new emerging class of materials consisting of metal ions or clusters coordinated with organic linkers, leading to a highly crystalline nano- or microporous network. Due to their high porosity, tunable pore size and structure, and abundant surface functional groups, they have attracted exponential interest in many applications, such as separation and gas storage, catalysis, chemical sensing, and drug delivery.⁶⁵ Beside their three-dimensional structure, many-layered MOFs have been reported in literature offering the potential of their implementation as building blocks for 2D-based membranes.⁶⁶ Nevertheless, challenges remain in the top-down exfoliation strategy to fully preserve the nanosheets' crystallinity and their high aspect ratio. On the contrary, the bottom-up approach could produce higher quality MOF nanosheets.

Despite the challenges in the top-down approach in preserving the morphological and structural integrity of the MOF nanosheets, Yang's group was successful in exfoliating 1-nm thick MOF

nanosheets with a lateral size larger than a micrometer while preserving their crystallinity.³⁶ A combination of a low-energy wet-ball milling and sonication exfoliated the MOF precursor $\text{Zn}_2\text{-(bim)}_4$ (bim=benzimidazole). Their key finding was to use a mixture of solvents, namely methanol and propanol. The former would access the interlayer spacing, thanks to its smaller kinetic diameter, while the latter was able to stabilize the exfoliated nanosheets. The exfoliated MOF nanosheets have a theoretical pore size of 0.21 nm, and the flexible framework could accommodate H_2 molecules into these pores. To avoid the restacking of the nanosheets, they adopted the hot-drop coating method onto a porous ceramic support, which increased the turbostratic disorder between the nanosheets (Figure 1.5a). Ultrathin membranes (thickness <10 nm) were fabricated, which gave a sharp molecular cut-off between H_2 and CO_2 with SF as high as 291 with a H_2 permeance higher than 2000 GPU (1 GPU = $3.3 \times 10^{-10} \text{ mol m}^{-2} \text{ s}^{-1} \text{ Pa}^{-1}$). It is worth mentioning that no absolute pressure difference across the membrane was applied to prevent bending/deformation of the nanosheets with loss in performance.

Ball milling and ultrasound exfoliation method might damage fragile MOFs. Wang et al. employed a mild freeze and thaw technique to exfoliate MAMS-1 (Mesh Adjustable Molecular Sieve, $\text{Ni}_8(5\text{-bbdc})6(\mu\text{-OH})_4$, 5-bbdc stands for 5-tert-butyl-1,3-benzenedicarboxylate) into nanosheets.⁴⁰ The fast volumetric expansion of the solvents during the thawing process created shear stress between the layers overcoming the weak Van der Waals interactions (Figure 1.5b). MAMS-1 possesses two different pore domains: 0.29 nm pore aperture parallel to the nanosheet plane and 0.55 nm aperture perpendicular to the smaller pore. It is then of vital importance to ensure the right in-plane orientation of the nanosheet to expose the more selective pore. This could be achieved using the hot-drop casting method at a temperature slightly higher than the solvent boiling point to allow fast evaporation and avoid the restacking of nanosheets as well as the desired nanosheets orientation.

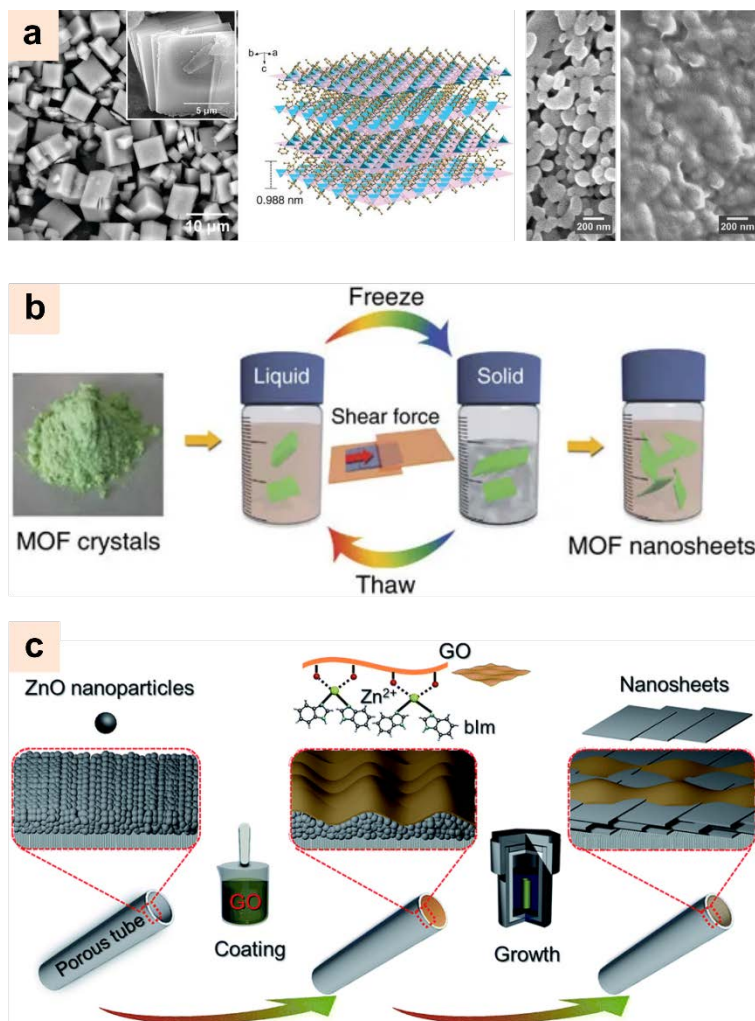


Figure 1.5. a) SEM image of as-synthesized $\text{Zn}_2(\text{bim})_4$ with its theoretical layered structure and the SEM images of bare porous support as well as with coated nanosheets.³⁶ b) Image of MAMS-1 crystal with an illustration of the freeze-thaw exfoliation method.⁴⁰ c) Illustration of the steps for preparing oriented $\text{Zn}_2(\text{bim})_4$ nanosheets membrane by zinc oxide self-conversion growth in GO confined space.⁶⁷ Reprinted with permission. Ref. [14]: Copyright 2014, American Association for the Advancement of Science. Ref. [40]: Open access, Copyright 2017 Springer Nature. Ref. [67]: Open access, The Royal Society of Chemistry (RSC).

Membranes with thicknesses up to 40 nm were fabricated. The 12-nm membranes displayed a H_2/CO_2 SF of 34 and H_2 permeance of 6516 GPU, while the 40 nm-thick membranes could achieve a higher separation factor of 235 at the expense of an order of magnitude lower H_2 permeance. Interestingly, their membranes showed a reversed thermo-switchable behavior. The gas pair selectivity was ranging from 5 at 100 °C to 245 at room temperature. In situ X-ray measurements helped explain this abnormal behavior with the flexibility of the tert-butyl groups as a function of temperature. This stimuli-responsive feature finding can be potentially exploited in temperature-swing-related gas separations.

Membranes supported on small-diameter tubular supports are of great importance in gas separation applications because they offer high surface area per unit of volume and can withstand higher

pressures. However, the top-down approach is confronted with many engineering challenges in fabricating 2D nanosheets onto tubular supports. Similarly, it is not trivial to directly grow 2D MOF membranes on tubular substrates. Li et al. were the first to report the synthesis of a crystalline nanosheet membrane on a porous tubular substrate by direct growth.⁶⁷ They exploited the GO-guided growth by first depositing a thin layer of ZnO nanoparticles on the tubular support by dip-coating, followed by another layer of GO upon which the nanoparticles self-converted into $\text{Zn}_2(\text{bIm})_4$ nanosheets membranes. The 200 nm thin membranes displayed a H_2/CO_2 selectivity of 106 and a H_2 permeance of ca. 500 GPU (Figure 1.5c). Their strategy offers the opportunity for the large-scale fabrication of highly-oriented MOF nanosheet membranes on a tubular geometry, which is relevant for industrial gas separations.

Unprecedented performance has been achieved with 2D MOF nanosheets-based membranes. Nevertheless, many efforts still need to be made before achieving the precise manipulation of the nanosheets, especially on a large scale. Fabrication of nanosheet lateral sizes larger than 1 μm , uniform nanosheet thickness, higher degree of crystallinity (particularly for the top-down exfoliation approach), and scalable membrane fabrication strategies are all vital features that still represent a hurdle in the commercialization of MOFs membranes. Moreover, investigations of their mechanical and chemical stability in real commercial operating conditions need to be performed.

1.6.3. Transport through graphene oxide nanochannels

GO is a derivative of graphene, and it is widely obtained from the oxidation of graphite using Hummer's method.⁶⁸ The oxidation method developed by Hummer produces GO with a high content of oxygen-rich functional groups (hydroxyl, carboxyl, and epoxy groups) on the basal plane as well as on the nanosheet's perimeter. The transport of molecules occurs mainly through the gallery spacings and through in-plane defects/gaps generated during exfoliation and/or during membrane assembly. The fine-tuning of the interlayer spacings between the nanosheets plays a key role in gas and water separations. Li et al. assembled GO nanosheets into a 1.8 nm-thick membrane by simple vacuum filtration, achieving unprecedented H_2/CO_2 and H_2/N_2 selectivities of 3400 and 900, respectively (Figure 1.6a). However, the H_2 flux was low for such a thin membrane, demonstrating the 'zig-zag' type of transport.³⁰ The importance of rationally manipulating the repulsive/attractive forces between the functional groups in the nanosheets can drastically change the GO membrane performance. Xu and coworkers rationally designed external forces (i.e., vacuum-filtration-coupled shearing forces derived from the spin-coating system) as well as inner forces (i.e., using intercalating polymers) to finely manipulate the 2D channels aperture.⁶⁹ The

polymer intercalation suppressed the repulsive force, while the external forces contributed to the well-ordered packing of nanosheets. The as-prepared membranes, with 2D channels of 0.4 nm, displayed 2–3 orders of magnitude improvement in hydrogen permeance and a 3-fold enhancement in the H_2/CO_2 selectivity (Figure 1.6b).

The interaction of the guest molecules with the functional groups present in the nanosheets can facilitate the transport of molecules. For example, μm -thick GO membranes were impermeable to even the smallest gases and changed their behavior after being exposed to water.⁷⁰ A fast transport took place due to a combination of the favorable interactions between water molecules and functional groups of GO and the fact that water can flow frictionless in the hydrophobic domains of GO.⁵³ On a similar principle, Zhou et al. functionalized GO nanosheets with a brush-like CO_2 -philic agent (piperazine) using vacuum filtration on a tubular support. The 20 nm-thick membranes exhibited a remarkable CO_2 permeance of 1020 GPU and a CO_2/N_2 selectivity of 680, while the non-grafted nanosheets showed orders of magnitude lower performance (Figure 1.6c).⁵⁴

Considerable progress has been achieved in the fabrication methods of GO membranes, as well as improvements in their performance. However, the long-term stability of the well-designed nanochannels, especially in the presence of water, along with the development of low defective nanosheets during exfoliation, needs to be fully investigated. Moreover, the inefficient ‘zig-zag’ type of transport motivates the formation of few-nanometer thick membranes to increase productivity, which might be technically challenging to engineer on an industrial scale.

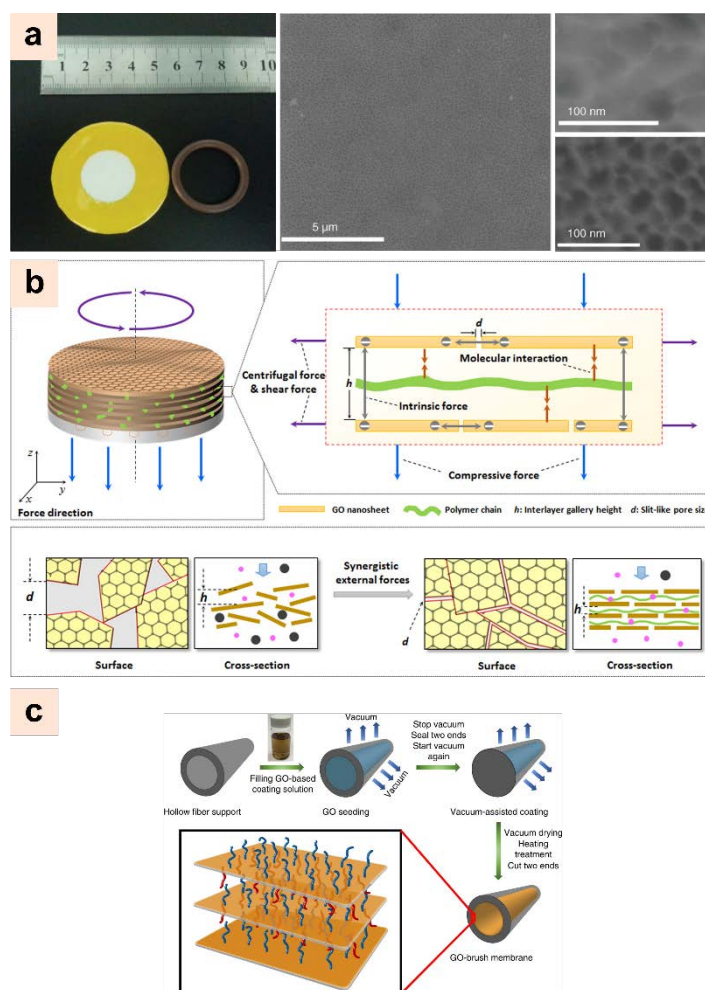


Figure 1.6. a) Picture of GO membrane on porous AAO support. Yellow and brown circles are Kapton tape and O-ring for sealing the membrane. Middle, SEM image of 18 nm-thick GO membrane on AAO support. Right, SEM images of AAO support with (top) and without (bottom) GO nanosheets.³⁰ (b) Illustration on the design of GO nanochannels with external forces application. Enlarged view shows resultant force (i.e., compressive, centrifugal, and between the polymer and GO sheets). Below, hypothetical assembly of GO sheets in the surface and cross-section with (right) and without (left) the application of the rationally designed forces.⁶⁹ (c) Illustration of the fabrication process of CO₂-based hollow fiber membranes with a brush-like CO₂-philic agent. Red and blue brushes are a visual aid to distinguish between molecules grafted on the bottom and top of the GO surface, respectively.⁵⁴ Reprinted with permission. Ref. [30]: Copyright 2013, the American Association for the Advancement of Science. Ref. [69]: Copyright 2016, American Chemical Society. Ref. [54]: Open access, Copyright 2017 Springer Nature publisher.

1.7. Opportunities for zeolite membranes compared to polymeric membranes

The successful implementation of polymeric membranes into commercial applications for gas separation has been widely demonstrated (Table 1.1). The key aspect of these commercial applications where polymeric membranes are employed is the mild temperature-operating condition limited to values below 150 °C.⁷¹ For applications where the operating conditions are

harsher, the use of most polymeric materials is precluded. High-temperature polymers (polybenzimidazole-based polymers) have shown excellent selectivities, for instance, for H_2/CO_2 separation and can withstand high temperatures; however, their low permeabilities represent a major bottleneck for the scale-up of these membranes.^{72–74}

A window of opportunity where zeolite-based membranes can stand out compared to polymeric ones is for high-temperature applications. Although it is always possible to cool down a gas stream and perform the separation with polymers, this is highly undesired due to the increased capital and operating costs and energy losses. Therefore, we identified major applications that are widely employed in the industry, where zeolite membranes could find an opportunity compared to polymeric membranes.

- *Hydrogen purification.* Hydrogen-based fuels are proposed as a transition energy source to renewable energies.⁷⁵ The current global hydrogen production is approximately 7.2 exajoules (EJ) per year, and its production is essentially fossil fuel-based. The amount of CO_2 emitted per year due to the production of hydrogen is approximately 500 Mt. Hydrogen production from fossil fuels with carbon capture and storage (CCS) may prove to be an effective process for reducing the CO_2 emissions.⁷⁶

Hydrogen production primarily relies on the transformation of hydrocarbons into syngas (mixture of H_2 and CO). The latter is typically produced by different routes such as gasification, steam methane reforming (SMR, 500–900 °C and 10–60 bar), autothermal reforming (ATR), etc. The syngas undergoes the water-gas shift reaction (WGS, 200–400 °C and 10–40 bar) to further convert carbon monoxide into hydrogen and carbon dioxide. The final reaction mixture mainly comprises CO_2 , H_2 , and unconverted reactants, and therefore requires a process for energy-efficient H_2 purification and CO_2 capture at temperatures higher than 200 °C. Thermally stable, energy-efficient membranes are highly attractive in this regard.

- *Pre-combustion capture.* During pre-combustion capture in an integrated gasification combined cycle (IGCC) power plant, coal is gasified to produce syngas. The syngas, similarly to the SMR, is shifted to CO_2 and H_2 . At this stage, in conventional IGCC plants, the shifted stream is cooled down, and amine-based absorption separation is implemented to absorb the CO_2 yielding a clean H_2 stream that is combusted in a gas turbine.⁷⁷ The implementation of membranes capable of withstanding high temperatures ($T > 200$ °C) and

H₂/CO₂ selectivity higher than 20 could remarkably increase the overall process efficiency.⁷⁸

- *Membrane reactor.* Catalytic chemical reactors are often operated at high temperatures. The availability of inorganic membranes capable of withstanding the reaction environment enables the coupling of reaction and separation steps in a single equipment. This can be achieved by either controlling the feed of a specific reactant or by selectively removing one of the reaction products, thus increasing the conversion of thermodynamically limited reactions (e.g., water-gas shift reaction, SMR).¹⁸

1.8. Zeolites: Limitations and opportunities

15% (130 out of 840) of the whole industrial catalysts are represented by zeolites.⁷⁹ Decades of study on zeolites have achieved astonishing industrial results, making them the state-of-the-art catalytic materials for many basic refinery processes (e.g., fluid catalytic cracking, hydrocracking, etc.).⁸⁰ On the other hand, the commercialization of zeolite membranes has been limited to only dehydration of organic solvents based on hydrophilic LTA-zeolite frameworks.^{81,82}

Many obstacles limited the commercialization of zeolite membranes, such as the membrane synthesis method, the prohibitive costs and large-scale engineering of the inorganic supports, and the use of expensive organic structure-directing agents.^{27,83}

High-performance zeolite membranes for gas separation are generally synthesized using seeded secondary growth over the *in-situ* crystallization method. The latter consists of placing the synthesis mixture (silica and alumina sources, SDA, and water) together with a porous substrate into an autoclave at high temperature, where the zeolite crystals nucleate and grow directly on the inorganic support.⁸⁴ The limited control over the anisotropic crystals orientation and the coupled nucleation-growth restricts the *in-situ* method compared to seeded secondary growth. The latter consists of synthesizing nano-seeds of the aimed zeolite in the range of 50-1000 nm and in depositing them onto a porous support. After a secondary re-crystallization step, the seeds are intergrown, forming a continuous and thin film.²⁷ Seeded secondary growth is a more versatile approach that decouples nucleation and growth of the crystals. It provides a higher degree of freedom by allowing the orientation of the anisotropic seeds, which plays a major role in the quality of the final membrane.⁸⁵ At the same time, hydrothermal synthesis and the subsequent activation of secondary-growth zeolite films results in reproducibility issues due to grain boundary defects, cracks, etc., hindering the vital requirement needed for industrial commercialization.^{83,86}

As mentioned in section 1.5 (chapter 1), a possible strategy to avoid secondary growth is the synthesis of 2D zeolite building blocks that can be assembled into thin films.⁸⁷ In the last decade, Tsapatsis and coworkers successfully initiated and advanced this strategy by synthesizing 2D MFI-based ultrathin membranes for the separation of xylene isomers.^{35,51,55,64,88–91} However, high-performance membranes that are based on the sole assembly of MFI nanosheets on a porous support or 2D zeolitic membranes capable of sieving light gases (H_2 , CO_2 , N_2 , O_2 , and CH_4) were not reported. When multilamellar-MFI nanosheets were assembled without secondary growth, a selectivity between butane isomers of 5.4 was obtained, which was an order magnitude lower than that achieved with secondary-regrown nanosheets demonstrating the existence of non-selective pathways.⁸⁹

The synthesis of high-performance zeolitic membranes without resorting to the secondary growth process remains a grand challenge. The other limiting factors (support and SDA) will be discussed in detail in the following sections.

1.9. Zeolites for H_2/CO_2 separation

The window of opportunities for zeolite membranes identified in section 1.7, foresees many applications based on the ability of zeolite membranes to sieve H_2 from CO_2 at high temperatures. However, current zeolite membranes are unable to efficiently sieve this gas mixture because of poor selectivities.⁹² The transport across a zeolite membrane starts with the adsorption of the gas molecules from the gas onto the zeolite framework, followed by the diffusion through the framework under surface diffusion (at low temperatures) or activated diffusion (at elevated temperatures), and the final desorption on the permeate side into the gas phase.^{93,94} H_2/CO_2 is a very challenging separation because of the diverse nature of these two molecules. CO_2 has a larger quadrupole moment compared to H_2 , which increases its adsorption in zeolites.²⁷ On the other hand, the smaller H_2 kinetic diameter allows for higher diffusion rates compared to CO_2 . These two extremes in their properties make the choice of zeolitic framework and of operating conditions arduous.

While there is a lack of pure zeolite membranes capable of separating H_2 from CO_2 , membranes that exploit the higher CO_2 condensability by permeating CO_2 and rejecting H_2 have been extensively reported. Hedlund and coworkers successfully prepared ultrathin (0.5–1 μm) MFI-zeolite membranes with extremely high flux and capable of achieving CO_2/H_2 selectivities up to

258 at 235 K and 9 bar.⁹⁵ At the same temperature, Noble and coworkers demonstrated the potential of SAPO-34 zeolite in the CO₂/H₂ separation reporting a separation factor of 110 with a moderate flux.⁹⁶

The use of CO₂-selective membranes requires operating at low temperatures to prevent losses in the membrane performances. CO₂ uptake in the zeolite framework is an inverse function of temperature, which results in a steep decrease in the CO₂/H₂ selectivity up to two orders of magnitude when going from 253 to 473 K.⁹⁶

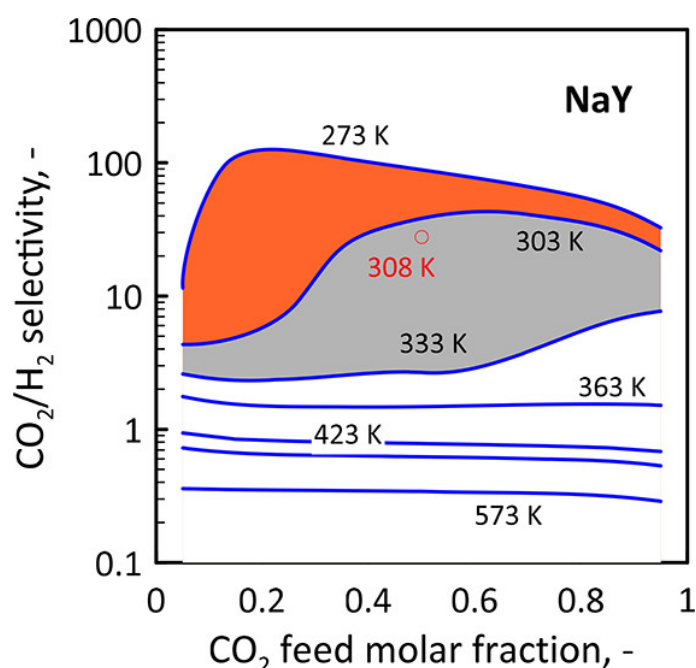


Figure 1.7. CO₂/H₂ selectivity as functions of CO₂ molar fraction at different temperatures in a NaY membrane. Feed pressure = 100 kPa, permeate pressure = 1 kPa. “O” experimental value of 4. Reprinted with permission from [97].

Barbieri and coworkers, based on surface and Knudsen diffusions, predicted the CO₂/H₂ transport mechanism of three different zeolite frameworks (i.e., FAU, DDR, and MFI) and further confirmed the very strong temperature dependence of CO₂/H₂ selectivity (Figure 1.7).⁹⁸

Overall, remarkable achievements have been attained using zeolite membranes for CO₂/H₂ separation, and while CO₂-selective membranes may offer the benefit of high-pressure H₂ streams in the retentate, ready to be used for further applications with less recompression energy, the implementation of low-temperature separations and the need of gas stream cooling and reheating is a major energetic disadvantage.

To develop H₂-selective membranes, the thermodynamic parameter (i.e., adsorption) must be minimized in favor of the kinetic parameter (i.e., diffusion) to favor the smaller kinetic diameter of

H₂ compared to the higher adsorption degree of CO₂. This can be achieved by utilizing zeolite frameworks with small pore sizes and high-temperature operating conditions. Zeolites possessing 6-MRs (six-membered rings of connected SiO₄ tetrahedra) are good candidates for the transport of small molecules such as He, H₂O, and H₂.^{92,99,100}

Sodalite zeolite has a high concentration of 6-MRs and could potentially offer efficient H₂/CO₂ separation. Sodalite membranes have been used for water desalination,¹⁰¹ alcohol dehydration,^{102–105}, and H₂/*i*-butane separation¹⁰⁶, yet their investigation for H₂/CO₂ separation still needs to be reported. Occluded structure-directing agent (SDA) and reproducibility issues from secondary growth synthesis are the main reasons for the low-performing sodalite membranes for gas separation together with structure collapsing when attempting to free the sodalite cages by removing the SDA.^{107,108}

A hydrous layered silicate (HLS) composed of chains of 4-MRs of SiO₄ tetrahedra that connect to form 6-MRs windows, called RUB-15, was reported in 1996 by Gies and coworkers.¹⁰⁹ RUB-15 possesses the desired SOD topology while retaining a layered structure. Okubo and coworkers demonstrated the first instance of transformation by topotactic conversion of RUB-15 layers into sodalite framework.¹¹⁰ Their key-finding consisted in identifying an appropriate intercalating molecule (e.g., acetic acid) that could replace the tetramethylammonium (TMA) SDA and in shifting the layers to the perfect *in-plane* registry to condense the interlayer Q³ sites ((SiO)₃SiOH or (SiO)₃SiO⁻). Later Koike et al. investigated the degree of crystallinity of the topotactically converted sodalite structure from RUB-15 using different acid treatment conditions.¹¹¹

The layered nature of RUB-15 could be a great opportunity to exploit the potential of the 6-MRs of the SOD topology while facilitating the removal of the SDA without collapsing the hemihedral cages. Moreover, its exfoliation could provide thin nanosheets for the synthesis of zeolitic membranes using the building block approach mentioned in section 1.5.

1.10. Importance of the support for commercialization of zeolitic membranes

Flux and membrane thickness are inversely proportional (Eq. 10). Zeolites membranes with only a few hundreds of nanometers have been synthesized to minimize the diffusional path that molecules need to travel.^{88,92}

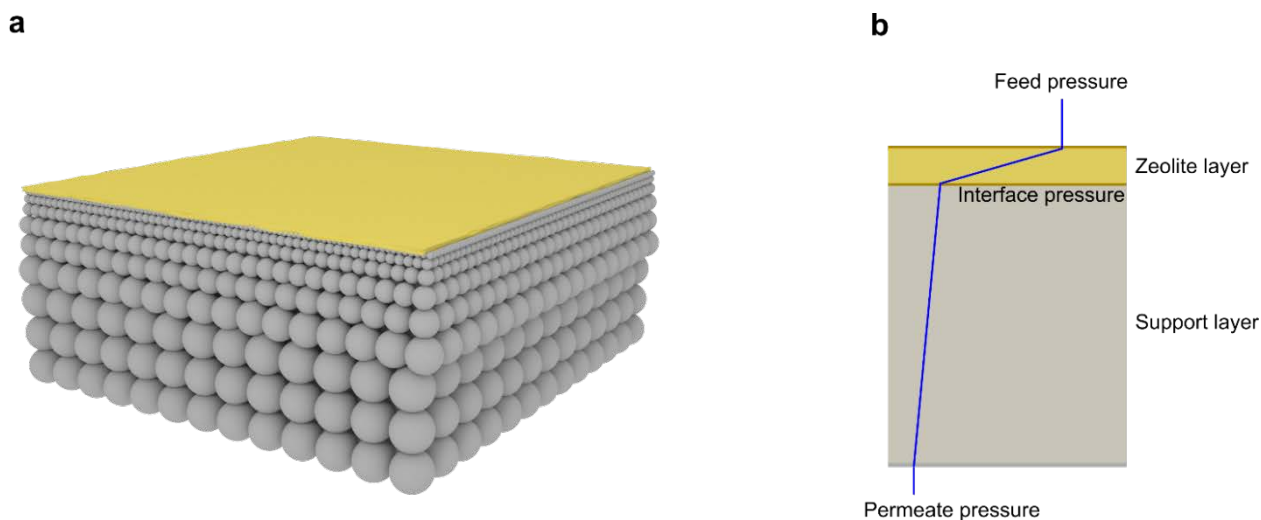


Figure 1.8. a) Planar asymmetric ceramic support with the zeolite layer. b) Pressure-drop diagram along the composite layers.

Ultrathin zeolitic membranes are not self-standing and need to be supported. The underlying support plays a crucial role for successful membrane preparation. Smooth surface, low-transport resistance, chemical and thermal stability are the primary requirements needed to support a zeolite layer. The employed porous supports are generally inorganic (e.g., α -alumina, stainless steel, titania, etc.). The choice of the support is mainly dictated by the zeolite phase and support material compatibility. Zeolites tend to have a negative thermal expansion coefficient (their lattice shrinks upon heating); unlike for most ceramic materials, this is positive.¹¹² The mismatch in the thermal expansion coefficient between zeolites and supporting layer is a major cause for the formation of defects, pinholes, cracks, etc., during the zeolite activation (i.e., SDA removal) and high-temperature testing.

The performance of the zeolite layer is highly affected by the support transport resistance. An ideal support should have a lower transport resistance, which is usually achieved by fabricating graded supports where the coarse layers facilitate the gas transport, while the fine texture of the top layer serves as a smooth surface for the zeolite seeds deposition (Figure 1.8a). For an optimal support, the major pressure drop should be located in the zeolite layer, while from the interface zeolite-support to the permeate side, the pressure drop should be negligible (Figure 1.8b).

Typically, the cost of the inorganic support used for zeolite membranes accounts for 70% to 90% of the overall membrane cost.^{27,83,113} Considering the uneven cost distribution caused by the support, the replacement with alternative, cheap materials would grant zeolite membranes a step forward towards commercialization in gas separation. Polymeric supports offer a great opportunity

to cost reduction for zeolite membranes; however, most of the zeolite frameworks require an activation step at high temperatures (> 673 K) in an oxidative atmosphere to remove the SDA, which would forbid the use of the majority of polymers.¹¹⁴ High-temperature polymers such as polybenzimidazole (PBI) are thermally and mechanically stable and display a high glass transition temperature (> 400 °C).¹¹⁵ The dense phase of PBI has an extremely low flux, which enables the use of PBI as support only in the porous form obtained *via the* non-solvent induced phase separation (NIPS) process. However, the calcination temperatures of zeolites exceed their thermal stability rendering their potential use only possible with alternative and milder detemplation processes.

Zeolite detemplation

Alternative and milder detemplation processes for the SDA removal are imperative for the employment of polymeric supports. SDA removal reaction is a function of both temperature and time. The simplest alternative method to conventional heat treatment at high temperatures is to lower the temperature at the expense of longer combustion time. Zhang et al. successfully detemplated MFI nanosheet membranes by using a temperature as low as 280 °C for 8 h yielding high-performance membranes for xylene and butane isomers separation.⁹¹

UV/ozone treatment is another alternative way to remove the SDAs from the zeolite framework that has been successfully employed.^{116,117} Zeolites are generally calcined with very small heating and cooling ramps to minimize crack formation; however, rapid thermal treatments (RTP) with a fast heating/cooling to 600-900 °C yielded remarkable results by healing grain boundary defects in polycrystalline silicalite-1.¹¹⁸ Finally, extraction-based detemplation in acidic media is a method that was initially conceived for mesoporous materials and adapted to microporous silicates by Lami et al. who employed nitric acidic solutions to extract the SDA from the beta zeolite.¹¹⁹

Great efforts have been devoted to the development of new detemplation methods, and these could enlarge the spectrum of polymeric materials that can be adopted as supports for zeolitic membranes. However, only a few of these methods are compatible with carbon-based polymers since the high temperatures of RTP and UV/ozone methods could degrade the polymeric chains. Achieving the implementation of lower detemplation temperatures to enable the use of high-temperature stable polymeric supports (e.g., polybenzimidazole) is just the first step. Many challenges still need to be overcome for the porous PBI polymer before being employed at a large scale, such as the fragile nature upon drying, the instability of the dope solutions used for NIPS process, and high degrees of shrinkage.

The successful synthesis of zeolite membranes onto polymeric supports has been demonstrated for frameworks that do not require SDA for their synthesis or if an activation step is not required, and such membranes yielded excellent performance.^{120,121} This is a great motivation in driving and directing more efforts towards new scalable and thermally resistant polymeric supports for zeolite membranes with the aim to benefit both their scalability and cost reduction.

1.11. Process simulation

The performance and the conceptual design of a membrane must be strictly developed as a function of the process operating conditions and the downstream applications of the purified stream. The circumscribed concept of developing a membrane with ultrahigh selectivity and permeance can be misleading.

For instance, with a fixed recovery (i.e., the ratio between flow of component of interest in permeate and feed streams) and purity of the component of interest in the permeate stream, the optimal membrane selectivity of the membrane is not always the highest: membranes with extremely high selectivity would require much larger areas to allow the less permeable component to reach the permeate side and balance the mixture to the targeted purity and recovery. Similarly, membranes with poor selectivity would also require large areas to allow enough of the component of interest to permeate, reaching the desired targets. Hence, the optimal selectivity that would minimize the membrane area is a function with an optimal minimum, which would require careful process simulation analysis to be determined.¹²²

Another instructive example on how high permeance and selectivity can turn to be a drawback is the concentration polarization phenomenon. The driving force for a component to permeate through the membrane is a function of the concentration difference (or, more in general, the chemical potential) at the very interface gas-membrane between upstream and downstream sides. When a highly selective and permeable membrane is employed, the concentration polarization takes place due to the fact that the permeation of the permeable component through the membrane is faster than the transport from the bulk to the membrane, thus, in a steady-state condition where the two fluxes have to be equal, the concentration at the interface is lower than that in bulk. This drastically reduces the driving force for the separation resulting in higher energy/membrane costs.¹²³

The above examples show that focusing on a few membrane parameters only can be counterproductive. The membrane synthesis and development cannot neglect the process

simulation, which provides the techno-economic analysis to minimize the overall cost for a given separation. The techno-economic analysis uses membrane performance parameters together with process variables to determine the optimal membrane configuration that minimizes the overall membrane and energy cost (Figure 1.9).

The development of a different type of membranes with higher flux and moderate selectivity and vice versa could provide a higher degree of freedom to process simulation analyses to find optimal configurations and operating parameters expanding the domain of the minimization of objective function costs.

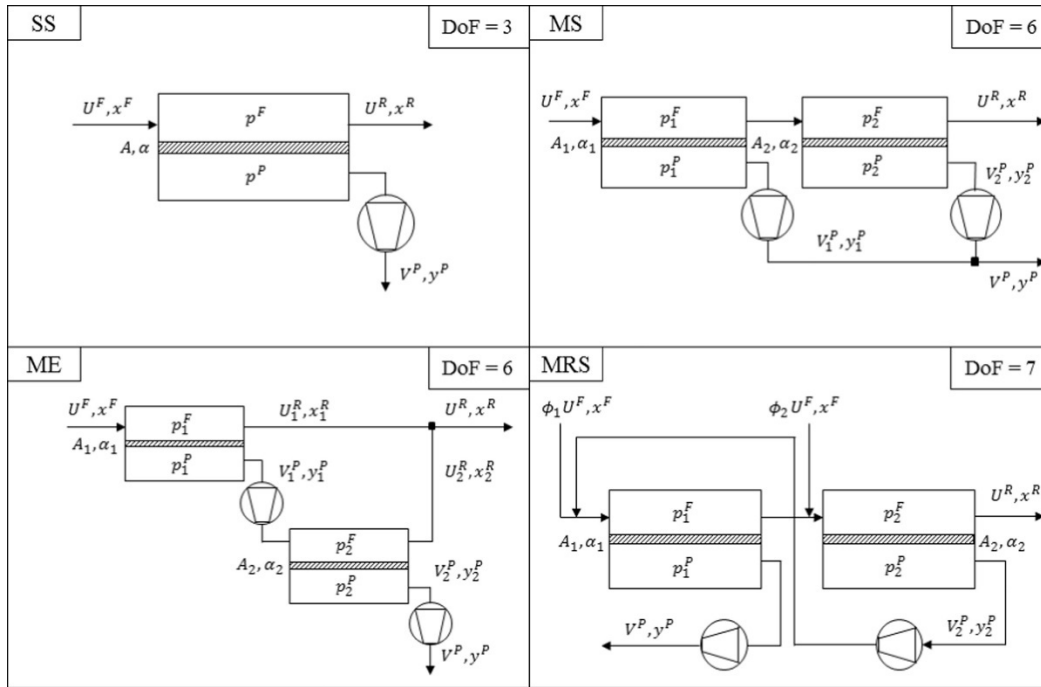


Figure 1.9. Two-stage layouts (for illustrating purposes) for the implemented configurations: (i) single module (SS), (ii) multistage stripper (MS), (iii) multistage enricher (ME), (iv) multistage with recirculation and feed splitting (MRS). Reprinted with permission [124]

1.12. Thesis outline

This dissertation aims to address longstanding challenges in the zeolitic membrane fabrication by looking at all the major components of the “membrane separation process” (i.e., selective layer, support, and process simulation), providing a comprehensive tool from selective-layer synthesis to potential application. For the selective layer, we report the synthesis of ultrathin zeolitic membranes without resorting to the secondary growth process using crystalline 0.8 nm-thick nanosheets as building blocks. Concerning the support, we report the development of a low-cost, scalable, and high-temperature polymeric support that could lower the overall zeolite membrane cost with the

potential of serving as support across different materials-based membranes. Finally, a carbon-based membrane possessing the second-highest flux ever reported in the literature with a Knudsen H_2/CO_2 selectivity was developed, and a techno-economic analysis was performed to evaluate the impact on the overall cost for pre-combustion capture using different stage configurations. The effect of combining membranes with different permeance/selectivity on the pre-combustion capture was evaluated by combining the two developed membranes (i.e., zeolitic and NPC).

Chapter 1. The challenge of separations is dealt with on a fundamental thermodynamic level. High-performance membrane-based separations are introduced as a potential means to approach the minimum theoretical work of separation. Current industrial applications for gas separation are discussed, and the limitations that hinder inorganic membranes for gas separation are highlighted. Current two-dimensional membranes are reviewed with special emphasis on zeolites and their transition from polycrystalline to 2D membranes. Potential applications for zeolite membranes are identified together with specific zeolitic frameworks capable of sieving H_2 from CO_2 . Finally, guidelines on the ideal support for zeolite membranes to reduce the overall membrane cost are provided, and the need to use process simulation analyses as feedback on the membrane synthesis is emphasized.

Chapter 2. The synthesis of 300 nm-thick zeolitic membranes using 0.8 nm-thick RUB-15 nanosheets as building blocks is reported without resorting to the secondary growth recrystallization process. Nudged elastic band (NEB) calculation guided our experimental work by computing the separation energies provided by the 6-MRs, which were promising for the H_2/CO_2 separation. Actually synthesized membranes confirmed the simulation studies as they gave H_2/CO_2 selectivities up to 100 in the temperature range of 25-300 °C, which make these pure zeolitic membranes the first able to carry out efficient pre-combustion capture. Moreover, this work contributed to expanding the limited library of exfoliated zeolitic nanosheets since this was the first report on the exfoliation of RUB-15.

Chapter 3. We report the synthesis of a new polymeric support made of PBI-AM FUMION® on a cheap stainless steel mesh. The high-temperature polymer (up to 330 °C) was prepared *via* the NIPS process and served as a support for RUB-15 nanosheets. A new milder detemplation process was developed to allow the employment of the PBI-AM support. 330 °C for 8 h was sufficient to remove the occluded organic molecules instead of 500 °C for 1 h. *In-situ* XRD during calcination confirmed the successful detemplation and the interlayer silanol condensation. A second

detemplation method was developed, which drastically cut down the membrane's processing time and steps. The use of diluted acetic acid solutions directly on filtered membranes successfully removed the occluded organic molecules as confirmed by XRD.

Chapter 4. A nanoporous carbon film (NPC) was fabricated by the pyrolysis of phase-separated block-copolymer/turanose film. The NPC was 100 nm thick and displayed a permeance of more than 2 million GPU with a H₂/CO₂ Knudsen selectivity in the temperature range of 25-300 °C. NPC membranes have been successfully used as a gas-permeable mechanical reinforcement for the crack-free synthesis of single-layer graphene membranes. Moreover, a techno-economic analysis of NPC membranes in pre-combustion capture with a two-stage process yielded extremely low specific membrane areas for H₂ purification, which can significantly cut down the footprint of the separation process and the associated capital cost. Finally, process simulation was employed to evaluate the impact of membranes with different performances (i.e., high selectivity and moderate permeance and vice versa) by employing RUB-15 and NPC membranes.

Chapter 5. A summary of the major achievements in synthesizing secondary-growth-free RUB-15 membranes is reported together with a future perspective on how to further improve the fabrication of RUB-15 membranes and on alternative employment of RUB-15 nanosheets in broader fields.

Chapter 2. Gas-sieving zeolitic membranes fabricated by condensation of precursor nanosheets

Adapted with permission from Mostapha Dakhchoune, Luis Francisco Villalobos, Rocio Semino, Lingmei Liu, Mojtaba Rezaei, Pascal Schouwink, Claudia Esther Avalos, Paul Baade, Vanessa Wood, Yu Han, Michele Ceriotti, and Kumar Varoon Agrawal, Gas sieving zeolitic membranes by the condensation of precursor nanosheets, Nature Materials, 20, 362–369 (2021). <https://doi.org/10.1038/s41563-020-00822-2>. Copyright © 2020, Springer Nature*

Abstract

The synthesis of molecular-sieving zeolitic membranes by the assembly of building blocks, avoiding the hydrothermal treatment, is highly desired for improving reproducibility and scalability. Herein, we report exfoliation of the sodalite precursor RUB-15 into crystalline 0.8-nm-thick nanosheets, hosting hydrogen-sieving six-membered rings (6-MR) of SiO₄ tetrahedra. Thin films, fabricated by filtration of a suspension of exfoliated nanosheets, possess two transport pathways, 6-MR apertures and intersheet gaps. The latter were found to dominate the gas transport, yielding a molecular cutoff of 3.6 Å with H₂/N₂ selectivity over 20. The gaps were successfully removed by the condensation of the terminal silanol groups of RUB-15, yielding H₂/CO₂ selectivities over 100. The high selectivity was exclusively from the transport across 6-MR, which was confirmed by the good agreement between the experimentally-determined apparent activation energy of H₂ and that computed by *ab initio* calculations. The scalable fabrication and the attractive sieving performance at 250–300 °C make these membranes promising for pre-combustion carbon capture.

1. Introduction

Zeolite membranes are attractive for energy-efficient molecular sieving under harsh chemical and thermal conditions.^{125–129} Although studied over close to 30 years,^{86,130} the adoption of zeolite membranes for gas and vapor separation has been hampered by the reproducibility issues in hydrothermal synthesis and the subsequent activation of the secondary-grown zeolite films on a porous support.⁸³ In this respect, the synthesis of high-performance zeolitic films by the assembly

of crystalline building blocks,^{35,89,131} avoiding the secondary growth step, is extremely desirable. One strategy to achieve this is synthesizing and applying crystalline, high-aspect-ratio zeolite nanosheets^{51,132–136} as a building block¹³⁷ for the zeolite film. Nanometer-thick nanosheets can enable ultrathin zeolite membranes⁶¹ comparable to the thickness of the skin layer of the polymeric membranes.⁷ The availability of such nanosheets is expected to benefit other applications of growing importance, including catalysis,^{138–140} and ion-exchange membranes in fuel cells and batteries.^{141,142}

The synthesis of zeolite nanosheets can be achieved by the top-down^{35,132} as well as the bottom-up¹⁴³ approaches. Advances in the bottom-up approach or direct synthesis of unit-cell-thick nanosheets by the hydrothermal synthesis have resulted in unilamellar MFI¹⁴³ and self-pillared pentasils (SPP)¹⁴⁰. On the other hand, the top-down approach, which involves the synthesis of lamellar zeolite precursor followed by exfoliation, has been highly successful in yielding nanosheets hosting molecular-sieving pores from a number of zeolite frameworks, including MWW,^{35,132} MFI,^{35,144} NSI,¹³⁴ FER,¹⁴⁵, etc. These approaches have also been extended to non-zeolitic layers yielding attractive performance, e.g., metal-organic frameworks nanosheets,³⁶ MXene,^{31,146}, etc. Yet, the fabrication of high-performance membranes by a facile assembly of zeolitic nanosheets has remained elusive.

For the synthesis of high-performance membranes by the assembly of microporous nanosheets, the following criteria must be satisfied, (i) synthesis of high-aspect-ratio nanosheets, (ii) preservation of microporous structure and sheet morphology during exfoliation, (iii) fabrication of compact nanosheet film on a porous support while eliminating large pinhole defects and sub-nanometer intersheet gaps. The last criterion is especially challenging because the intersheet gaps are intrinsic to the stacked nanosheet films and tend to dominate the overall molecular transport and, therefore, the molecular selectivity.^{30,53} Herein, we address these issues and report the fabrication of high-performance H₂/CO₂ separation by a zeolitic membrane prepared by a reactive assembly of sodalite nanosheets hosting hydrogen-sieving six-membered rings (6-MR) of SiO₄ tetrahedra. We report exfoliation of sodalite precursor, RUB-15,¹⁰⁹ leading to a dispersed solution of crystalline 0.8-nm-thick nanosheets (Figure 1.2a). The nanosheets were stacked in a thin film morphology by filtration leading to an intersheet gap with a molecular cutoff of 3.6 Å compared to that of 2.9 Å expected from the 6-MR apertures (Figure 1.2b). The gaps were successfully diminished by the condensation of the terminal silanol groups, which effectively blocked CO₂ transport (Figure 1.2c), leading to a H₂/CO₂ ideal selectivity over 100 at 250–300 °C. The scalable synthesis of high-temperature H₂-

sieving zeolitic membranes is expected to improve the energy efficiency of pre-combustion carbon capture.^{78,96,147–149}

2. Methods

2.1. Materials

The materials employed to synthesis bulk layered RUB-15 were purchased from commercial suppliers. Tetramethylammonium hydroxide, TMAOH, (25% in water, Sigma Aldrich), tetraethylorthosilicate, TEOS, (98% anhydrous, Acros), low-molecular-weight polystyrene (1360 g/mol, Eastman), ethanol (99.9%, Fisher chemicals), hexadecyltrimethylammonium bromide, CTAB, (>98%, Sigma Aldrich), sulphuric acid, (95-97%, Merck). Chlorobenzene (99.8%, Merck). Toluene (99.8%). AAO supports (Smartmembrane and Puyuan nano).

2.2. Synthesis of layered RUB-15.

RUB-15 was synthesized via the hydrothermal synthesis route using a modified method reported by Gies and co-workers¹⁰⁹ and Okubo and co-workers¹⁰⁷. Typically, 112.5 g of TMAOH was mixed with 64.3 g of tetraethylorthosilicate and 128.8 g of deionized water, and the mixture was stirred for 24 h at room temperature. The mixture was then transferred into a rotary evaporator at 40 °C and 100 mbar until the liquid was completely removed. The resulting crystals were stored at 4 °C overnight after which they were dried on a tissue paper at room temperature for 1 day. Next, they were transferred to a Teflon-lined autoclave for heating at 150 °C for up to four weeks. The resulting white powder was thoroughly washed with deionized water until the pH was below 9. The powder was dried at 70 °C.

2.3. Swelling of RUB-15 layers

RUB-15 layers were swollen with hexadecyltrimethylammonium bromide (CTAB) at room temperature. Typically, 3.4 g of CTAB were dissolved in 200 ml of distilled water at neutral pH until the solution became transparent. Subsequently, 1 g of as-synthesized RUB-15 was added to the mixture and was stirred for 24 h. The resulting material was recovered by centrifugation, and the excess CTAB and TMAOH were removed by washing RUB-15 with 4 liters of deionized water. The swollen RUB-15 was dried in an oven at 70 °C.

2.4. Exfoliation of swollen RUB-15

RUB-15 exfoliation was performed by the melt compounding technique as reported by Tsapatsis and co-workers with small modifications.³⁵ Typically, 0.6 g of swollen RUB-15 and 15 g of polystyrene (1360 g/mol) were loaded in a co-rotating twin-screw extruder (Xplore micro compounder) under a nitrogen environment at 120 °C for 30 min with a screw speed of 150 rpm. The temperature was subsequently decreased to 60 °C for 60 min. Finally, the polymer/silicate nanocomposite was extruded at 90 °C.

2.5. Purification of exfoliated RUB-15 nanosheets by DGC

RUB-15 nanocomposite was dissolved in toluene with a nanocomposite concentration of 1.23%. 50 ml PTFE tubes (Beckman Coulter) were filled with 25 ml of chlorobenzene. 25 ml of the nanocomposite solution was slowly added on top of the chlorobenzene. Centrifugation (Beckman Coulter Avanti J-26S XP) at 40000 g-force was carried out for 3 h to settle the nanosheets into a cake. The supernatant was discarded, and the nanosheets were mixed with 50 mL of ethanol. This centrifugation process was repeated twice to remove traces of chlorobenzene. In the end, the supernatant was discarded, and a cake of settled nanosheets was obtained.

2.6. Acid-treatment of purified RUB-15 nanosheets

The acid treatment was carried out by dispersing the nanosheets cake in a 0.2 M solution of sulfuric acid in ethanol. The mixture was kept under stirring at 80 °C for 16 h. Subsequently, the nanosheets were collected by centrifugation (40000 g-force for 3 h). The obtained cake was washed using ethanol (a repeated cycle of dispersion in ethanol followed by centrifugation) until the pH was 7. Finally, tip sonication (Sonopuls mini20) for 30 minutes and centrifugation at 10000 g-force for 10 min were performed to remove large, unexfoliated particles.

2.7. Assembly of nanosheets into a membrane

AAO supports with 20 nm pores were bath sonicated for 30 min in 500 mL of deionized water. Membrane fabrication was carried out by filtration. In a typical experiment, 100 to 500 μ L of the purified nanosheets solution were mixed with 12 mL of fresh ethanol and sonicated for ~25 min. The resulting solution was then centrifuged in 15 mL Falcon tubes at 5000 rpm for 10 min. Gently piped 10 mL from the supernatant were withdrawn and used as a solution for the filtration. The

pressure difference between upstream and downstream of the support was tuned in order to reach a flux of $\sim 2.8 \times 10^{-3}$ mL/s.

After the filtration of the nanosheet solution on the support ended, the AAO was gently removed from the filtration setup and was dried at room temperature for 1 h. The sample was transferred to a convective oven at 70 °C to further remove the remaining ethanol.

2.8. Preparation of calcined RUB-15-based nanosheets membranes

As-filtered membranes were heated in a 3-zone furnace in air at 500 °C for 1 h with a heating and cooling rate of ca. 60 °C/h. Occasional cracks (Figure 1.22 and Figure 1.23) were healed by refiltering a small amount of nanosheets (typically 10 μ L diluted in 12 mL of fresh ethanol). A He trans-membrane pressure of 6 bar was applied, and no visible solvent flow was detected (filtered solvent was evaporating faster than the time needed for the solvent droplets to get out from the tubing system). After a few hours, only a small amount of the solution was filtered, suggesting the presence of only a few defects that could transport the solvent molecules.

2.9. Preparation of calcined RUB-15-based nanosheets membranes using diluted sol-gel derived silica solution

The extremely diluted solution was prepared according to the recipe adopted by Hedlund and coworkers,¹⁵⁰ where they have used an ultrathin silica coating to block defects in MFI membranes for the CO₂/H₂ separation. The silica solution was prepared by the sol-gel method. A mixture of ethanol and tetraethylorthosilicate was vigorously mixed with a solution of water and nitric acid. The clear solution was refluxed for 3 h at 60 °C. The final molar composition was 1TEOS:3.8 Ethanol:6.4 H₂O:0.085 HNO₃. The solution used for dip coating was prepared by diluting 19 times and filtering with a 0.2 μ m syringe filter. The dip-coating was performed immersing and withdrawing the calcined membrane at a rate of 1 mm s⁻¹ with a waiting time of 4 s. The membranes were finally calcined at 500 °C for 1 h with heating and cooling rates of 50 °C/h.

2.10. Gas permeation

Mixed and single gas permeation tests were carried out using a homemade permeation setup (Figure 1.1). Kalrez 7075 O-rings were used to seal membranes to allow gas permeation studies up to 300 °C. Argon was used as the sweep gas. Flow rates of the gases were controlled by mass flow controllers (MFCs). The permeate gas concentration was analyzed in real-time by a mass

spectrometer (Hidden Analytical, HPR-20). Once the steady-state was reached, the permeate concentration data was recorded and averaged (typically 30-60 min for each gas measurement). The gas permeance J_i , the ideal selectivity α_{ij} , and the separation factor β_{ij} were calculated by the following equations (1-3).

$$J_i = X_i / (A * \Delta P_i) \quad (1)$$

$$\alpha_{ij} = J_i / J_j \quad (2)$$

$$\beta_{ij} = (C_i / C_j)_{\text{permeate}} / (C_i / C_j)_{\text{feed}} \quad (3)$$

where X_i is the flow rate of component i , A is the membrane area, ΔP_i is the transmembrane pressure difference for component i , C_i and C_j are the concentrations of component i and j in the feed/permeate streams with i being the faster-permeating component.

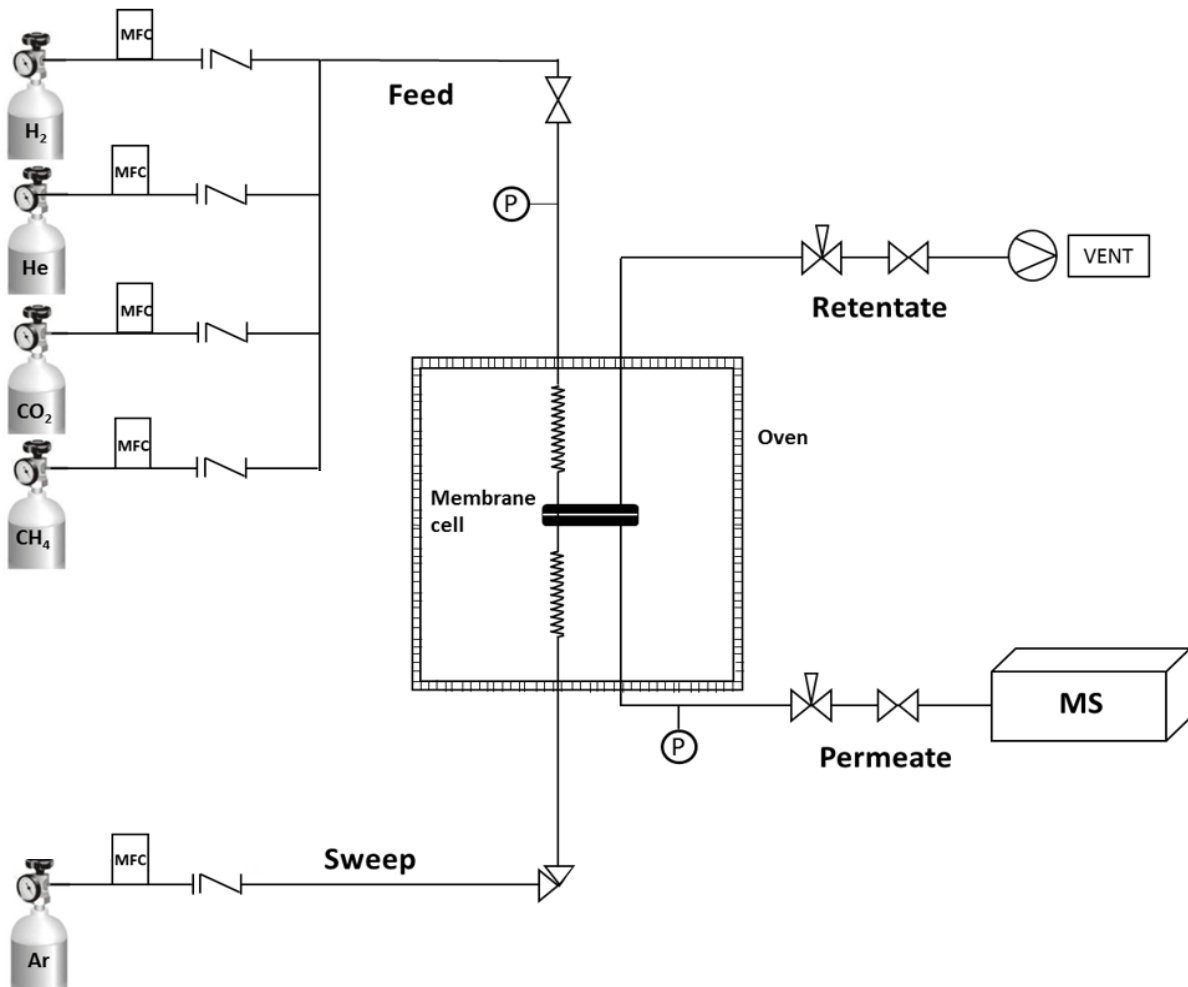


Figure 1.1. Schematic of the homemade permeation setup.

2.11. Ab-initio calculations.

The initial structure of the two-dimensional (2D) RUB-15 surface was taken from the Cambridge Crystallographic Data Centre (CCDC) [ref. no. 1620984]. We removed the TMAOH and water molecules from it and terminated the undercoordinated surface by adding H atoms to the dangling O. Convergence of the energy as a function of the wavefunction and charge density cutoffs as well as of the k point grid was explored. We used 55 Ry and 660 Ry as the wavefunction and charge density cutoffs, respectively. For the k points, we generally used a 1 2 2 Monkhorst-Pack grid (the x -axis corresponds to the direction perpendicular to the surface slab), except for computing the elastic constants (see details below). In order to reach numerical convergence for the relaxation calculations, mixing beta was set equal to 0.2 and mixing_dimension to 8.

To assess the quality of our DFT description, we first computed the cell parameters. For this, we performed a `vc_relax` calculation, where both the nuclei positions and the cell parameters were allowed to relax to their optimal values. Cell parameters are within 1 % of the experimental ones, and the surface area error is of 0.24 %.

2.12. Characterization

Powder XRD patterns were collected using a Bruker D8 Advance using CuK α radiation (λ Cu K α = 1.5406 Å). In-plane and out-of-plane (Figure 1.18a-b) diffraction measurements were conducted on a 9 kW Rigaku Smartlab diffractometer with a Cu target (45 kV, 200mA). The measurements were taken in parallel beam mode. The incident angle was set to 0.3°, and the incident slit height was 0.5 mm. A parallel slit collimator and analyzer of 0.5° respectively, were used. A Hypix 3000 detector in 0D mode was mounted on the in-plane arm, which allowed the samples to remain stationary.

SEM images were collected using an FEI Teneo scanning electron microscope at an acceleration voltage of 1-2 kV. Samples were imaged without using any conductive coatings.

TEM images were collected using an FEI Tecnai G2 Spirit microscope operating with 120 keV incident electron beam. Low-dose HRTEM was performed on a Cs-corrected FEI cubed G2 Titan 60-300 electron microscope at 300 kV, using a Gatan K2 direct-detection camera in electron counting mode. The HRTEM images were acquired with the dose fractionation function, and each image stack is composed of 120 frames with 0.05 s exposure for each frame, with a total electron

dose of $\sim 60 \text{ e}^- \text{ \AA}^{-2}$. The raw image was denoised by using an Average Background Subtraction Filter (ABSF) filter. The CTF correction was performed base on the defocus value determined from the amorphous thon rings in the Fourier transform, and the projected electrostatic potential was simulated by the QSTEM software (QSTEM V2, 31; www.qstem.org).

AFM measurements were done on a Bruker Dimension FastScan operated in the ScanAsyst mode with ScanAsyst-Fluid+ probes (resonant Frequency of 150 kHz, spring constant of 0.7 N/m, length of 70 μm , and width of 10 μm) at room temperature.

AFM samples were prepared by spin coating of RUB-15 nanosheets on a freshly cleaved mica substrate.

The Fourier transform infrared (FT-IR) measurements were carried out with a Spectrum Two FT-IR spectrometer (PerkinElmer) in which both background and sample spectra were recorded 32 times.

^{29}Si solid-state nuclear magnetic resonance (NMR) measurements of as-synthesized layered RUB-15 (powder) were performed on a 400 MHz Avance III spectrometer. RUB-15 powder was packed into a 3.2 mm zirconium rotor and the experiments were run at a spin rate of 5 kHz and $\pi/2$ radio frequency pulse of 13.5 μs with a relaxation delay of 150 s.

^{29}Si solid-state NMR experiments for the as-filtered and the calcined nanosheet films were carried out on a 900 MHz wide-bore magnet equipped with an Avance Neo console and 3.2 mm low-temperature cross-polarization magic angle spinning NMR probe. The membranes were packed into 3.2 mm rotors without any further processing. Experiments were run at a spin rate of 15 kHz. In order to obtain quantitative measurements on the amount of Q3 and Q4 sites, echo detected measurements ($\pi/2$ - τ - π - τ) were done with an echo delay τ of 1 rotor period and a $\pi/2$ radio frequency pulse of 4.9 μs with a relaxation delay of 150 s. The echo was used to remove any ^{29}Si background in the probe. In order to identify the kinds of Si bonding motifs present in the membranes, a higher sensitivity NMR measurement was done using cross-polarization (CP),^{151,152} in which spin magnetization is transferred from ^1H to ^{29}Si . CP measurements were done using a contact time of 10 ms with a pulse repetition time of 0.5 s.¹⁵³

3. Results and discussions

3.1. Gas diffusion through 6-Membered Si-tetrahedra rings

The layered RUB-15 was first reported by Gies and co-workers as a potential precursor to sodalite.¹⁰⁹ Okubo and co-workers successfully demonstrated the conversion to sodalite by a topotactic condensation of shifted RUB-15 layers,^{107,110} making RUB-15 promising for the synthesis of all-silica sodalite membrane. The as-synthesized RUB-15 layers have a chemical composition of $[(\text{N}(\text{CH}_3)_4)_8(\text{Si}_{24}\text{O}_{52}(\text{OH})_4) \cdot 20\text{H}_2\text{O}]$ where tetramethyl ammonium (TMA^+) ions act as the organic structure-directing agent (OSDA). RUB-15 layers possess an orthorhombic lattice and an *Iba2* space group symmetry with layers stacked along the *a*-axis with unit cell parameters $a=27.905 \text{ \AA}$, $b=8.408 \text{ \AA}$, and $c=11.518 \text{ \AA}$ (Figure 1.3).

The reflection conditions are as follows: hkl , $h+k+l=2n$; $0kl$, $k, l=2n$; $h0l$, $h, l=2n$; and $hk0$, $h+k=2n$. The individual silicate layers in RUB-15 are composed of hemihedral cavities formed by atomically bridged arrays of 4- and 6-MR of SiO_4 tetrahedra resembling one-half of the sodalite cage (Figure 1.2d). The 6-MR of sodalite is widely accepted to be permeable to H_2 .^{99,104,154} For example, using molecular dynamics (MD) simulations, van der Berg et al. reported the energy barrier for H_2 diffusion across all-silica sodalite to be 32.9 kJ/mole.⁹⁹ To calculate the energy barrier for the transport of H_2 and CO_2 across the 6-MR of RUB-15, we performed density functional theory (DFT) calculations using the open-source Quantum Espresso 6.1 software¹⁵⁵ considering the GGA/PBE functional¹⁵⁶ and applying the Grimme-D2¹⁵⁷ scheme to take into account dispersion corrections (details in Supplementary Information). The structure of an isolated RUB-15 nanosheet terminated by silanol groups was allowed to relax in terms of both the position of the nuclei and the cell parameters, yielding *b*- and *c*-axis parameters of 8.49 and 11.44 \AA , and α angle of 90.06° , within 1% of the experimental data.¹⁰⁹ The stability conditions for a two-dimensional material were met, indicating that the isolated RUB-15 would be mechanically stable (Note 1 Appendix I, Table 1.1). To compute the energy barrier for gas diffusion, nudged elastic band (NEB) calculations¹⁵⁸ were performed covering the path between the gas phase and the adsorption site located on the other end of the surface, across the pore (Figure 1.2e, Note 2 Appendix I). All nuclei were allowed to relax, including those forming the RUB-15 lattice. The climbing image scheme was used to obtain more reliable values for the activation energies, and the endpoints of the NEB configurations were kept fixed to the initially optimized values. The calculated activation energy, E_{act} , of H_2 from its adsorbed state was $39 \pm 2 \text{ kJ/mole}$. The corresponding apparent activation energy, $E_{act-app}$, defined as the sum of adsorption energy and activation energy from the adsorbed state, was $33 \pm 2 \text{ kJ/mole}$.

A slight expansion of the 6-MR is observed when H₂ is located at the center of the ring (Supplementary Movie 1), which seems to assist its diffusion. CO₂ required a much larger E_{act} of 117±5 kJ/mole, suggesting that RUB-15 is indeed promising for sieving H₂ and other smaller molecules such as He and NH₃ from larger molecules such as CO₂, N₂, and CH₄.

Table 1.1. Computed elastic constants of the RUB-15 nanosheet.

Elastic constants	[GPa nm]
C ₁₁	18.4
C ₂₂	12.8
C ₁₂	9.0
C ₆₆	48.1

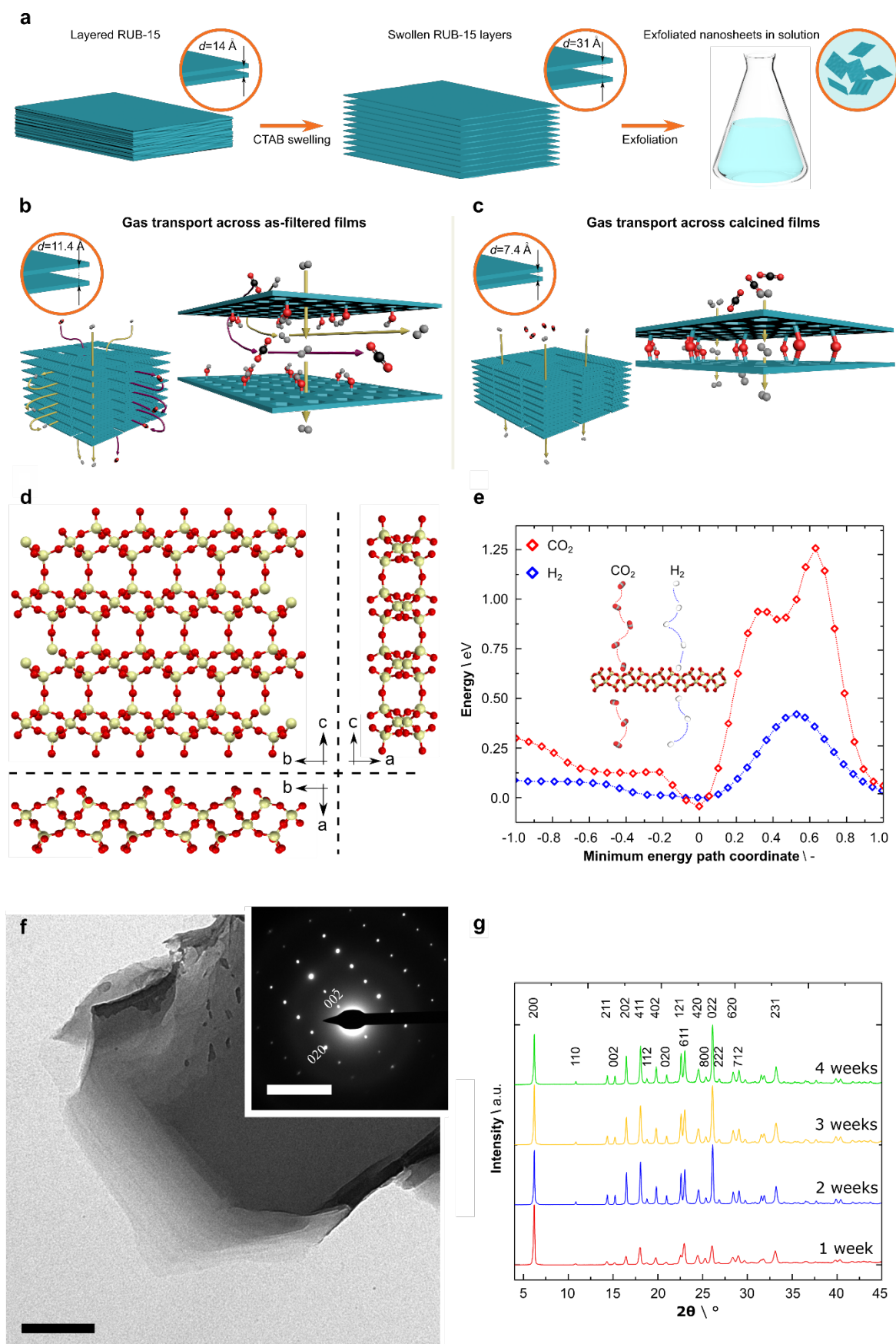


Figure 1.2. RUB-15 framework as an attractive candidate for the fabrication of hydrogen sieving membranes. a-c, Illustration of processing of RUB-15 into H_2 sieving membranes. a) RUB-15 layers are swollen to increase the d spacing from 14 to 31 \AA . Melt compounder-based exfoliation yields 8- \AA -thick single-layers which are

subsequently dispersed in polar solvents upon sulfuric acid treatment. b) Filtration-based assembly of the exfoliation nanosheets leads to an ordered stacking with a d spacing of 11.4 Å. The interlayer spacing is small enough to allow sieving of H₂ from CH₄ and N₂ but not from CO₂. c) Upon calcination, the neighboring terminal silanol groups condense, decreasing the d spacing to 7.4 Å, blocking the CO₂ transport while H₂ diffuses across the 6-MR apertures. d) The structure of RUB-15 layer. Si and O are shown in yellow and red, respectively. H and interlayer guests are omitted for clarity. e) Potential energy along the minimum energy path coordinate for the adsorption of molecules on a single RUB-15 nanosheet (reaction coordinate value from -1 to 0) and the transport of H₂ and CO₂ across the 6-MR (reaction coordinate between 0 and 1). f) TEM image of as-synthesized RUB-15 layers. The corresponding ED pattern is shown in the inset. Scale bars in the panel and the inset correspond to 200 nm and 5 nm⁻¹, respectively. g) Powder XRD patterns (λ Cu K α = 1.5406 Å) from as-synthesized RUB-15 as a function of the transformation time.

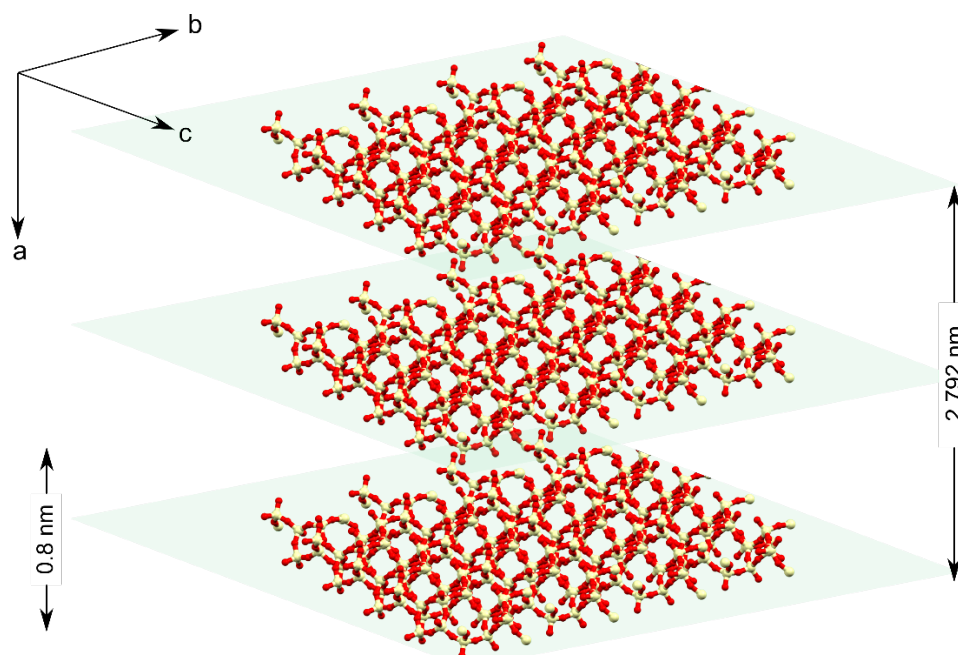


Figure 1.3. Structure for the layered RUB-15. The bc planes are highlighted in green to illustrate the layered structure. Si: yellow; O₂: red. H₂ and interlayer guests are omitted for clarity. The unit-cell dimension along the a-axis is noted as 2.792 nm, whereas the thickness of each sheet is ca. 0.8 nm.

3.2. Synthesis of single layer RUB-15 nanosheets

The layered RUB-15 was crystallized by a pseudo-solid-state transformation of hydrated silicate double-four-ring by heating in a closed autoclave at 150 °C,¹⁰⁷ leading to layers with plate-like morphology (Figure 1.2f and Figure 1.4).

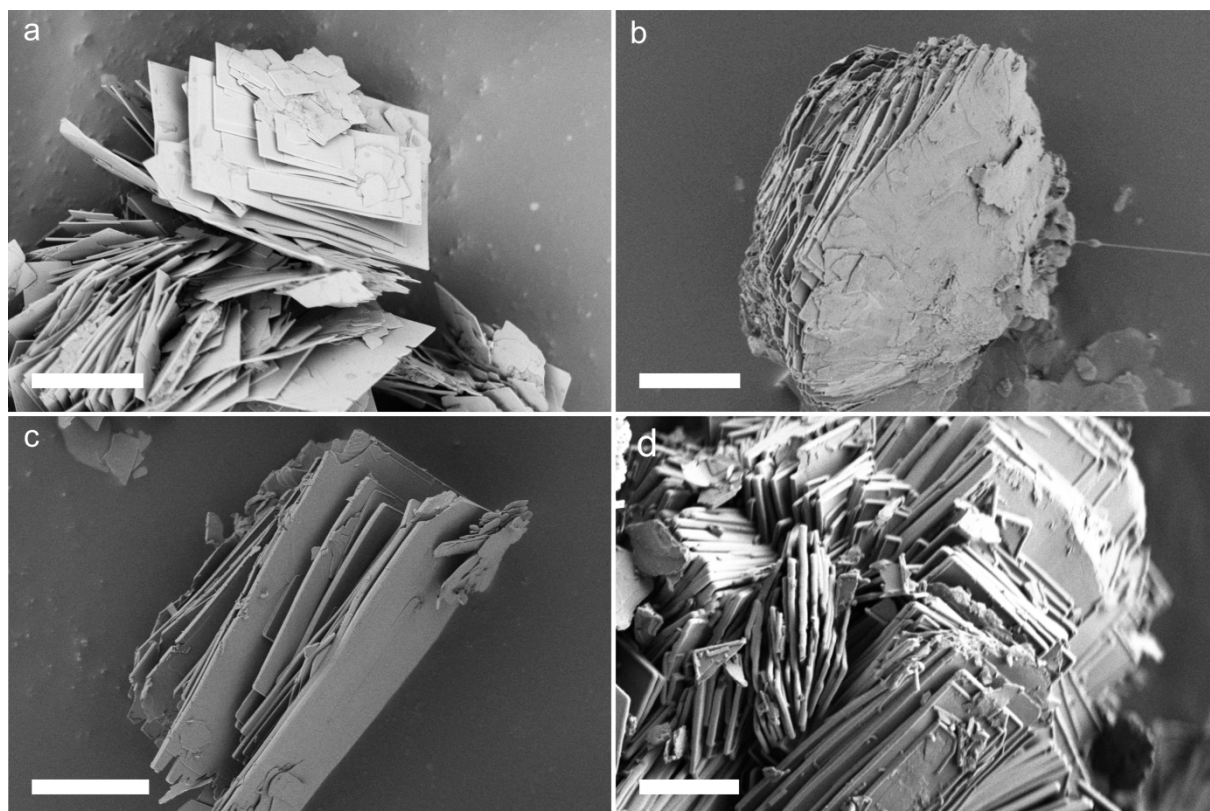


Figure 1.4. The morphology of as-synthesized RUB-15 layers. SEM image of layered RUB-15 after a) one, b) two, c) three, and d) four weeks of hydrothermal synthesis. The scale bars correspond to 10 μm .

Selected area electron diffraction (SAED) pattern indicated that as-synthesized layers were highly crystalline (inset of Figure 1.2f). This was confirmed by powder X-ray diffraction (XRD) studies with crystallinity improving by extending the transformation for two weeks or more (Figure 1.2g, Table 1.2 and Table 1.3).

Table 1.2. Comparison of the reflections expected from RUB-15 against our experimental XRD data.

Reflections	CCDC 1620984	XRD data	$ \Delta(2\theta) $
hkl	reflections $2\theta [^\circ]$	$2\theta [^\circ]$	$[^\circ]$
200	6.33	6.23	0.10
110	10.99	10.84	0.15
002	15.38	15.24	0.14
202	16.65	16.5	0.15
411	18.22	18.07	0.15
112	18.94	18.78	0.16
402	19.98	19.81	0.17

312	20.99	20.99	0.00
121	22.73	22.59	0.14
611	23.17	23.01	0.16
321	24.48	24.55	0.07
800	25.53	25.39	0.14
022	26.23	26.13	0.10
222	27.01	26.84	0.17
413	28.57	28.41	0.16
712	29.23	29.07	0.16
123	31.71	31.56	0.15
721	31.88	31.9	0.02
820	33.36	33.2	0.16

Table 1.3. Comparison of the reflections expected from RUB-15 against our experimental SAED data.

Reflections hkl	CCDC 1620984 <i>d</i> spacing [nm⁻¹]	SAED Data [nm⁻¹]	 $\Delta(d \text{ spacing})$ [nm⁻¹]
002	5.759	5.60	0.16
020	4.204	4.48	0.28
022	3.395	3.27	0.13

No significant changes were observed beyond two weeks, and therefore, the two-week samples were used for further experiments (Note 3 Appendix I, Figure 1.5 and Figure 1.6).

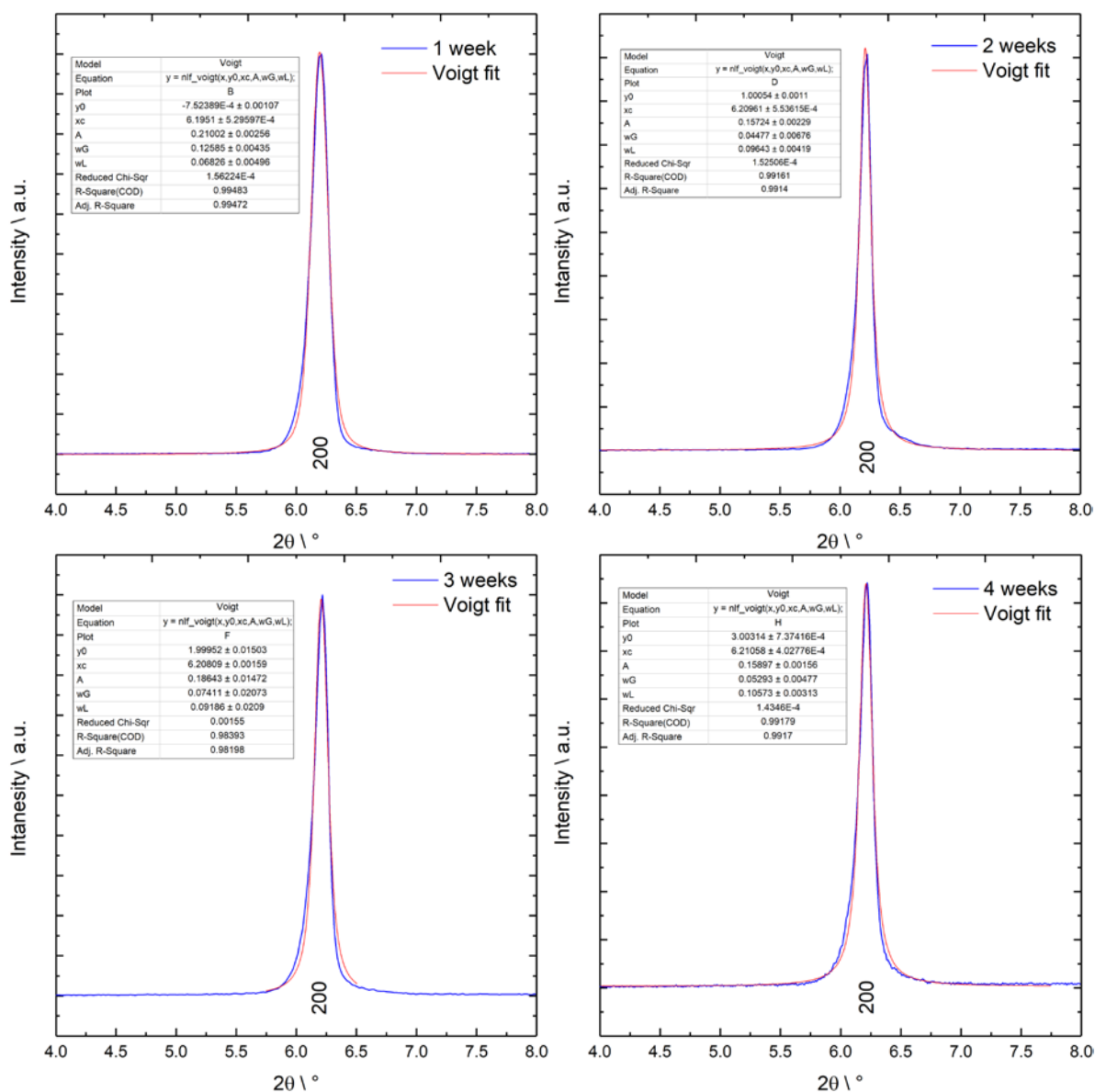


Figure 1.5. PXRD patterns (λ Cu K α = 1.5406 Å) of the layered RUB-15, showing a peak representing the 200 plane with corresponding Voigt fit for 1, 2, 3, and 4 weeks synthesis time.

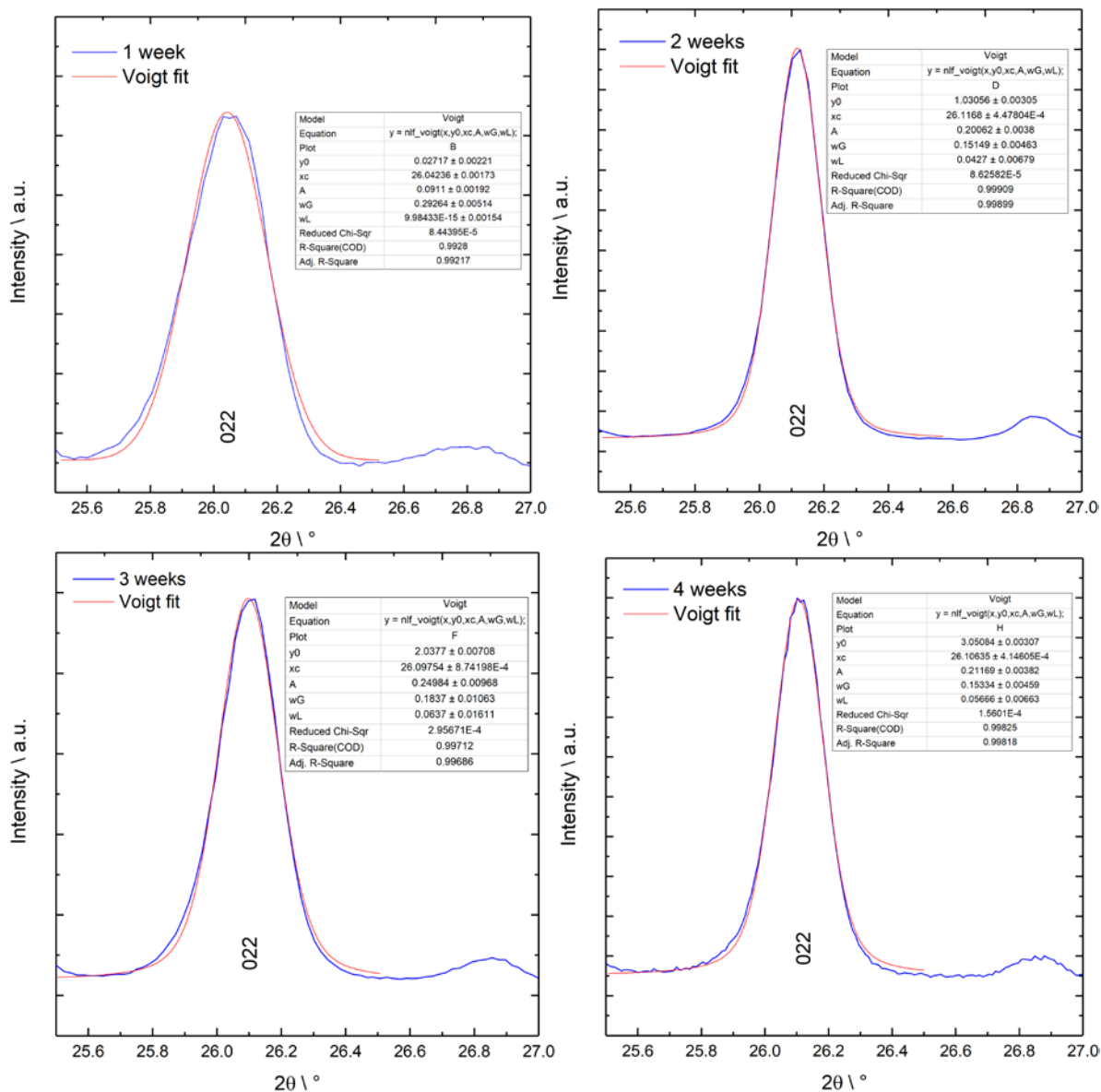


Figure 1.6. PXRD patterns (λ Cu K α = 1.5406 Å) of the layered RUB-15, showing a peak representing the 022 plane with corresponding Voigt fit for 1, 2, 3, and 4 weeks synthesis time.

The ^{29}Si magic-angle spinning nuclear magnetic resonance (MAS NMR) confirmed the 2:1 ratio of Q^3/Q^4 ratio expected in the fully crystallized RUB-15 layers (Figure 1.7).

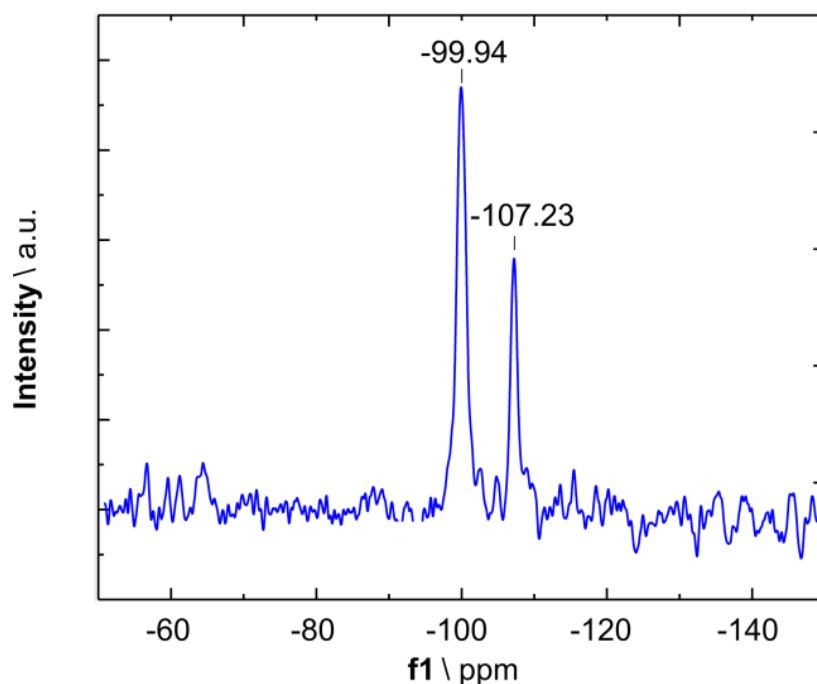


Figure 1.7. Solid-state ^{29}Si MAS NMR spectrum from the as-synthesized RUB-15 layers revealing the two prominent peaks at Q^4 (-107.23 ppm) and Q^3 (-99.94 ppm).

Thermogravimetric analysis (TGA) of the as-synthesized layers in air indicated that the material hosted ca. 40% of interlayer water and OSDA, consistent with the theoretical chemical composition (Figure 1.8).

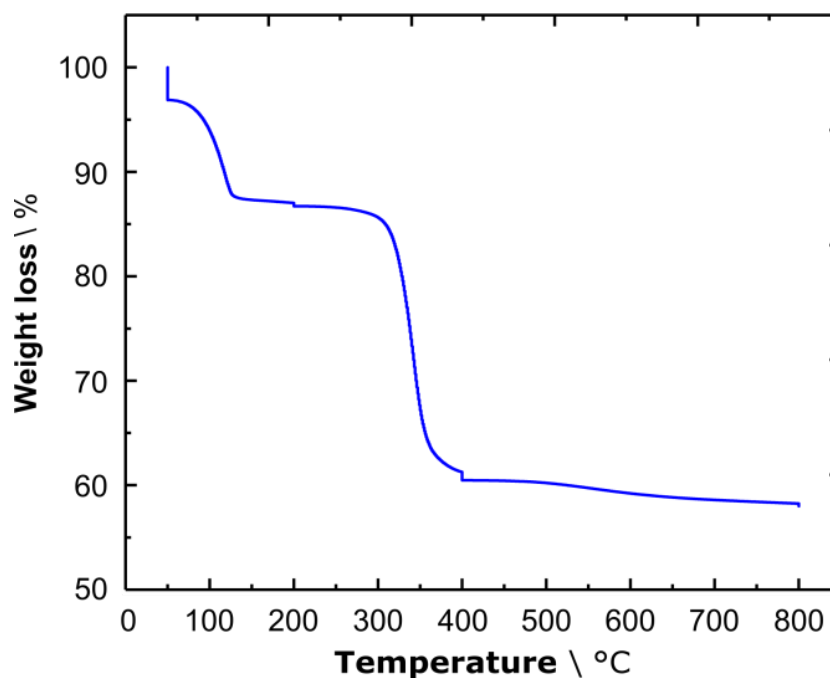


Figure 1.8. Thermogravimetric analysis of the as-synthesized RUB-15 layers with a heating rate of 5 °C/min in air flow from 25 °C to 800 °C. The weight loss corresponds to i) non-structural water molecules, ii) water molecules hosted in gallery spacing, iii) OSDA, and (iv) weight loss associated with the silanol condensation.

The interlayer spacing between the as-synthesized RUB-15 layers, indicated by the 200 peak, was 1.4 nm (Figure 1.9a). To weaken the interlayer interactions for the eventual exfoliation, the RUB-15 layers were swollen with cetyltrimethylammonium bromide (CTAB). The swelling was carried out at room temperature and at a neutral pH to prevent any structural damage to RUB-15.

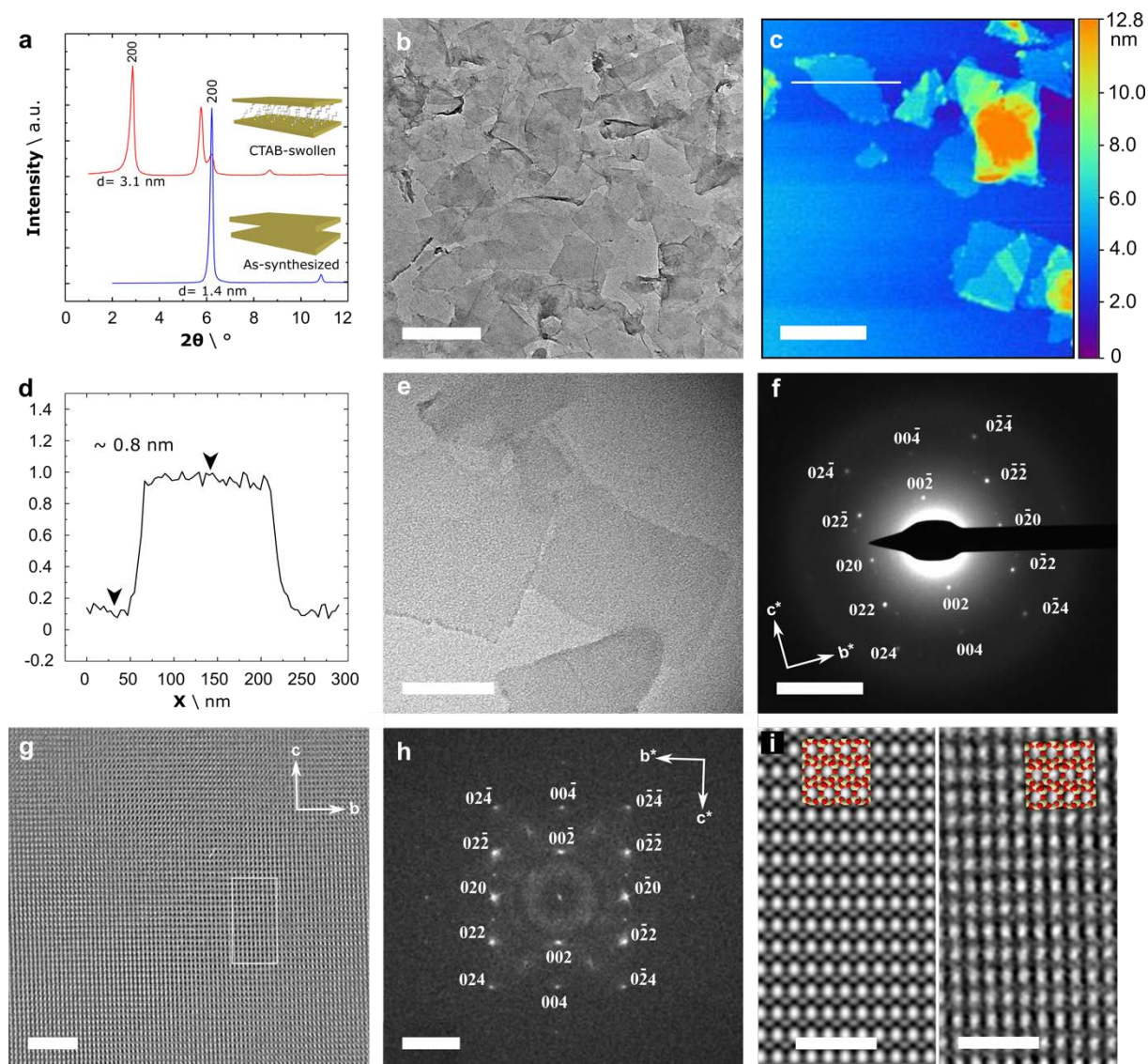


Figure 1.9. Characterization of exfoliated RUB-15. a) Powder XRD pattern (λ Cu $K\alpha$ = 1.5406 Å) from the surfactant-swollen and as-synthesized RUB-15. The inset shows corresponding illustrations. b) Low-magnification TEM image of exfoliated nanosheets. c) Tapping-mode AFM topographical image of exfoliated RUB-15 nanosheets d) Height profile across a nanosheet shown in (c). e) High-magnification TEM image of the exfoliated nanosheets. f) SAED pattern of an exfoliated nanosheet along the [100] zone axis. g), Denoised HRTEM image of the exfoliated nanosheet lying flat on the 0kl plane. h) Fourier transform of (g). i) Left: simulated projected potential map along the [100] direction of RUB-15 with a point spread function width of 2 Å. Right: contrast transfer function (CTF)-corrected image of the highlighted area in (g) based on a defocus value of -260 nm that is determined from the thon rings in the Fourier transform pattern. Scale bars; b, 250 nm, c, 200 nm, e, 100 nm, f, 3 nm⁻¹, g, 5 nm, h, 2 nm⁻¹, i, 2 nm.

A RUB-15/CTAB weight ratio of 1/3.4 ensured a 1.6-fold higher CTAB compared to the stoichiometric TMA⁺ in the gallery spacing. A successful swelling was confirmed with d spacing increasing from 1.4 to 3.1 nm, with a corresponding expansion of the gallery spacing from 0.6 to 2.3 nm (Figure 1.9a). The peak at $2\theta = 3^\circ$ represents the first-order reflection of d spacing from the swollen layers, while the peaks at 2θ of 6 and 9° represent the second and third-order reflection peaks, respectively. At room temperature, a majority of the RUB-15 layers could be swollen. The peak at 2θ of 6.3° was essentially the 200 peak of un-swollen layers (Figure 1.9a, Figure 1.10, and Figure 1.11).

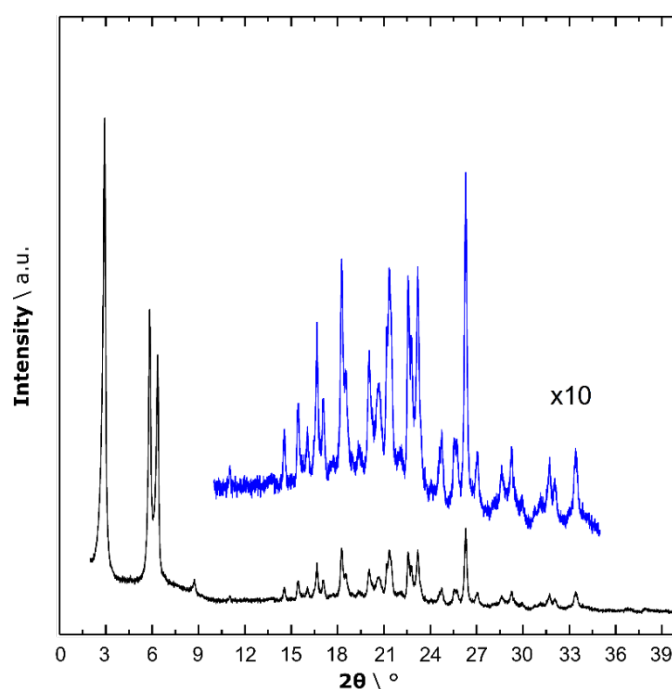


Figure 1.10. Wide-angle powder XRD (λ Cu K α = 1.5406 Å) from the RUB-15 layers swollen at room temperature.

A complete swelling could be achieved at 85 °C, where this peak disappeared (Figure 1.11). Subsequently, the swollen layers were exfoliated by the polymer melt compounding route¹⁵⁹ using a low molecular weight polystyrene (M.W. of 1360 g/mol). Briefly, the temperature of the polystyrene melt was varied to regulate the melt viscosity, and therefore, the diffusivity of the polymer chains in the swollen RUB-15 layers as well as the shear force between the entangled polymer chain and the nanosheets, which led to exfoliated RUB-15 nanosheets embedded in the polymer matrix.

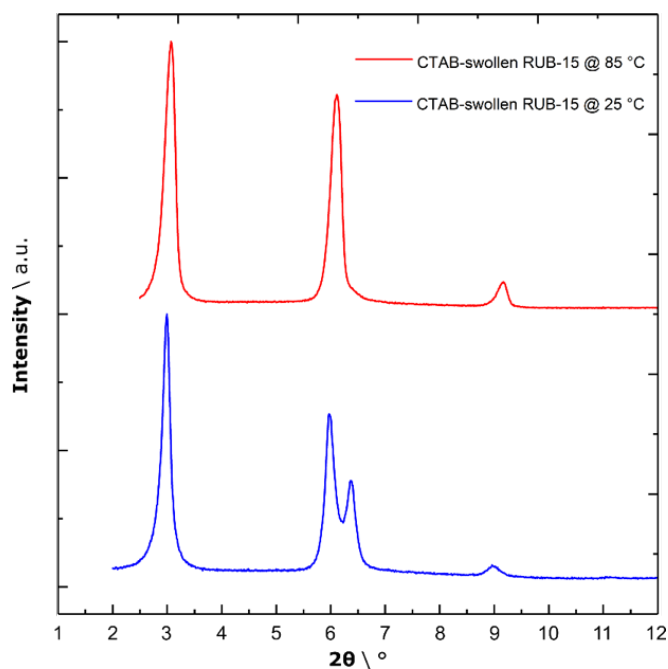


Figure 1.11. Powder XRD patterns (λ Cu $K\alpha = 1.5406$ Å) from the RUB-15 layers swollen at 25 and 85 °C.

The extraction and purification of the exfoliated RUB-15 nanosheets from the polystyrene matrix (Figure 1.12) were carried out by dissolving the matrix in toluene followed by density-gradient-centrifugation (DGC).⁸⁸



Figure 1.12. Picture of the exfoliated RUB-15 embedded in the polymer matrix. Ca. 10 g were obtained by a single processing. The scale bar corresponds to 30 mm.

The resulting nanosheets could be dispersed in ethanol after the ion exchange of CTAB with H^+ by stirring the nanosheets in 0.2 M solution of sulfuric acid solution in ethanol at 80 °C for 16 h (Figure 1.13). Extremely thin nanosheets with an average lateral size of 205 ± 62 nm, calculated by taking

the square root of the average nanosheet area, were observed by transmission electron microscopy (TEM, Figure 1.14, and Figure 1.9b and Figure 1.9e).



Figure 1.13. The Tyndall effect observed from the colloidal suspension of RUB-15 nanosheets dispersed in ethanol. The scale bar corresponds to 10 mm.

The crystalline structure of the nanosheets was preserved during exfoliation as indicated by the SAED pattern along the [100] zone axis (Figure 1.9f), which also confirmed that the nanosheets oriented along *a*-out-of-plane axis. This is highly desirable for the fabrication of membranes with a short molecular diffusion path. Atomic force microscopy (AFM) images of exfoliated nanosheets confirmed that the nanosheets were indeed single-layer (Figure 1.9c-d) with a thickness of ca. 0.8 nm, agreeing well with the structure of the nanosheets (Figure 1.3).

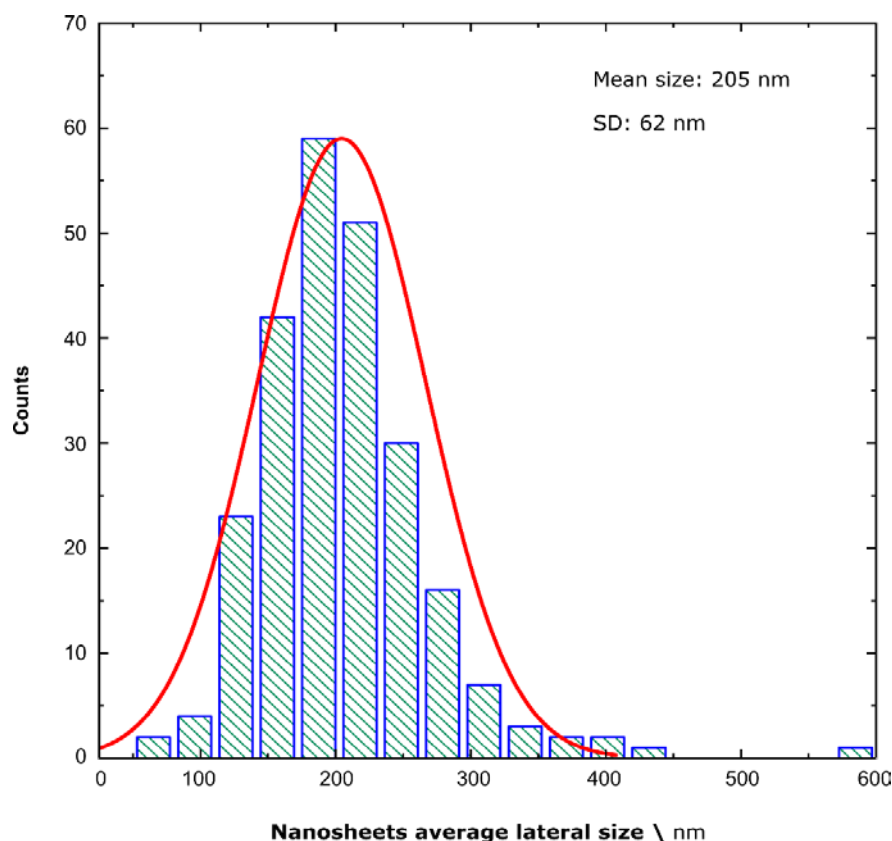


Figure 1.14. Lateral size distribution of the exfoliated nanosheets with a gaussian fit. To avoid the misjudgment of short and long edges of some irregular nanosheets, we proceeded with the area measurement of each nanosheet and then took its square root to obtain an average lateral size, which results in a single distribution.

The structure of nanosheets was revealed with high-resolution TEM (HRTEM) imaging along the [100] crystallographic direction. HRTEM was performed under low-dose conditions that effectively limited electron beam-induced structural damage.^{160,161} The obtained HRTEM image (Figure 1.9g) reveals the high crystallinity of the nanosheet, and the corresponding Fourier transform confirms that it is of the RUB-15 structure and oriented along the [100] direction (Figure 1.9h). The angle between the b^* and c^* directions in the Fourier transform deviates to ca. 89° , which can be attributed to the electron-beam damage as well as the contribution from lens distortions. We processed the HRTEM image by correcting the effect of the contrast transfer function (CTF) of the objective lens to make the image contrast more interpretable. The CTF-corrected image (Figure 1.9i, right) agrees well with the simulated [100]-projected electrostatic potential map of RUB-15 (Figure 1.9i, left), showing an ordered arrangement of the 6-MR apertures, although the smaller 4-MR are not clearly resolved due to the limited information transfer of the image. The slight deviation from a right angle restricts the ability to superimpose the projection of the structure model on the CTF-corrected image to only onto a small domain

(Figure 1.9i, right). On the other hand, for the simulated [100]-projected electrostatic potential map of RUB-15, a better match with the projection of the structure model was obtained.

3.3. Nanosheets membrane assembly and condensation

The nanosheets could be assembled to form a thin film on a porous support (AAO, anodic aluminum oxide) using vacuum filtration (Figure 1.15a). Due to their high aspect ratio, the nanosheets rested flat on the supports with an α -out-of-plane orientation (Figure 1.15b), consistent with the TEM observation.

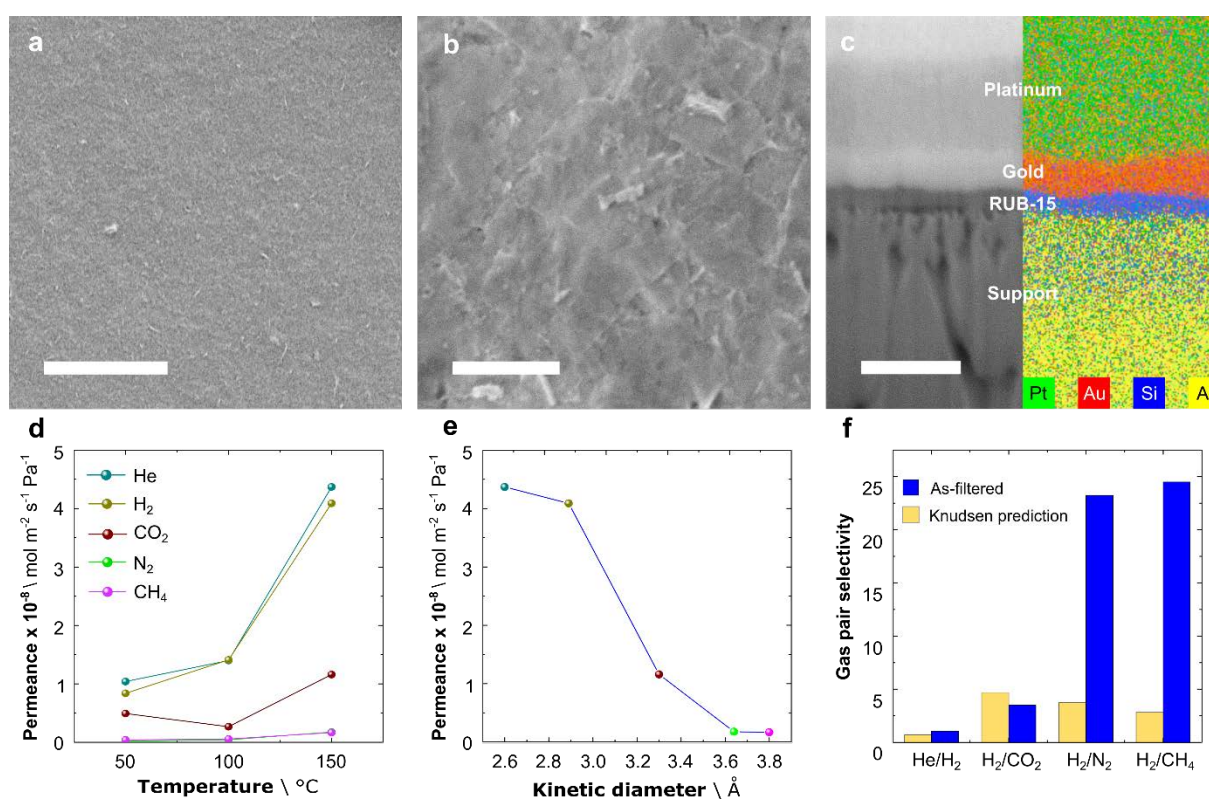


Figure 1.15. Characterization of the as-filtered RUB-15 nanosheet film. a) Low- and b) high-magnification SEM images of the as-filtered nanosheet films. c) Corresponding cross-sectional image of the film. Left-side is the SEM image, and the right side is elemental mapping overlaid on top of the SEM image. Pt and Au were used as protective coatings. Al corresponds to the underlying alumina support. d) Single-gas permeation data as a function of temperature. The relative plot of $\ln(\text{permeance})$ vs $1/T$ is reported in Figure 1.17. e) Permeation as a function of the kinetic diameter of gases at 150 $^{\circ}\text{C}$. f) Ideal gas selectivities from the as-filtered membranes at 150 $^{\circ}\text{C}$ compared to the theoretical Knudsen selectivity. Scale bars; a, 5 μm , b-c, 500 nm.

Pinhole-free and compact films with a thickness of ca. 300 nm could be prepared, as revealed by the cross-section prepared by focused-ion beam (FIB) (Figure 1.15c, left), while the energy dispersive X-ray (EDX) analysis on the same cross-section helped to identify the RUB-15 layer (Figure 1.15c, right). A uniform film could be obtained in a centimeter-scale area (Figure 1.16).

The stacking of nanosheets on top of each other led to an intersheet spacing of 11.4 Å (Figure 1.18a), corresponding to a gallery spacing of ca. 3.4 Å.



Figure 1.16. A picture of the assembled RUB-15 nanosheets on the AAO support. The scale bar corresponds to 1 cm.

This gallery spacing acted as a parallel transport pathway for the gases along with the 6-MR of the RUB-15 layer. As a result, a high H_2/CO_2 selectivity, expected from the NEB calculations, was not realized. Although the permeance of H_2 from the as-filtered films was somewhat activated corresponding to an $E_{act-app}$ of ca. 20 kJ/mole (Figure 1.17), the $E_{act-app}$ was much lower than that calculated by NEB for H_2 transport across 6-MR (33 ± 2 kJ/mole), confirming that the intersheet gallery spacing dominated the overall gas transport. Indeed, the molecular cutoff was closer to 3.6 Å, and not around 2.9 Å as expected from the 6-MR (Figure 1.15d-f). Therefore, while the H_2/CO_2 ideal selectivity was low, the H_2/N_2 and H_2/CH_4 ideal selectivities were above 20 (Figure 1.15f), much higher than the corresponding Knudsen selectivities (3.7 and 2.8, respectively).

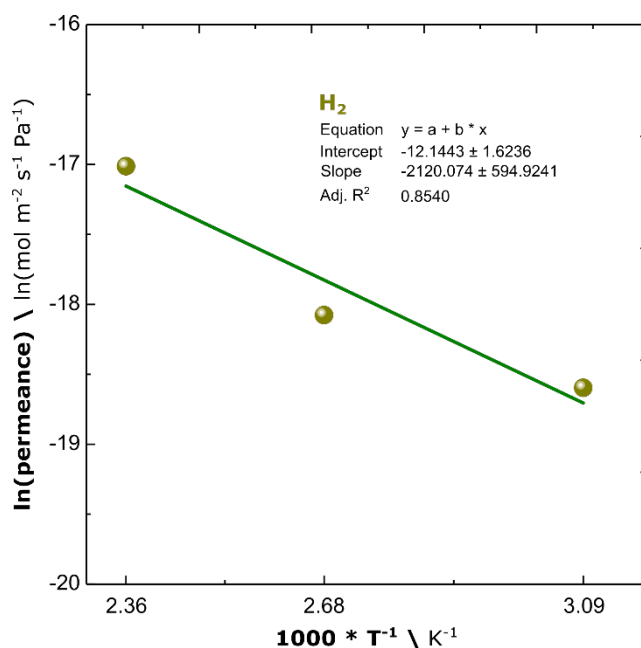


Figure 1.17. Arrhenius plot showing temperature-dependence of H₂ permeance from the nanosheet film before calcination, as reported in Figure 1.15d.

The presence of reactive terminal silanol groups in the zeolite precursor nanosheets presents a unique opportunity for the reduction of intersheet gaps allowing one to block the nonselective molecular transport along the gallery spacing. The neighboring silanol groups can be condensed by simple heating to form covalent Si-O-Si linkages, which can reduce the intersheet gaps, thereby blocking the molecular transport along these gaps. Indeed, calcination of the as-filtered nanosheets film in air led to a shift of the periodic interlayer spacing from 11.4 Å to 7.4 Å (XRD data, Figure 1.18a). It is noteworthy that the interlayer spacing post-calcination is slightly smaller than the nanosheet thickness and is attributed to the condensation reaction between neighboring layers, which produces a water molecule. The turbostratic arrangement of the assembled nanosheets prevents a complete/uniform condensation of the silanol groups, which explains the broadened interlayer-spacing peak. In-plane XRD on the as-filtered membranes showed three distinct peaks relative to the 002, 020, and 022 planes (d spacing adapted from lattice parameters of relaxed nanosheet structure, Table 1.4), which is in agreement with the nanosheet orientation along the a -out-of-plane axis (Figure 1.18b). Upon calcination, the 020 and 022 plane reflections were distinguishable, indicating the preservation of in-plane periodic order.

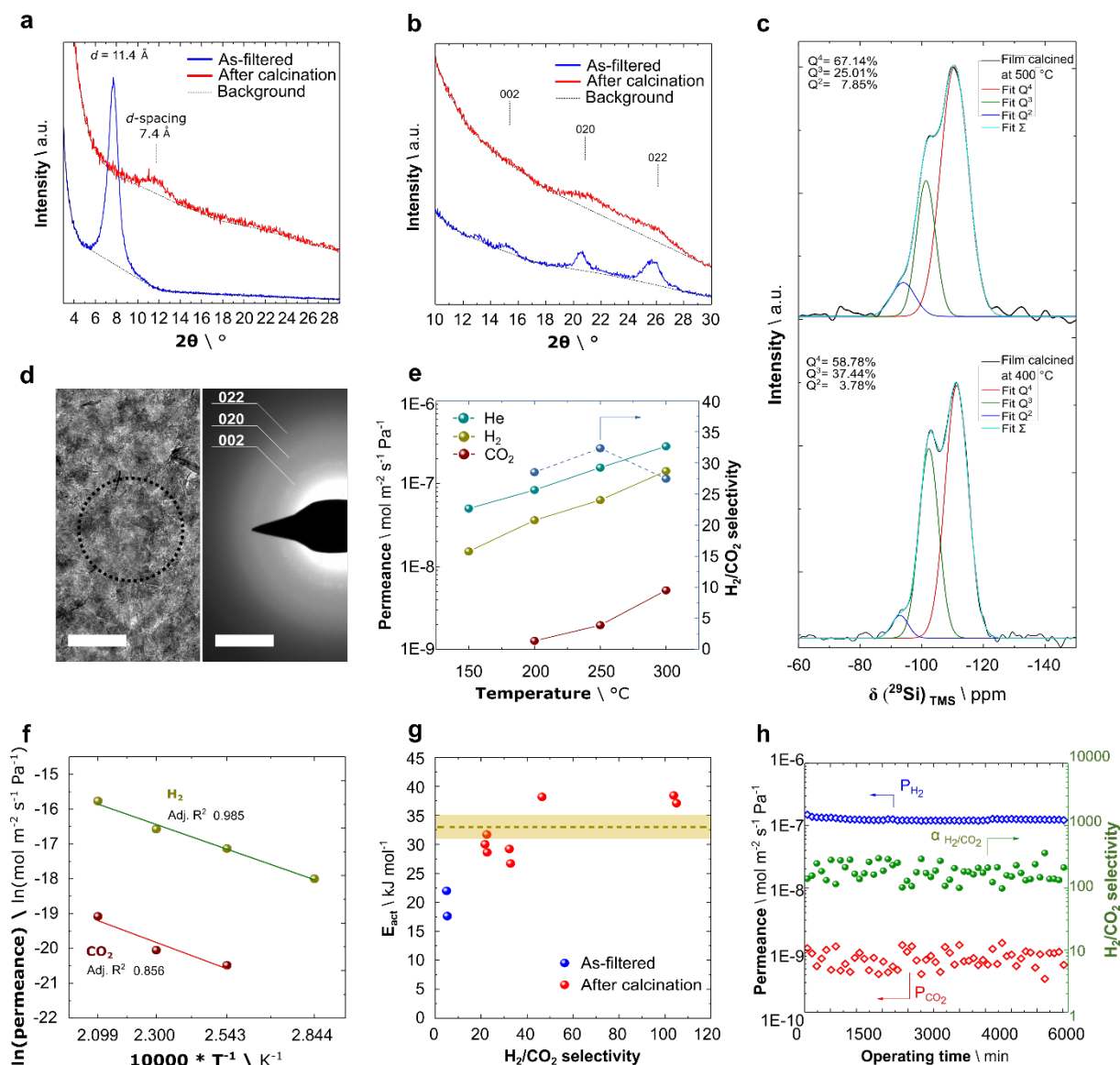


Figure 1.18. Characterization of the calcined RUB-15 nanosheet film. Comparison of the out-of-plane a) and in-plane b) XRD pattern (λ Cu $K\alpha = 1.5406$ Å). c) ^{29}Si MAS solid-state NMR from the films of exfoliated nanosheets calcined at 400 °C (bottom) and 500 °C (top). The data were deconvoluted with a symmetric Gaussian profile, and the relative percentages of the Q^2 , Q^3 , and Q^4 peaks at -92.1, -101.1, and -110.8 ppm, respectively, are shown. d) TEM image of a calcined nanosheet film (left) and the corresponding SAED pattern (right). (e), Single-gas permeation data from the calcined nanosheets membranes as a function of temperature. (f) The plot of $\ln(\text{permeance})$ vs. $1/T$ from data in (e) for H_2 and CO_2 . g) $E_{\text{act-app}}$ for H_2 as a function of the H_2/CO_2 ideal selectivity. The horizontal band represents $E_{\text{act-app}}$ from the NEB calculations. h) 100 h stability test with an equimolar H_2/CO_2 mixture feed in the presence of 4% water vapor at 200 °C. Scale bars in d are 1 μm (left) and 2 nm^{-1} (right).

Cross-sectional images of films before and after the calcination step revealed a slight decrease in the film thickness consistent with a decrease in the gallery spacing (Figure 1.19). A comparison of the Fourier-transformed infrared (FTIR) spectra from the as-filtered and the calcined films reveals that the broad peak around 3300 cm^{-1} , associated with the O-H stretching vibrations of the silanol group of RUB-15,^{110,162} diminished after calcination (Figure 1.20).

Table 1.4. d spacing obtained by Gaussian fit to the peaks, corresponding R^2 , and comparison to the d spacing from DFT-calculations-derived lattice parameter.

h	k	l	d spacing extracted from Gaussian fit [Å]	R^2 for Gaussian fit	d spacing based on DFT- derived lattice parameter [Å]
0	0	2	5.77 ± 0.03	0.692	5.72 ± 0.06
0	2	0	4.31 ± 0.01	0.936	4.24 ± 0.04
0	2	2	3.44 ± 0.01	0.968	3.41 ± 0.03

^{29}Si MAS solid-state NMR was performed on the layered RUB-15 and on the nanosheet films calcined at two different temperatures (i.e., 400 and 500 °C) to capture the evolution of silanol condensation (Figure 1.18c). As-synthesized layered RUB-15 displays a quantitative Q^3/Q^4 ratio of 2:1.

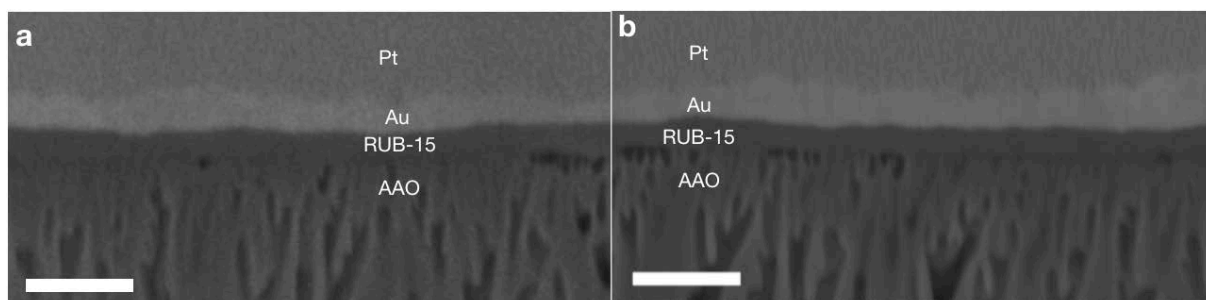


Figure 1.19. SEM images of the cross-section of RUB-15 films, (a) as-filtered, and (b) post calcination. The scale bars correspond to 200 nm. The cross-section specimen was prepared from the same as-filtered film by gently cutting the membrane in two parts. One part was imaged as it is (a), and the other part was calcined at 500°C for 1 h and then imaged (b).

In comparison, upon calcination at 400 °C, the neighboring intra-sheets silanol groups (Si-OH) condensed, converting into Q^4 species decreasing the Q^3/Q^4 ratio from 2 to 0.6. Q^2 species were also detected, albeit with a small population, likely originating from the damages to the nanosheet during the exfoliation and processing steps.

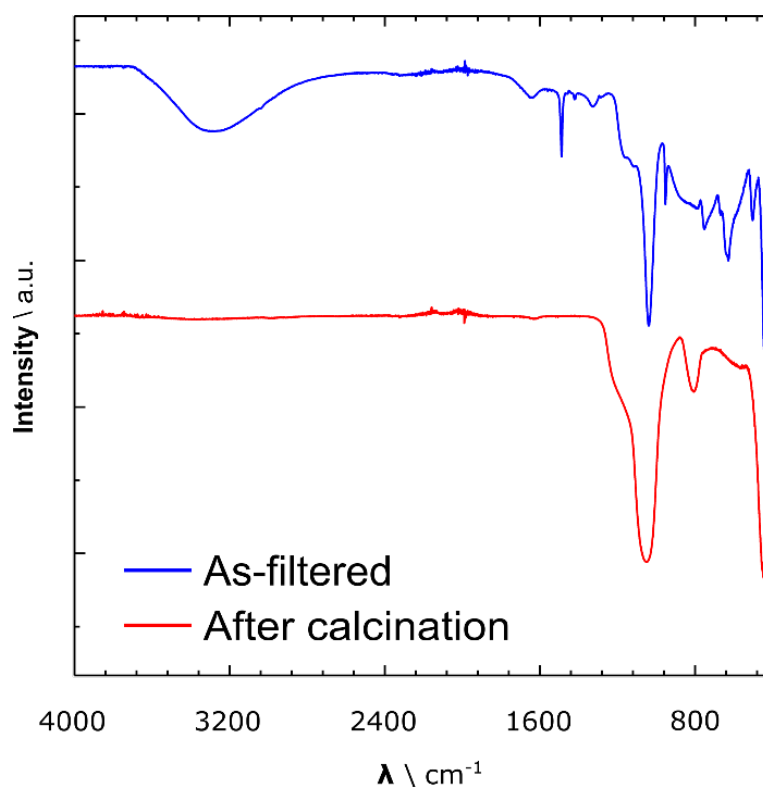


Figure 1.20. FTIR of the as-filtered and after calcination RUB-15 membranes.

When the heat treatment was carried out at 500 °C, a further and minor decrease in the Q^3/Q^4 was witnessed from 0.6 to 0.4, consistent with increased silanol condensation at a higher temperature. The three distinct Si bonding motifs (Q^4 , Q^3 , and Q^2) were also confirmed by higher sensitivity NMR measurement using cross-polarization (CP), in which the spin magnetization is transferred from ^1H to ^{29}Si (Figure 1.21).

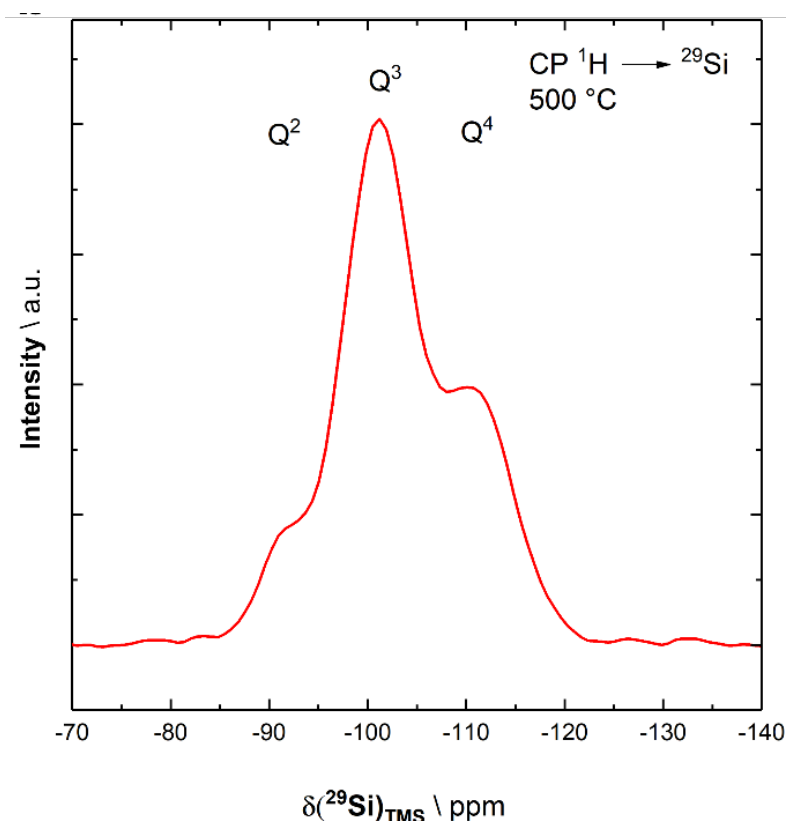


Figure 1.21. $^{29}\text{Si}\{^1\text{H}\}$ CP MAS solid-state NMR using a contact time of 10 ms with a pulse repetition time of 0.5 s indicating the presence of Q^4 , Q^3 and Q^2 species at calcination temperatures of 500°C .

To further probe the order in the calcined film, the film was transferred to a TEM grid by etching the support and lifting off the floating film by the grid. Sheet-like morphology could be observed (Figure 1.18d, left), and the corresponding SAED pattern agreed with the turbostratic arrangement of RUB-15 nanosheets with no particular preference of rotation of nanosheets in the plane of the film (Figure 1.18d, right). The intensities of the diffraction spots were weaker than those from the as-synthesized nanosheets in agreement with the broader in-plane XRD and NMR peaks indicating that the order in the calcined film was somewhat reduced, likely from framework distortion arising from the condensation of disorganized silanol groups in the turbostratic layers.

A survey of the morphology of the calcined film in the scanning electron microscope (SEM) revealed occasional cracks or peeling off of the film from the substrate (Figure 1.22).

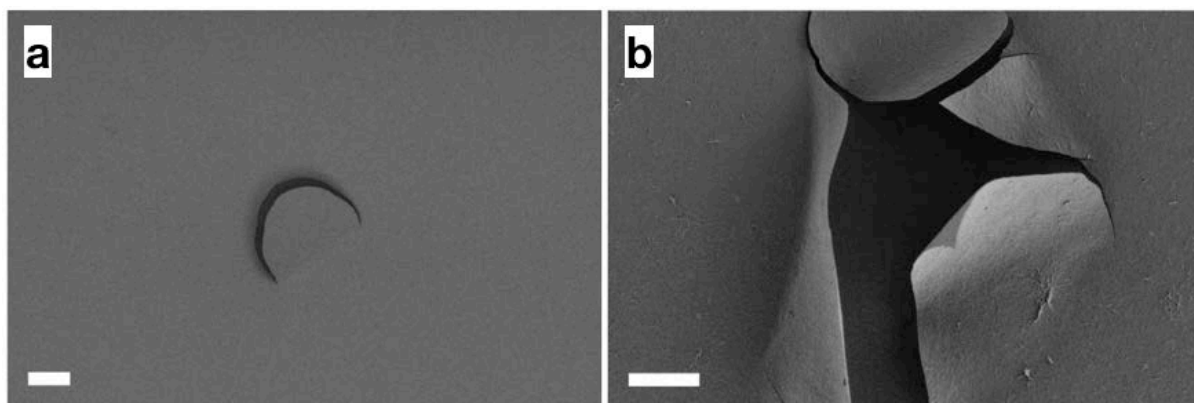


Figure 1.22. SEM images of calcined membranes showing the occasional cracks in the calcined film due to the non-uniformity of the commercial AAO support. The scale bars correspond to 10 μm .

Typically, we could observe 3-4 such incidences in a mm^2 area (Figure 1.23). We attribute this to the non-uniformity of the commercial aluminum oxide support, which had patches with higher porosity. During filtration, these patches developed a thicker coating, and consequently, the thicker area developed stress-induced cracks during the calcination step.

To avoid non-selective transport from cracks, we developed a curing step involving refiltration of the nanosheets coating on top of the calcined film. Since the flow of the solvent was predominantly through the cracks, the refiltration step plugged the defects within the nanosheets (Figure 1.24).

Analysis of the gas transport across the cured calcined film revealed that the intersheet gaps were indeed diminished upon calcination, and the H_2/CO_2 ideal selectivity increased well above 25, an order of magnitude higher than that compared to the as-filtered film, reaching up to 100 for several membranes (Figure 1.18e-g).

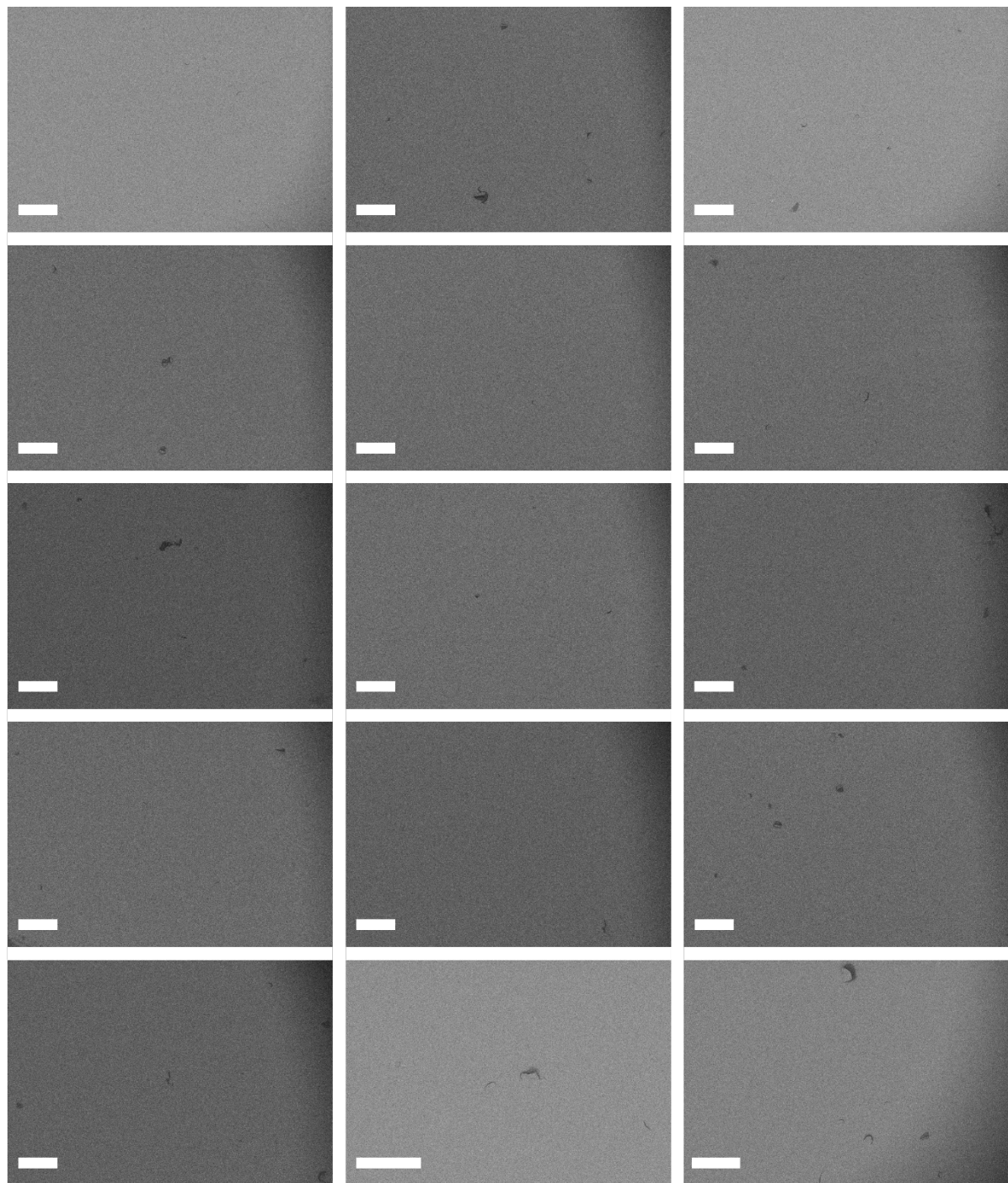


Figure 1.23. SEM images of calcined films showing the occasional cracks. The scale bars correspond to 200 μm .

Upon calcination, the $E_{act-app}$ for the transport of H_2 increased from 20 to 26.7 kJ/mole when the H_2/CO_2 ideal selectivity increased to 29.7 (Table 1.5). The $E_{act-app}$ progressively increased to 38 kJ/mole, close to that predicted by the NEB calculations (33 ± 2 kJ/mole) for transport across the 6-MR, when there were less defects in the calcined membrane (Figure 1.18g). This confirmed that the transport in these membranes was dominated by the 6-MR path. As expected, a further decrease

in the number of defects, which led to an increase in the H_2/CO_2 ideal selectivity (to 100) accompanied by a decrease in permeance (Figure 1.25), did not lead to an increase in $E_{act-app}$.

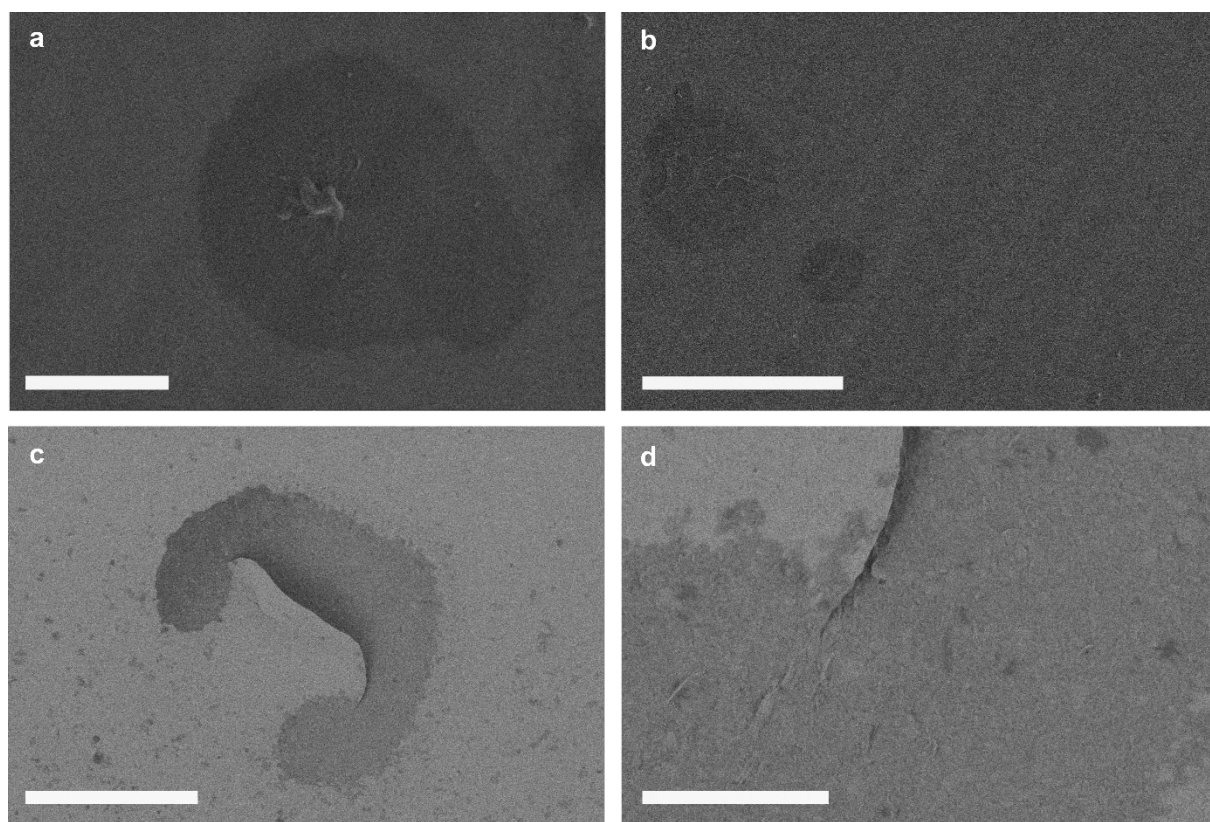


Figure 1.24. SEM images of the cured RUB-15 films. The scale bars correspond to a) 50 μm b) 300 μm c) 30 μm and d) 5 μm .

Following this strategy for the curing of defects, 7 separate membranes were prepared yielding H_2/CO_2 ideal selectivity in the range of 20-100 and H_2 permeance in the range of 41-424 GPU at 250-300 $^\circ\text{C}$ (Table 1.5).

Owing to the thermal stability of the zeolitic RUB-15 nanosheets and the activated transport, the H_2 permeance is expected to increase to 300 – 2400 GPU at 400 $^\circ\text{C}$ (Table 1.5). Overall, the H_2/CO_2 separation performance reported from the RUB-15 membranes compares favorably with those from the state-of-the-art zeolite membranes reported in the literature (Figure 1.25). This, combined with the fact that the RUB-15 membranes were made by facile filtration of RUB-15 nanosheets avoiding the conventional hydrothermal film treatment, makes these membranes highly attractive for the pre-combustion carbon capture where a H_2 permeance over 300 GPU and H_2/CO_2 ideal selectivity over 20 has been predicted to improve the energy-efficiency of the capture compared to that using the conventional absorption process.⁷⁸

Table 1.5. H₂/CO₂ separation data as a function of temperature, corresponding $E_{act-app}$ and the projected H₂ permeance at 400 °C from 7 separate cured RUB-15 membranes by refiltering the RUB-15 nanosheets on top of as-calcined RUB-15 films.

Membrane #	Temperature [°C]	H ₂ Permeance [GPU]	H ₂ /CO ₂ selectivity	$E_{act-app}$ [kJ/mole]	H ₂ permeance projected at 400 °C [GPU]
Membrane 1	250	211	29.7	26.7	830
Membrane 2	300	424	27.5	29.2	1895
Membrane 3	250	184	21.7	30	857
Membrane 4	300	147	22.5	31.7	747
Membrane 5	300	334	32.1	38.2	2369
Membrane 6	200	67	105.6	37.1	449
Membrane 7	200	41	103.8	38.5	295

Note: the project permeance at 400 °C was calculated by using the activation energy data (column 5) and measured permeance (column 3) at a given temperature (column 2).

Alternatively, we could also cure the defects by dip coating a thin layer of sol-gel derived silica solution (1 TEOS : 3.8 C₂H₅OH : 6.4 H₂O : 0.085 HNO₃; diluted by 19 fold; details in methods)¹⁶³ on top of the calcined RUB-15 film and curing the film at 500°C for 1 h. No significant change in film thickness was observed, and one could observe nanosheets coating beneath the silica layer (Figure 1.26). This strategy also led to an attractive sieving performance with H₂/CO₂ ideal selectivity in the range of 50-150 and H₂ permeance in the range of 100-1000 GPU at 250 °C from 8 separate membranes (Table 1.6).

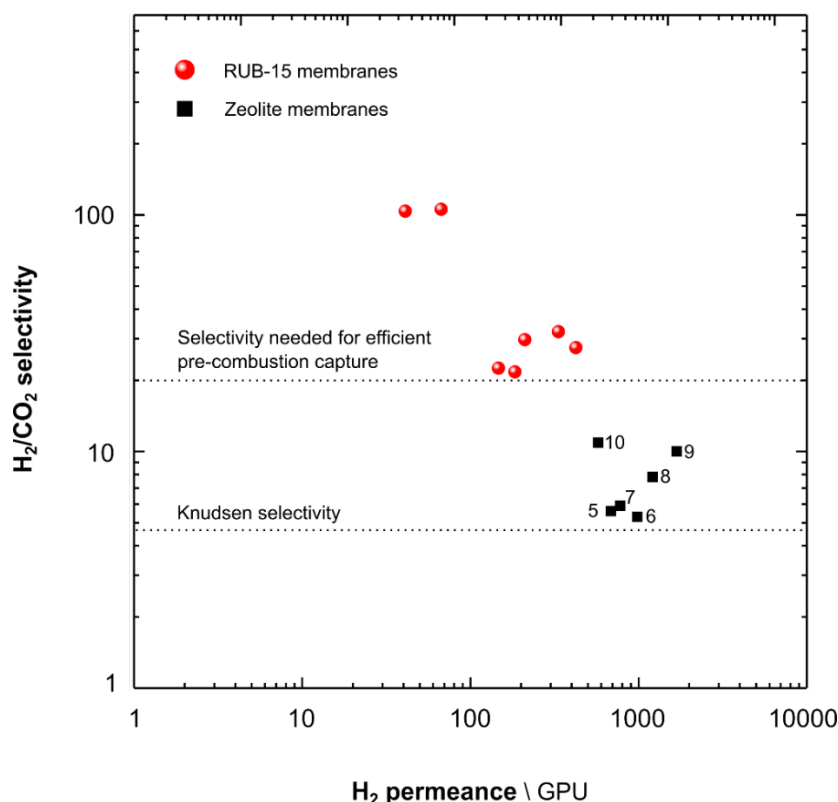


Figure 1.25. Comparison of the H_2/CO_2 separation performance from the RUB-15 nanosheet membranes compared with that from the state-of-the-art zeolite membranes at temperatures higher than 200 °C. Data from only those RUB-15 membranes that were prepared by refiltering RUB-15 nanosheets to heal the defects in the calcined films are included (i.e. RUB-15 films cured by silica coating are excluded). Hybrid zeolite membranes prepared by modifying zeolite films by organosilica were excluded since they do not present a single zeolite phase.^{164–169}

The membranes also performed well when fed with 50:50 volumetric H_2/CO_2 mixture thanks to the size-sieving transport (Figure 1.27).

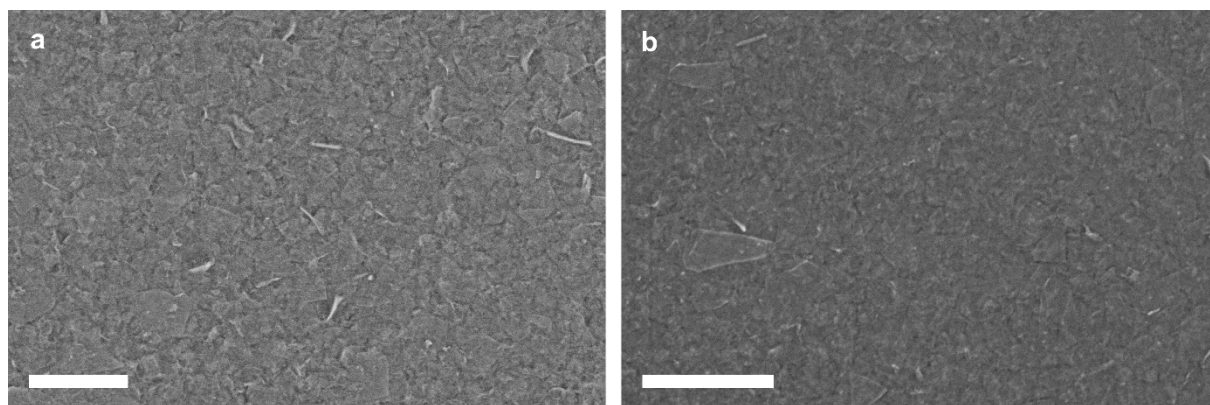


Figure 1.26. Top-view SEM images of the nanosheets film a) after filtration of nanosheets on a porous support and calcination, and b) after coating the film in (a) with the diluted silica solution. The scale bars correspond to 1 μm .

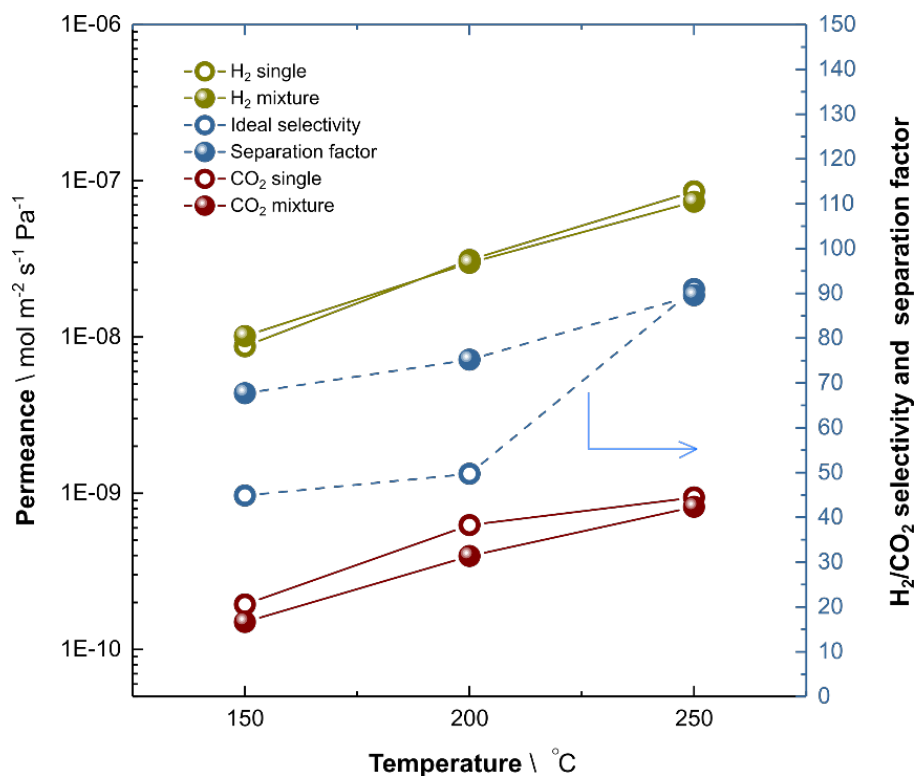


Figure 1.27. Single-component and mixed-gas (50:50 volume) permeation data from membrane 10 (Table 1.6).

In comparison to the single-component test, the H₂ permeance did not change while the H₂/CO₂ separation factor was slightly higher than the corresponding ideal selectivity. The membrane performance was stable during the 100 h continuous testing with an equimolar H₂/CO₂ mixture feed in the presence of 4% water vapor at 200 °C (Figure 1.18h).

Table 1.6. H₂/CO₂ separation performance of the 8 separate cured RUB-15 membranes by dip coating a thin silica layer on top of as-calcined RUB-15 films.

Membrane #	Temperature [°C]	H ₂ Permeance [GPU]	H ₂ /CO ₂ selectivity
Membrane 8	250	427	62.1
Membrane 9	250	713	49.4
Membrane 10	250	219	89.6
Membrane 11	250	848	154.1
Membrane 12	250	1182	47.4
Membrane 13	250	108	48.4
Membrane 14	250	184	21.7
Membrane 15	250	211	29.7

4. Conclusions

Overall, we demonstrate that the 6-MRs of sodalite precursor are indeed promising for the sieving of H₂ from CO₂. Chemically and thermally robust RUB-15 films are likely to find application in precombustion carbon capture, as the selective layer in the catalytic membrane reactors for the water–gas shift reaction, as well as the protective overlayer for Pd membranes. The film formation, calcination, and curing approach discussed here can be applied to fabricate high-quality zeolite films from a number of zeolite frameworks, for example, MWW, MFI, NSI, and so on, in which the precursors can be synthesized in the lamellar morphology. Scalable syntheses of such films without the complex hydrothermal treatment will improve the reproducibility of polycrystalline zeolite membranes and will bring them a step closer to large-scale deployment for gas and vapor separation.

Appendix I

Note 1. Mechanical stability of RUB-15 nanosheet

We studied the stability of RUB-15 using the DFT framework by considering its mechanical properties. To compute the elastic constants, we first relaxed the nuclei positions to a high degree of accuracy, using a 1 4 4 Monkhorst-Pack k-point grid, keeping the lattice parameters fixed in their experimental values. Deformations were applied, the new energy of the system was computed after the relaxation of the nuclei, and the elastic constants were then computed from the resulting energy-strain curves. For a two-dimensional (2D) material in the xy plane, the strain energy per unit area can be expressed as a function of the components of the elastic modulus tensor¹⁷⁰:

$$U(\epsilon) = \frac{1}{2}C_{11} \epsilon_{xx}^2 + \frac{1}{2}C_{22} \epsilon_{yy}^2 + C_{12} \epsilon_{xx}\epsilon_{yy} + 2 C_{66} \epsilon_{xy}^2 \quad (S1)$$

using Voigt notation (1=xx, 2=yy, 6=) for the components of the tensor. ϵ is the strain. By exploring different degrees of strain in the x -direction, C_{11} can be obtained. Analogously, C_{22} can be obtained by repeating the procedure for different strain values in the y -direction only. C_{12} can then be computed when applying strains in the x and y directions at the same time, while for computing C_{66} it is necessary to apply a strain in the angle, leaving the lattice parameters constant. The following values for the strain ϵ were considered to determine C_{11} , C_{12} and C_{22} : -0.05, -0.03, -0.01, -0.005, -0.002, 0, 0.002, 0.005, 0.01, 0.03 and 0.05. C_{66} was determined by applying strains

values of: 0, 0.001, 0.003, 0.005, 0.01, 0.03 and 0.05. For each strain explored, the energy per unit area, U , was plotted as a function of the strain, and the curve was fitted by a quadratic function. The parameters of these functions allow obtaining the elastic constants using equation S1. The results are shown in Table 1.1. For a 2D material to be mechanically stable, two conditions need to be fulfilled: $C_{66} > 0$ and $C_{11}C_{22} - C_{12}^2 > 0$. Both of them are valid for the 2D RUB-15, so we can conclude that the material is mechanically stable.

Note 2. Nudged elastic band (NEB) calculations for activation energy

The activation energy required for a gas molecule to go through the RUB-15 surface was computed by means of NEB, using the `neb.x` module of the Quantum Espresso 6.1. The Broyden scheme was used to minimize the energy of the path, and the two endpoint configurations were kept frozen after an initial relaxation prior to the NEB calculation. The auto climbing image scheme was considered. The calculation was considered to be converged when the norm of the force orthogonal to the path was less than 0.05 eV/Å for CO₂ and less than 0.02 eV/Å for H₂ for all the configurations. The calculations were performed following the protocol detailed below: (1) the adsorption sites were computed by adding an H₂/CO₂ molecule respectively and relaxing the positions of all nuclei to achieve minimum energy, (2) two NEB calculations were performed, one covering the path between the gas phase and the adsorption site (negative reaction coordinate values in manuscript Figure 1d) and another covering the path between the two adsorption sites at both ends of the RUB-15 surface (positive reaction coordinate values in manuscript Figure 1d. This part of the path features the passage of the gas molecules across the pore).

Finally, the influence of the chosen functional in the activation energy values was investigated by means of hybrid calculations using the PBE0 hybrid functional. The values of the activation energies were found to be overestimated by the PBE functional by 3 and 12% for CO₂ and H₂, respectively, thus revealing that the method of choice yields reasonable results.

Note 3. Comparison of the crystallinity of layered RUB-15 after 1-4 weeks of synthesis

Although the crystallinity of the one-week synthesis appears to be low compared to longer synthesis times, the narrow full width half maximum (FWHM) indicates a good stacking of the nanosheets along the [100] direction (Figure 1.5). Larger differences in the degree of crystallinity can be appreciated by analyzing the FWHM of the 022 plane for which the one-week sample shows a larger value of about 1/3 higher compared for example, to the two-weeks synthesis time (Figure 1.6).

Chapter 3. Gas-sieving zeolitic membranes on scalable polymeric support obtained with mild calcination temperatures and *in-situ* acidic detemplation

To be submitted. Mostapha Dakhchoune, Luis Francisco Villalobos, Pascal Schouwink, Claudia Esther Avalos, and Kumar Varoon Agrawal.*

Abstract

Abstract

The scalable fabrication of zeolite membranes is limited by the need of expensive inorganic supports and complex post-synthesis processing steps such as the detemplation and activation of the zeolite crystals. Up to 90% of the zeolite membrane cost is represented by the inorganic support, resulting in one of the major hurdles to their commercialization. Replacing the inorganic support with a polymeric one would drastically cut down the membrane cost. However, the high temperatures required for the detemplation of zeolites, and in some cases for the envisioned application, are above the thermal stability of most polymers. Herein, the scalable synthesis of polymer-derived porous support together with two mild zeolitic detemplation processes for the synthesis of gas-sieving RUB-15 membranes are reported. Non-solvent induced phase separation of PBI-AM Fumion[®] polymer on a cheap stainless steel mesh resulted in a porous (20 nm) and smooth surface ideal for depositing zeolitic nanosheets. RUB-15 detemplation temperature was reduced to 330 °C from 500 °C with successful removal of the occluded organic molecules and silanol condensation between the nanosheets. Alternatively to the thermal detemplation method, a room-temperature, liquid extraction-based process using diluted solutions of CH₃COOH in ethanol was developed. The extraction-based detemplation is highly scalable because it drastically cuts down the membrane's processing time and mitigates the creation of defects associated with the calcination step. The effectiveness of the mild calcination process together with the PBI-AM support yielded molecular sieving membranes capable of separating H₂/CO₂ with selectivities in the range of 20-35 and permeances up to 400 GPU under testing temperatures in the range 25-250 °C. Permeation results on the membranes detemplated with *in-situ* acid treatment displayed similar results.

1. Introduction

Zeolites are crystalline, microporous aluminosilicates with precise pore arrays in the range of gas molecules, which possess high chemical and thermal stability, making them ideal candidates for membrane-based gas separation. However, despite decades of excellent lab-scale demonstrations of high-performance membranes, their implementation on larger scales remains a longstanding challenge.

A key limitation is represented by the prohibitive cost of the inorganic supports (ceramic, metal-based, etc.), which often accounts for up to 90% of the total cost of the membrane.^{27,83,171,172} Moreover, the large-scale fabrication of these inorganic supports poses serious engineering and technical challenges.

Replacement with alternative, cheap materials would put zeolite membranes a step forward towards commercialization in gas separation applications. In this regard, polymeric supports could remarkably cut down the overall membrane cost. The synthesis of zeolite membranes on polymeric supports was successfully demonstrated on polyethersulfone (PES) for LTA and Faujasite frameworks.^{120,121} However, PES thermal stability is compromised at high temperatures, and this makes PES suitable only for frameworks that do not require the use of organic structure-directing agents (OSDAs) in their synthesis sols. On the other hand, most of the frameworks of interest for gas separation are synthesized with OSDA requiring a harsh thermal treatment (> 673 K) in oxidative atmosphere to activate the zeolitic pores by decomposing the occluded organic molecules.¹¹⁴ Although new approaches have been developed to detemplate the zeolitic framework such as rapid heat treatment (RTP)¹¹⁸ and UV/ozone-based,^{116,117} their employment with low-thermally stable polymers would severely compromise their integrity.⁹¹ This screens out the majority of polymeric supports, leaving only a few thermally stable polymers, such as polybenzimidazole-based polymers, as potential candidates for the scale-up of zeolite membranes for gas separations.

Polybenzimidazole (PBI) is a heterocyclic thermoplastic polymer with intrinsic H_2/CO_2 selectivity and high mechanical, thermal and chemical stability. PBI displays a low flux due to its densely packed chains leading to a low fractional free volume (FFV). The low-flux can be overcome by preparing porous PBI *via* non-solvent phase inversion (NIPS), making it suitable to be used as a support at the expense of the H_2/CO_2 selectivity. However, after the NIPS process, PBI becomes

brittle and shrinks considerably upon drying (up to 40% observed for hollow fibers), making its processing on a large scale a serious hurdle.¹⁷³ The use of water as non-solvent in the NIPS process causes, upon drying, the collapsing (or densification) of the pores in the selective layer due to the capillary forces originated by the high surface tension of the water.^{174,175} A multiple-step solvent-exchange strategy has been successfully employed to mitigate this phenomenon by going from water (surface tension at 25 °C equal to 72.71 mJ m⁻²) to methanol (surface tension at 25 °C equal to 22.09 mJ m⁻²) to isopropanol (surface tension at 25 °C equal to 20.92 mJ m⁻²) and finally to hexane (surface tension at 25 °C equal to 17.98 mJ m⁻²), preventing the pores from collapsing.^{176,177} Although the porous structure was successfully preserved, the shrinkage of the PBI hollow fiber was still significant (~18%).¹⁷⁷ Moreover, PBI is hard to dissolve in organic solvents, and if no additives are added to the solution, it precipitates out within a short time.

Besides the support optimization, many zeolite-related hurdles are still there to overcome to bring zeolitic membranes to mature commercialization and implementation on a large scale. The major hurdles include overcoming the low reproducibility of the hydrothermal synthesis, controlling grain boundary defects, and removing the structure-directing agent (SDA) without damaging the membrane. Tsapatsis group has demonstrated partial independence from hydrothermal synthesis by synthesizing two-dimensional (2D) MFI nanosheets and using them as building blocks for the fabrication of ultrathin membranes by simple filtration onto a porous substrate. However, the unselective gas transport through the intersheet gaps was dominant compared to the transport across the ten-membered SiO₄ ring (10-MRs), and a secondary growth step was necessary to achieve a high separation of xylene isomers.^{35,178} Recently, our group further improved the nanosheet-based processing by completely avoiding the secondary growth process in the fabrication of gas-sieving zeolitic membranes using exfoliated 2D RUB-15 nanosheets as building blocks.⁹² High H₂/CO₂ performance through the 6-MRs was achieved by eliminating the non-selective intersheet gaps *via* silanol condensation of neighboring nanosheets. However, the adopted detemplation method based on a calcination process to remove the occluded organic molecules was still taking place at elevated temperature (500 °C), rendering the potential use of polymeric supports unfeasible [even temperature stable polymer such as PBI partially degrade at 500 °C]. Moreover, the difference between the thermal expansion coefficients of the zeolitic layer and the underlying anodized aluminum oxide support (AAO) leads to the formation of cracks in the zeolitic film during the high-temperature calcination step, which required a defect healing step to be selective.⁹²

The development of milder detemplation methods that are compatible with the use of temperature stable polymeric supports (e.g., polybenzimidazoles and polyimides)^{179,180} would represent a useful advance towards the commercialization of zeolite membranes. This could be achieved by calcining at lower temperatures for a longer period of time or by using acids to remove the SDAs. For example, solvent extraction in acidic media [a mild detemplation method that was initially conceived for mesoporous materials and adapted to microporous silicates by Lami et al. has been successfully used to detemplate zeolite beta by using solutions of concentrated nitric acid (up to 13 N).¹¹⁹ Davis and co-workers showed that harsher conditions and longer time treatments were required to remove OSDA partially from zeolitic pores that had comparable size to the OSDA. This means that the relationship between the sizes of the OSDA molecule and the zeolite pore plays a crucial role in the extraction and that small pore zeolites are less prone to benefit from this method.^{181,182}

Herein, we address two of the major hurdles limiting the scale-up of zeolite membranes by developing a temperature-stable hybrid polymeric-inorganic support and developing two mild detemplating routes compatible with such support. Briefly, we synthesized a PBI-based support using NIPS of PBI-AM Fumion® on a stainless steel mesh and developed a low temperature (330 °C) and an acid-based detemplation process for RUB-15 nanosheet-based membranes compatible with the employment of the PBI-AM/stainless steel mesh support. To the best of our knowledge, this represents the first report of PBI-AM as membrane support. PBI-AM powder is easily dissolved in many organic solvents, and the NIPS process on a commercial stainless steel mesh yielded a 200 µm-thick PBI-AM layer with a smooth surface and uniform pore size in the range of 20-30 nm with negligible transport resistance.

The organic molecules trapped between RUB-15 nanosheets were removed *via* a mild calcination procedure (330 °C) that allowed the use of PBI-AM supports. *In-situ* X-ray diffraction of the calcination process confirmed the complete removal of organic molecules. In addition to the mild calcination procedure, we developed another route that was calcination-free (room temperature processing) for the removal of the guest organic molecules. This drastically cut down the number of processing steps and time to the final membrane. Non-acid treated RUB-15 nanosheets were filtered on the PBI-AM support, and once the RUB-15 film was fully formed, a 3M ethanolic solution of acetic acid was filtered to extract the organic molecules and eliminate the gallery spacing between the nanosheets.

The effectiveness of the two mild detemplating processes and the PBI-AM/stainless steel support yielded molecular sieving membranes capable of separating H₂/CO₂ with selectivities in the range

of 20-35 and permeances up to 400 GPU under testing temperatures in the range of 25-250 °C. Permeation results on the membranes detemplated with *in-situ* acid treatment displayed similar results.

2. Methods

2.1. Materials

The materials employed to synthesis bulk layered RUB-15 were purchased from commercial suppliers: Tetramethylammonium hydroxide TMAOH (25% in water, Sigma Aldrich), tetraethylorthosilicate TEOS, (98% anhydrous, Acros), N-Methyl-2-pyrrolidone NMP, (99%, Sigma Aldrich), low-molecular-weight polystyrene (1360 g/mol, Eastman), ethanol (99.9%, Fisher chemicals), hexadecyltrimethylammonium bromide CTAB, (>98%, Sigma Aldrich), sulfuric acid, (95-97%, Merck), chlorobenzene (99.8%, Merck), toluene (99.8%). PBI-AM Fumion[®] powder was purchased from Fumatech. Stainless steel mesh (pore size 20 µm, Part number #325X2300TL0014) was purchased from TWP Inc.

2.2. Layered RUB-15 hydrothermal synthesis.

Layered RUB-15 was synthesized *via* hydrothermal synthesis by adopting a modified recipe reported elsewhere.^{107,109} Briefly, 112.5 g of TMAOH was mixed with 64.3 g of tetraethylorthosilicate and 128.8 g of deionized water by stirring for 24 h at 25 °C in a polypropylene beaker. The mixture was then transferred to a rotary evaporator at 40 °C and 100 mbar of pressure using 75 rpm, until the complete evaporation of the solvent was achieved. Wet crystals were dried in a tissue paper for a few hours and transferred to a Teflon-lined autoclave, and heated at 150 °C for 2 weeks. The obtained white powders were thoroughly washed with deionized water (DI) and dried in a convection oven at 70 °C.

2.3. CTAB-based swelling of RUB-15 layers.

Swelling of layered RUB-15 powder was carried out by stirring 3.4 g of hexadecyltrimethylammonium bromide (CTAB) in 200 mL of DI water until the solution turned transparent. 1 g of layered RUB-15 was then added, and the system was stirred for 24 h at room temperature. Next, the powder was collected, washed with abundant water, and dried at 70 °C.

2.4. RUB-15 exfoliation.

RUB-15 exfoliation was performed by the melt compounding technique (Xplore micro compounder 15) as reported by Tsapatsis and co-workers with small modifications.³⁵ In a typical experiment, 0.6 g of swollen RUB-15 was mixed with 15 g of low-molecular-weight polystyrene at 120 °C under a nitrogen environment. Next, the temperature was slowly decreased to 60 °C and then kept fixed for the whole experiment duration. The temperature of the extrusion was 90 °C.

2.5. Nanosheets extraction from polymeric matrix.

RUB-15 nanosheets embedded in the nanocomposite (polymeric matrix) were dissolved in toluene with a concentration of 1.23 w/w%. 50 mL in volume PTFE tubes were filled with 25 mL of chlorobenzene and gently added 25 mL from the nanocomposite solution in toluene. A centrifugation step of 4000 g-force and 3 h was performed (Beckman Coulter, Avanti J-26S XP), which settled down the cake of nanosheets while the supernatant, rich in polystyrene, was discarded. Fresh ethanol was added, and the centrifugation repeated once more to remove chlorobenzene traces. Note, for membranes prepared with acidic extraction, toluene was added rather than ethanol.

2.6. Sulfuric acid treatment of RUB-15 nanosheets

The cake resulting from the centrifugation step was dispersed in sulfuric acid solution in ethanol (0.2 M) and kept under stirring at 80 °C for 16 h. Following the acid treatment, a series of centrifugation steps (40000 g-force for 3 h) were performed until the solution pH was around 7. Nanosheets treated using this procedure will be referred to as acid-treated nanosheets.

2.7. PBI-AM support preparation

The dope solution was prepared by mechanically stirring an 8 w/w% solution of PBI-AM powder in NMP solvent. The solution was used as it is without further treatment. A water coagulation bath was heated at 60 °C, and a casting knife of 10 MIL (~ 250 µm) was used to cast the solution on the stainless steel mesh. Upon casting, the system was placed in the coagulation bath and left overnight. The supports were then washed with deionized water and let dry at room temperature. For the stabilization of the support structure, the PBI-AM was heated at 330 °C for 8 h. After the heat treatment, the supports were used without further treatment.

2.8. Assembly of nanosheets into a membrane with mild calcination temperature

200 μL of purified acid-treated RUB-15 nanosheets were added to 12 mL of fresh ethanol and sonicated for 25 minutes. The solution was then centrifuged at 5000 rpm for 10 min in a Falcon tube, and the top 10 mL were gently piped out and used for the membrane assembly. Vacuum filtration was tuned to achieve a flow rate of $\sim 2.8 \times 10^{-3}$ mL/s. After the completion of the filtration (usually 20 min), the RUB-15@PBI-AM membrane was dried at room temperature for a few hours and then calcined at 330 $^{\circ}\text{C}$ for 8 h. The occasional-defective membranes were healed by refiltering a fresh dilute suspension of purified nanosheets in ethanol (1 mL of a solution diluted 10-fold with respect to the solution used to prepare the membrane) to clog defects.

2.9. Assembly of nanosheets into a membrane with acidic extraction

RUB-15 nanosheets were purified from the polymeric matrix as mentioned previously, and toluene was added rather than ethanol since no acid treatment was performed before the membrane fabrication. A small aliquot (300 μL) of nanosheets dispersed in toluene was mixed with 12 mL of fresh toluene and sonicated for 25 minutes. The suspension was used as it is without centrifugation and filtered through the PBI-AM support.

Once the suspension in toluene was filtered, 10 mL of acetic acid in ethanol (3 M) was poured and filtered through without changing the vacuum conditions. Pure ethanol (20 mL) was used to wash away residues of the acetic acid. Finally, the membrane was removed and dried overnight at 70 $^{\circ}\text{C}$.

2.10. Gas permeation.

Mixed and single gas permeation tests were carried out using a homemade permeation setup (Figure 1.1). Argon was used as the sweep gas. Flow rates of the gases were controlled by mass flow controllers (MFCs). The permeate gas concentration was analyzed in real-time by a mass spectrometer (Hiden Analytical, HPR-20). Once the steady-state was reached, the permeate concentration data was recorded and averaged (typically 30-60 min for each gas measurement). The gas permeance J_i , the ideal selectivity α_{ij} , and the separation factor β_{ij} were calculated by the following Equations (1-3).

$$J_i = X_i / (A * \Delta P_i) \quad (1)$$

$$\alpha_{ij} = J_i / J_j \quad (2)$$

$$\beta_{ij} = (C_i / C_j)_{\text{permeate}} / (C_i / C_j)_{\text{feed}} \quad (3)$$

where X_i is the flow rate of component i , A is the membrane area, ΔP_i is the transmembrane pressure difference for component i , C_i and C_j are the concentrations of component i and j in the feed/permeate streams with i being the faster-permeating component.

2.11. Characterization

Powder XRD patterns were collected with a Bruker D8 Advance using $\text{CuK}\alpha$ radiation ($\lambda \text{ Cu K}\alpha = 1.5406 \text{ \AA}$). In-plane and diffraction measurements were conducted on a D8 Discover Plus TXS (Bruker). The measurements were taken in parallel beam mode. The incident angle was set to 2° , and the incident beam was equipped with a 1 mm-hole together with a c1 mm-collimator.

SEM images were collected using an FEI Teneo scanning electron microscope at an acceleration voltage of 1-2 kV. Samples were imaged without using any conductive coatings. Focused-ion beam was performed with a Zeiss XB 540.

3. Results and discussions

3.1. PBI-AM support fabrication and assembly of RUB-15 nanosheets

The commercially available PBI-AM copolymer offers many advantages compared to PBI for the fabrication of porous polymeric supports. PBI-AM is more processable than PBI as it easily dissolves in several NIPS compatible solvents such as dimethylacetamide (DMAc), N,N-dimethylformamide (DMF), N-Methyl-2-Pyrrolidone (NMP), and dimethyl sulfoxide (DMSO) without the need of additives. Moreover, upon drying, the porous structures of PBI-AM supports, formed using the NIPS process, retain their flexibility, and their pores do not collapse. On the contrary, conventional PBI is very difficult to dissolve, and traces of undissolved polymer can be a source of defects in the fabrication of nanocomposite membranes. Additionally, porous PBI structures prepared *via* the NIPS process tend to collapse upon drying and become very brittle.^{176,183,184}

We could dissolve PBI-AM in common organic solvents (NMP, DMAc, DMF, etc.) up to 10 w/w % by mechanical stirring at room temperature. PBI-AM supports were prepared via the NIPS process onto a low-cost woven stainless steel mesh (Figure 2.1a and Figure 2.3a). The woven stainless steel mesh employed in the process had an average pore opening of 20 μm , is mechanically robust, and can withstand high temperatures. The 20 μm openings were ideal to allow partial infiltration of the viscous polymeric solution (Figure 2.1a and Figure 2.3a, Figure 2.3g), effectively anchoring the porous PBI-AM to the stainless steel mesh. In this way, any macroscopic shrinkage and bending upon drying was avoided. On the contrary, free-standing films of PBI-AM, made by casting the PBI-AM solution on top of a glass plate, bent heavily upon drying and shrank $\sim 10\%$. The regular surface of the metal mesh support guaranteed a uniform thickness of the casted film. When a casting blade of 10 MIL ($\sim 250 \mu\text{m}$) and a PBI-AM 8 w/w% solution were employed, the average thickness of the porous polymer layer was 200 μm . The resulting structure yielded a smooth surface with $\sim 20 \text{ nm}$ pores and a cross-section with a macrovoid-free spongy layer from 2 to 50 μm on the top and large macrovoids below it (Figure 2.1b and Figure 2.3b-e). The as-prepared supports were calcined in air at 330 $^{\circ}\text{C}$ for 8 h to ensure their thermal arrangement and structure stabilization prior to the deposition of RUB-15 nanosheets.⁹¹ We note that the porous structure of the PBI-AM/metal mesh films was retained after such a calcination step.

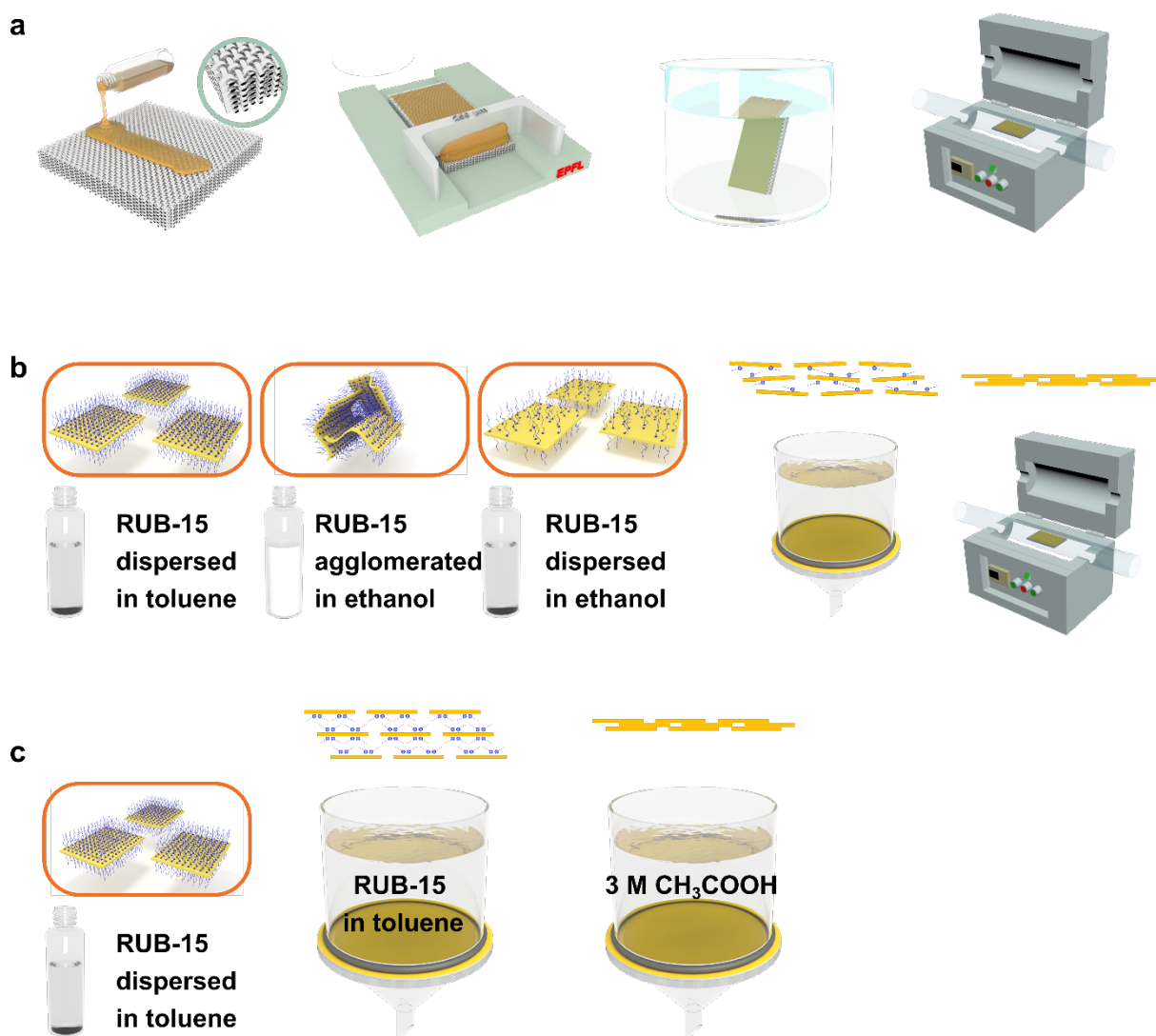


Figure 2.1. a) Illustration of the NIPS process of the PBI-AM polymer, including coating of the stainless steel mesh with 8% w/w solution in NMP, casting with 10 MIL blade, phase inversion in a water bath at 60 °C, and thermal treatment of the rearrangement and stabilization of the support at 330 °C. b) Solution processing of RUB-15 nanosheets with conventional *ex-situ* acid treatment in sulfuric acid, filtration onto PBI-AM support and new calcination procedure at 330 °C for 8 h. c) New solution processing of RUB-15 nanosheets without the need of thermal treatment for the removal of the occluded organic molecules.

RUB-15 nanosheets preparation was obtained following our previous report.⁹² Briefly, the layered morphology of RUB-15 was synthesized hydrothermally by a pseudo-solid-state transformation of hydrated silicate double-four-ring (D4R) at 150 °C.^{107,185} Tetramethylammonium hydroxide (TMAOH) SDA was ion-exchanged with cetyltrimethylammonium bromide (CTAB) to weaken the interlayer interactions between RUB-15 nanosheets, facilitating the polymer-based exfoliation with low-molecular-weight polystyrene (1360 g mol⁻¹) with the melt-compounding technique.¹⁵⁹ Extraction and purification of RUB-15 nanosheets from the polymeric matrix were carried out using density-gradient centrifugations.⁸⁸

The processing of RUB-15 nanosheets into H_2/CO_2 gas-sieving membranes using the scalable PBI-AM supports, and the mild calcination approach is illustrated in Figure 2.1b. Starting with a highly stable dispersion of RUB-15 nanosheets in toluene [the good interaction between the apolar solvent and the CTAB tails guarantees a stable dispersion] (Figure 2.1b), the nanosheets were transferred into ethanol resulting in a foggy dispersion due to the nanosheets agglomeration caused by the unfavorable interaction between CTAB and the polar ethanol (Figure 2.1b). Mild sulfuric acid treatment in ethanol (0.2 M) removed some of the CTAB molecules from the surface of the nanosheet, and the newly exposed charged groups allowed the dispersion of the acid-treated RUB-15 nanosheets in ethanol for a time scale of hours before resettling down. The hours-long stability was sufficient for the fabrication of membranes *via* filtration. A harsher acid treatment in a 4 M H_2SO_4 solution was needed to fully remove the CTAB molecules. Thermogravimetric analysis (TGA) on the mildly acid-treated nanosheets showed a weight loss percentage of 18.3%, while non-acid treated and harsh-treated (4 M H_2SO_4) nanosheets, the weight losses were 51.2 and 9.7%, respectively (Figure 2.2). This reveals that the milder acid treatment (H_2SO_4 0.2 M) partially removed the surfactant from the nanosheets, and a harsher treatment (H_2SO_4 4 M) was necessary to completely detemplate RUB-15 nanosheets. Even though it was possible to fabricate continuous RUB-15 films from completely detemplated nanosheet dispersions (H_2SO_4 4 M case), the resulting membranes were not selective. We hypothesized that the presence of CTAB during the filtration step is required to obtain a nanosheet packing adequate for membrane applications where intersheet gaps are minimized. The mildly acid-treated nanosheets were successfully used to fabricate thin selective films (~ 150 nm) on the PBI-AM support *via* vacuum-filtration (Figure 2.3f-h) followed by a mild calcination step to remove the remaining CTAB molecules. The novelty in this procedure was the development of a mild yet efficient calcination procedure (330°C instead of 500°C), which allowed the employment of PBI-AM support (details in section 3.2).

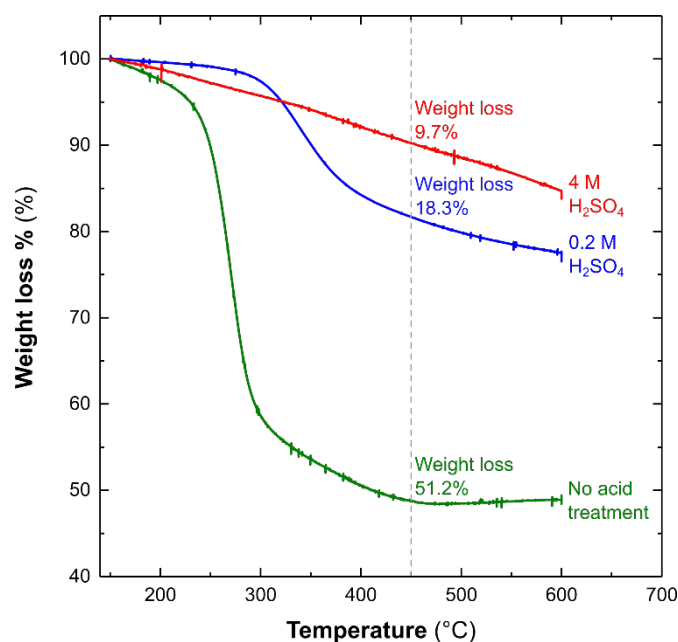


Figure 2.2. Thermogravimetric analysis of RUB-15 nanosheets as a function of the acid treatment concentration. Red, blue, and green curves are RUB-15 nanosheets treated in an ethanolic solution of H₂SO₄ 4 M, 0.2 M, and no acid-treated, respectively.

Alternatively to the thermal removal of the occluded organic molecules, we developed a facile extraction process to remove CTAB molecules from already formed RUB-15 films with dilute solutions of acetic acid, which allowed a drastic cut-down of the overall membranes fabrication process. The OSDA extraction method using an acid treatment was previously reported and proven to be very effective on MFI (silicalite-1) and beta zeolite crystals when tetraethylammonium cation and the linear hexamethylenediamine OSDAs were used for the synthesis of beta and silicalite-1, respectively.¹⁸² However, only partial removal was achieved when bis-piperidinium and tetraalkylammonium templates were used for beta and silicalite-1, respectively, underlying the strong relation between pore size and OSDA size.^{181,182} Contrarily to silicalite-1, where the OSDA is located within the 10-MR pore of the zeolite along the *b*-axis, RUB-15 contains the OSDA-exchanged surfactant on the outer surface of the nanosheets, rendering its extraction process doable under mild conditions. Figure 2.1c shows how directly from the nanosheets dispersed in toluene we could fabricate membranes on the PBI-AM support. Once the membrane was formed, a 3 M ethanolic solution of acetic acid was filtered through ensuring the removal of the CTAB. XRD studies confirmed the removal of the CTAB evidenced by a decrease in the *d* spacing to 8 Å, which is equivalent to the thickness of the nanosheet and expected when no CTAB is present (details in section 3.2). We note that the PBI-AM support was chemically stable under the toluene and environment 3 M ethanolic solution of acetic acid used for these steps.

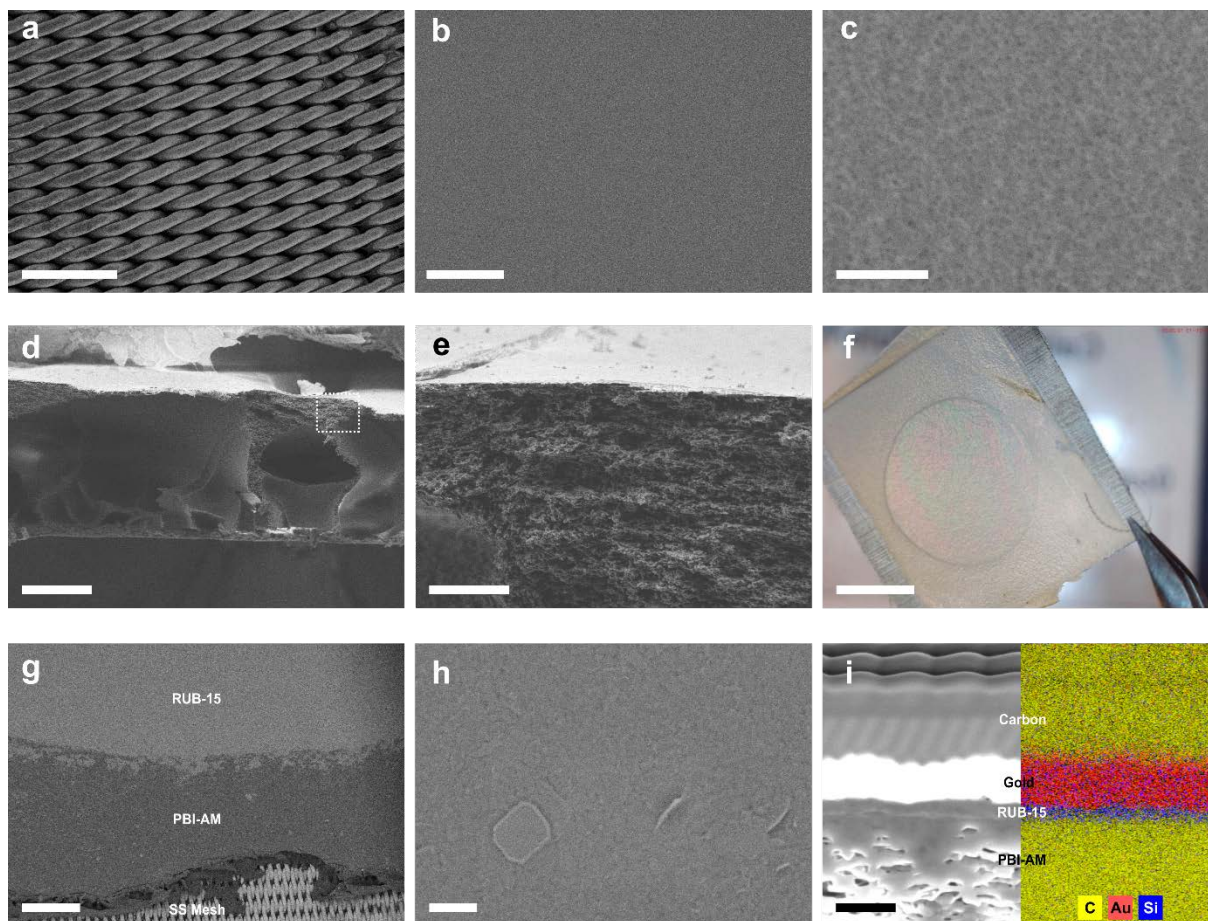


Figure 2.3. a) SEM image of stainless steel with an average pore opening of 2 μm . Low- b) and high-magnification. c) SEM images of the PBI-AM support showing the surface uniformity and the narrow pore size with an average size of 20 nm. d) SEM image showing the film cross-section with macro voids and $\sim 200 \mu\text{m}$ in thickness. e) High-magnification SEM image of the dotted square in (d). f) Photograph of the PBI-AM support with RUB-15 nanosheets coated on top in the colorful central disc. g) SEM image of the boundaries between zeolitic film, PBI-AM support, and stainless steel mesh. h) High-magnification SEM image showing the good packing of the nanosheets. i) Focused Ion Beam-SEM image of the cross-section of RUB-15 film ($\sim 150 \text{ nm}$ in thickness) on PBI-AM support. Carbon and gold layers were used to protect RUB-15 film from beam damage. Scale bars are: 200 μm in (a) and (b), 400 nm in (c) and (i), 100 μm in (d), 50 μm in (e), 0.5 cm in (f), 1 mm in (g), and 500 nm in (h).

3.2. *In-situ* XRD of mild thermal detemplation

In our previous report, RUB-15 membranes were calcined in air at 500 $^{\circ}\text{C}$ for 1 h, ensuring the complete removal of CTAB surfactant and the silanol condensation between nanosheets, which blocked the gas transport through non-selective pathways.⁹² However, such temperature does not allow the employment of polymeric supports such as PBI-AM (decomposition temperature > 400 $^{\circ}\text{C}$). Detemplation reaction time and temperature are two major variables that affect the SDA removal when using thermal treatments. For example, a longer detemplation process at mild temperatures (e.g., 300 $^{\circ}\text{C}$ for 8 h) could open the majority of MFI pores occluded by the SDA,

and a similar result was achieved with a shorter exposure at a higher temperature (e.g., 450 °C for 4 h).^{61,91}

To explore the time-temperature dependence of the detemplation process of RUB-15 films and develop a mild calcination procedure compatible with PBI-AM, we performed *in-situ* XRD studies on RUB-15 films on PBI-AM (Figure 2.4a). XRD of the *in-situ* heat treatment demonstrated that the complete removal of CTAB and the silanol condensation were taking place at lower temperatures when the sample was kept for 8 h at 330 °C (Figure 2.4a). The *d* spacing remained constant around 11 Å (Note 1 Appendix I) up to 150 °C. In the range of temperatures of ~150-240 °C, the *d* spacing between RUB-15 nanosheets layers increased by 0.5 Å, due to the higher kinetic activity of the trapped organic molecules between the layers (Figure 2.4a-b). From ~270 °C to ~310 °C, a sharp decrease of the *d* spacing took place due to the fast degradation of the surfactant into combustion products (Figure 2.4a-b). The constant temperature at 330 °C for 8 h ensured the complete removal of the surfactant together with the silanol condensation between nanosheets (Figure 2.4a).

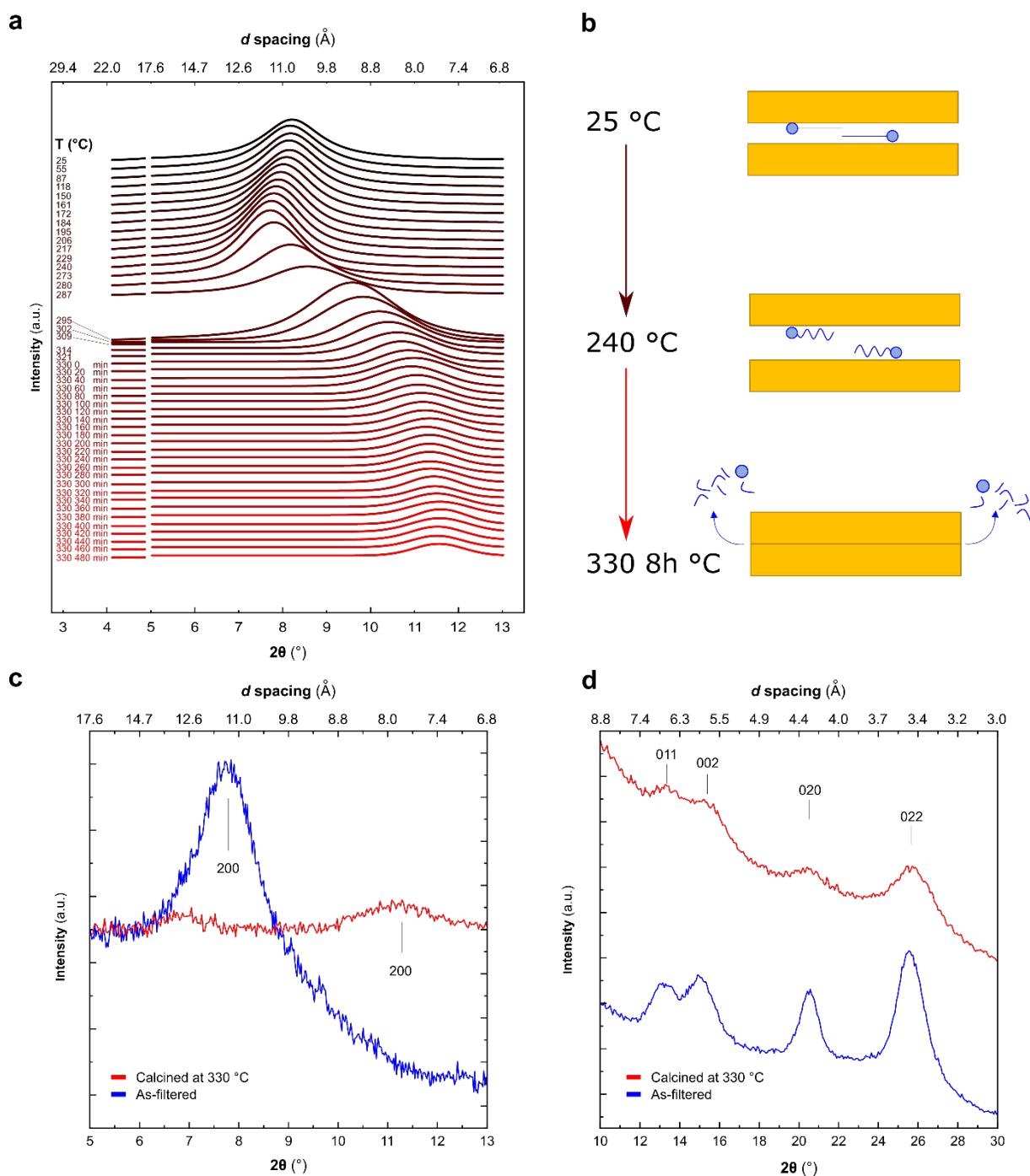


Figure 2.4. a) *In-situ* out-of-plane XRD (Cu K α , $\lambda = 1.5406 \text{ \AA}$) on RUB-15@ PBI-AM film from 25 °C to 330 °C in air atmosphere. b) Illustration of the nanosheets d spacing variation during the *in-situ* XRD performed in (a). c) Out-of-plane XRD (Cu K α , $\lambda = 1.5406 \text{ \AA}$) of RUB-15@PBI-AM film in the as-filtered films and calcined with new calcination process d) In-plane XRD (Cu K α , $\lambda = 1.5406 \text{ \AA}$) of RUB-15@PBI-AM film for as-filtered and calcined at 330 °C for 8 h.

Careful (Note 1 Appendix I) *ex-situ* out-of-plane investigation of the as-filtered RUB-15 film and after the 330 °C for 8 h calcination showed good agreement with our previous report. The interlayer d spacing (200 peak) shifted from 11.4 to $\sim 7.6 \text{ \AA}$ after the mild calcination temperature indicating that all the CTAB was removed and only condensed RUB-15 nanosheets remained (Figure 2.4c).

RUB-15 nanosheet thickness is ~ 8 Å, and after the silanol condensation, the removal of a water molecule decreases the interlayer distance to the observed ~ 7.6 Å.

To probe the crystallinity of the nanosheets upon calcination, in-plane XRD was performed on RUB-15 films before and after the 330 °C heat treatment (Figure 2.4d). Four distinct peaks were clearly visible in the as-filtered films relative to the 011, 002, 020, and 022 planes of RUB-15, which are in agreement with the nanosheets orientation along the *a*-axis. Upon calcination for 8 h at 330 °C, the same plane's reflections were distinguishable, indicating the preservation of the in-plane nanosheet order.

3.3. Gas separation RUB-15@PBI-AM calcined at 330 °C

Gas transport analysis from RUB-15 membranes supported on PBI-AM (RUB-15@PBI-AM) and detemplated with the new calcination process confirmed that the developed process contributed to the elimination of the intersheet gaps. RUB-15@PBI-AM membranes after the mild calcination step yielded H₂/CO₂ selectivities in the range of 20-35 and permeances up to 400 GPU under testing temperatures in the range of 25-250 °C (Figure 2.5a-d).

Single-gas permeation measurement of He (kinetic diameter 0.26 nm), H₂ (0.29 nm), CO₂ (0.33 nm), N₂ (0.36 nm), and CH₄ (0.38 nm) showed a sharp cut-off in the permeance between small (He and H₂) and large (CO₂, N₂, and CH₄) molecules, indicating that the transport was based on a molecular sieve mechanism across the 6-MRs of RUB-15 nanosheets (Figure 2.5a).

Nudged elastic band (NEB) calculations on RUB-15 nanosheets between the gas phase and the adsorbed state located on the other end of the pore surface estimate the apparent activation (E_{AA}) energy barrier for H₂ molecules equals to 33 ± 2 kJ mol⁻¹.⁹² RUB-15@PBI-AM membranes followed a systematic trend in which higher selectivities were obtained at apparent activation energies close to what NEB calculations estimate (Figure 2.5c). Finally, the newly developed RUB-15@PBI-AM membranes enriched the literature of pure zeolitic phase membranes capable of providing an efficient pre-combustion capture process if compared to conventional absorption-based processes (Figure 2.5d).¹⁸⁶

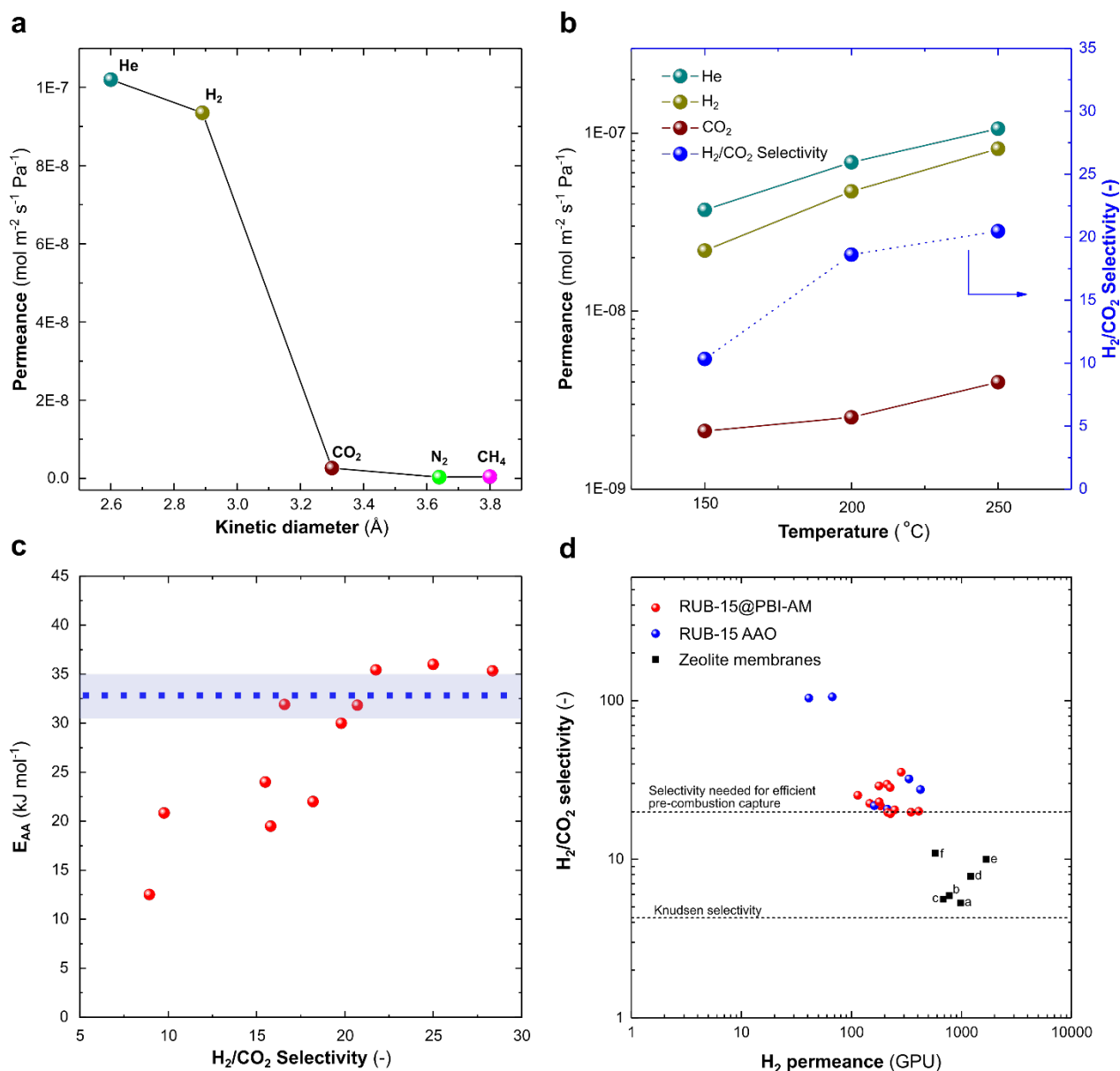


Figure 2.5. a) Single-gas permeation measurements He, H_2 , CO_2 , N_2 , and CH_4 as a function of their kinetic diameter. b) Single-gas permeation measurements from the RUB-15@PBI-AM membranes as a function of temperature. c) E_{AA} for H_2 as a function of the H_2/CO_2 ideal selectivity. The horizontal blue band represents E_{AA} from our previous NEB calculations.⁹² d) Comparison of the H_2/CO_2 separation performance from the RUB-15 nanosheet membranes compared with that from the state-of-the-art zeolite membranes at temperatures higher than 200 $^{\circ}\text{C}$. Hybrid zeolite membranes prepared by modifying zeolite films by organosilica were excluded since they do not present a single zeolite phase. a,¹⁸⁷ b,¹⁸⁸ c,¹⁶⁶ d,¹⁶⁷ e,¹⁶⁸ f.¹⁸⁹

3.4. In-situ detemplation of RUB-15@PBI-AM membranes

Alternatively to the thermal-based detemplation method, the use of a room-temperature liquid extraction-based process was developed. This approach allowed the facile removal of the CTAB molecules that are trapped within the interlayer spacings by simply filtering 10 mL of a 3 M solution of acetic acid in ethanol. First, the nanosheets dispersed in toluene were vacuum-filtered

to fabricate thin films on the PBI-AM support, and subsequently (before the membrane dries), 10 mL of the acidic solution were added on top of the wet film and filtered.

Out-of-plane XRD on the films obtained by the filtration of the nanosheets dispersed in toluene (Figure 2.6, green line) showed a sharper 200 peak compared to the conventional RUB-15 nanosheets dispersed in ethanol and acid-treated with a 0.2 M solution of H_2SO_4 . The full-width half-maximum (FWHM) of the films prepared from toluene (without CTAB removal) was 0.30° (Figure 2.6, green line), while the conventionally detemplated films (partial removal of the CTAB) displayed a FWHM of 1.31° (Figure 2.6, magenta line). We speculate that the highly concentrated CTAB molecules act as pillars for the nanosheets, increasing their order (Figure 2.6, top inset). Analogously, when the concentration of CTAB was scarce, a higher deviation from horizontal alignment occurs, resulting in a broader peak (Figure 2.6, top inset). Moreover, a larger d spacing of 13.4 Å is observed for the nanosheets in toluene, compared to 11.4 Å for acid-treated nanosheets (Figure 2.6), which is due to the different orientation of the CTAB molecules.

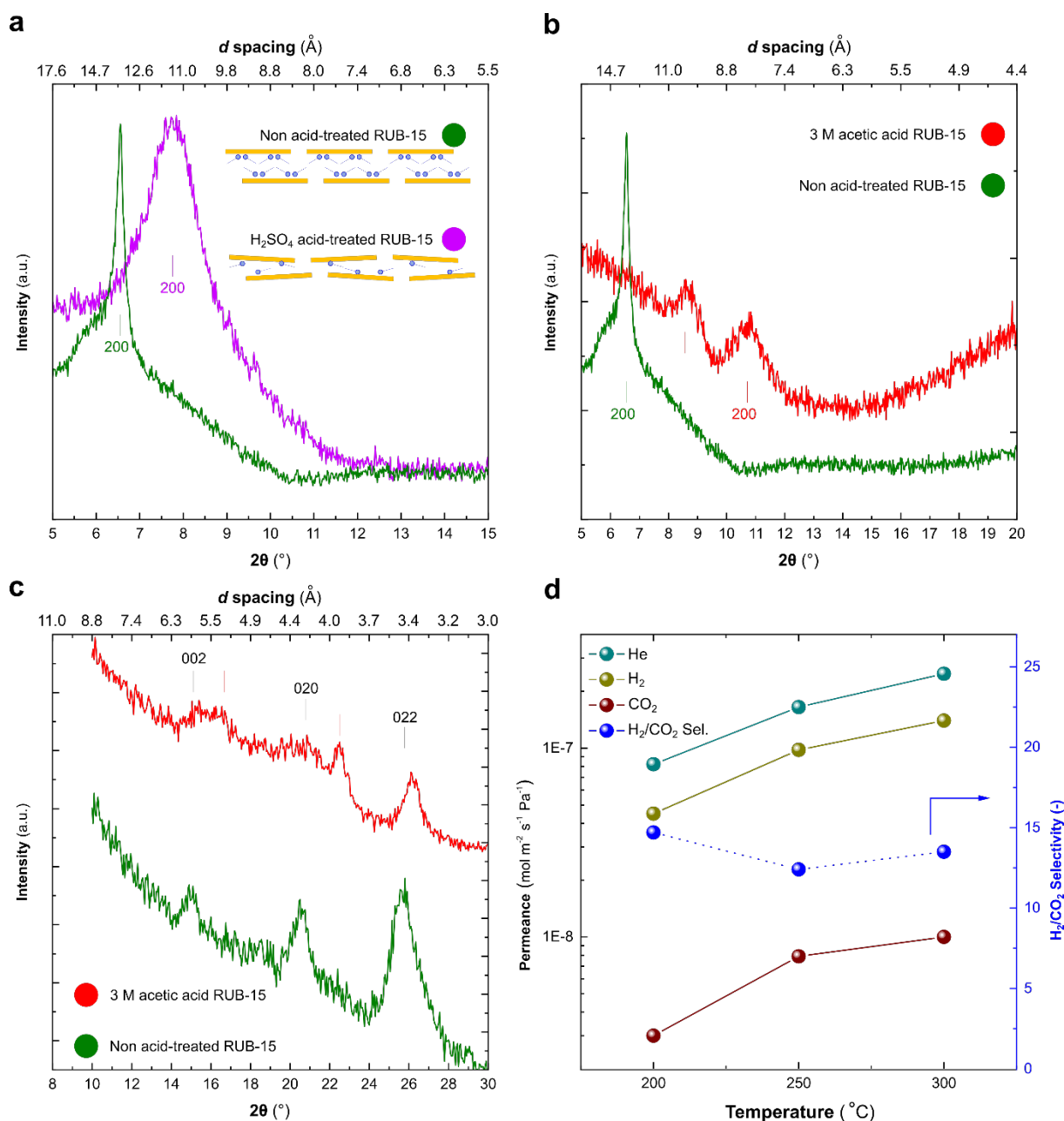


Figure 2.6. a) Out-of-plane XRD (Cu K α , $\lambda = 1.5406 \text{ \AA}$) of as-filtered RUB-15 films. Comparison of the d spacing between membranes fabricated with acid-treated nanosheets with conventional method based on 0.2 M of sulfuric acid (magenta) and membranes fabricated with nanosheets dispersed in toluene and that did not undergo acid treatment (green). Cartoons are an illustration of possible nanosheets configuration. b) Out-of-plane XRD (Cu K α , $\lambda = 1.5406 \text{ \AA}$) of as-filtered RUB-15 film without any acid treatment (green) and film obtained by re-filtering a 3 M solution of acetic acid in ethanol (red). c) In-plane XRD (Cu K α , $\lambda = 1.5406 \text{ \AA}$) of RUB-15 films before (green) and after (red) the refiltration step with 3 M acetic acid solution in ethanol. d) Preliminary gas permeation data from a membrane detemplated with extraction method with an acetic acid solution, Permeances of He, H $_2$, and CO $_2$ together with ideal H $_2$ /CO $_2$ selectivity are reported.

After filtering a diluted solution (3 M) of acetic acid in ethanol, the d spacing shifted from 13.4 \AA to 8 \AA as confirmed by the shifting of the 200 peak reflection in Figure 2.6b. Surprisingly, a new peak appeared at around $2\theta = 8.8^\circ$ ($d = 10 \text{ \AA}$), which is under current investigation to determine

its origin. In-plane XRD was performed on the same samples to determine the in-plane crystallinity of RUB-15 nanosheets upon the acid treatment (Figure 2.6c). Films formed with nanosheets in toluene displayed three distinguishable reflections relative to the 002, 020, and 022 planes, and upon *in-situ* acid treatment with acetic acid, the same peak reflections were preserved. Analogously to the out-of-plane measurement, two new peaks have emerged whose investigation is still ongoing (Figure 2.6c).

Preliminary results on a membrane fabricated with the new *in-situ* detemplation method showed a molecular sieving type of transport with a H_2/CO_2 selectivity of 15 and a H_2 permeance higher than 300 GPU (Figure 2.6d) at 300 °C. The newly developed method is a simple way of detemplating zeolitic membranes without resorting to the thermally driven process and could benefit other 2D nanosheets-based zeolites, where mismatches in the thermal expansion coefficients between support and zeolitic phase are the main source of defects formation. Moreover, the room temperature process and its short time (less than 20 minutes) are highly beneficial for the future scale-up compared to the slow heat treatments required in a typical calcination process.

4. Conclusions

Zeolite membranes commercialization is hindered by the prohibitive costs of the inorganic supports and their challenging manufacturing on a large scale. We have reported the first example of polymeric PBI-AM Fumion[®] support obtained by the NIPS process, which could withstand high temperatures (603 K) and was employed for the deposition of thin zeolitic films made of RUB-15 nanosheets for the pre-combustion capture. Zeolites that use mild calcination temperature for the detemplation process could benefit from the new support due to its narrow pores, smooth surface, and chemical and mechanical stability. Two new detemplation processes were developed to allow the safe employment of the PBI-AM support at low temperatures. First, a gentler calcination procedure was used, which was based on longer time treatments (8h) in favor of a milder calcination temperature (330 °C), and XRD studies confirmed the successful removal of the occluded organic molecules and silanol condensation. Second, an *in-situ* room-temperature, liquid-extraction-based method that uses a diluted solution of acetic acid (3 M) in ethanol was sufficient to remove the organic molecules in the gallery spacing of RUB-15 nanosheets, cutting down the number of step and processing time for membrane fabrication. Films obtained from the mild calcination temperature yielded molecular-sieving membranes capable of sieving H_2/CO_2 mixtures and could be employed for the efficient pre-combustion capture. Preliminary results from the *in-*

situ detemplated membranes showed the promise and the potential in delivering attractive H₂/CO₂ selective membranes with only a few fabrication steps ideal for scale-up.

Appendix I

Note 1. The aim of the *in-situ* XRD experiment was to show the transient d spacing shifting and not to obtain the exact d spacing at the beginning and end of the experiment. The error in the d spacing can be up to $\pm 0.3\text{-}0.5$ Å due to the homemade heating cell in which the alignment could not be as accurate as normal XRD measurements. Moreover, the slight wobbling of the stainless steel mesh could contribute to increasing the uncertainty in the measurement. For more accurate d spacing measurements, refer to Figure 2.4c.

Chapter 4. Block-copolymer templated nanoporous carbon membrane for ultrafast hydrogen purification

*Submitted. Mostapha Dakhchoune, Marina Micari, Luis Francisco Villalobos, Kuang-Jung Hsu, Jing Zhao, and Kumar Varoon Agrawal**

Abstract

Nanoporous carbon (NPC) film, fabricated by the pyrolysis of phase-separated block-copolymer/turanose film, has been used successfully as a gas permeable mechanical reinforcement for crack-free synthesis of single-layer graphene membranes. However, a dedicated study on the nanostructure and transport properties of the NPC has been missing. Herein, we show that the NPC film has a perforated lamellar (PL) nanostructure where molecular transport is limited by an interlamellar spacing of ~ 2 nm. The unique PL nanostructure of the NPC film originates from its precursor, i.e., block-copolymer stabilized by hydrogen bonding with a carbohydrate additive where the latter also acts as the main carbon-forming agent. This nanostructure is highly sensitive to the carbohydrate/block-copolymer, and gives away to a lacey structure below 2:1 ratio. Attributing to a thickness of 100 nm and the porous nanostructure, the NPC yields extremely rapid molecular transport. For gases, the transport takes place in Knudsen regime, with H_2 permeance over two million GPU and H_2/CO_2 selectivity over 4.5 in the temperature range of 25 - 300 °C. A techno-economic analysis for the application of NPC membrane for pre-combustion carbon capture reveals that a two-stage membrane process can purify H_2 with extremely low specific membrane area ($0.076 \text{ m}^2 \text{ kgCO}_2^{-1} \text{ s}^{-1}$), which can significantly cut down the footprint of the separation process and the associated capital cost.

1. Introduction

Porous carbon films have obtained increasing attention because of their superior thermal and chemical robustness in harsh environments, high surface area, tunable pore-size-distribution, and electrical conductivity.^{190–192} Their superior properties have led to several applications, e.g., gas separation, catalysis, ultrafiltration, sensors, fuel cells, etc.^{193–196} One of the most studied carbon materials for membrane-based separation is carbon molecular sieves (CMS) comprised of slit-like

pores generated by partial graphitization of polyimides.^{197–199} They have been extensively investigated in the field of gas separation, where separation takes place based on the relative difference in the molecular size.^{200–202} Attractive gas pair selectivities for similar-sized molecules, e.g., for O₂/N₂, N₂/CH₄, CO₂/N₂, etc., by size-sieving have been reported with the CMS membranes.^{203,204} CMS are advantageous because they can be prepared on a large scale from polymeric membrane precursors and their performance and stability are typically superior to their polymer counterparts. Gas separation processes, which require high selectivity under harsh conditions, are particularly suitable for CMS membranes. Strategies to increase the permeance of CMS membranes would likely accelerate their implementation in applications where a high throughput separation is needed, e.g., carbon capture. Decreasing the thickness of their selective layer could be an effective strategy for increasing their permeance.^{193,205} Recently, Ingo and coworkers showed that the nanostructure of the selective layer could be sensitive to the thickness of the CMS film.^{206,207} Therefore, the synthesis of porous carbon films capable of providing a high molecular permeance is highly attractive. In this regard, the extremely thin (~0.5–3 nm) carbon nanomembranes formed by the crosslinking and pyrolysis of self-assembled monolayers (SAMs) of aromatic molecules are promising.^{208–210} The pyrolysis of SAMs forms ~1 nm-thick carbon membranes, and some of the crosslinked SAMs have been used to separate gases.^{210–212} Another class of carbon membranes that have received attention in the past are selective surface flow (SSFTM) membranes developed by Air Products, where the effective pore diameter is in the range of 0.5–0.6 nm, and the gas transport takes place by selective surface diffusion of more strongly adsorbing components.²¹³

In contrast to the abundantly studied carbon membranes hosting sub-1-nm pores, only a handful of reports are available on the study of gas selective carbon membranes hosting pores larger than 1 nm.^{214–218} Most of the studies on mesoporous carbon membranes focused on their structure-property relationship, porosity, and pore-size-distribution; however, the transport properties have not been given adequate attention.²¹⁹ In this range of pore size, the transport of weakly adsorbing gases takes place primarily by Knudsen diffusion in contrast to molecular sieving (activated transport) and surface diffusion.²¹³ The gas permeance, N , in the case of the Knudsen transport, can be expressed as:²²⁰

$$N = \frac{d_p}{RT\delta} \sqrt{\frac{8RT}{9\pi M_w}} \quad (1)$$

where d_p is the pore diameter, R is the universal gas constant, T is the temperature, δ is the membrane thickness, and M_w is the molecular weight of the gas. Eq. 1 shows that the permeance of gas is inversely proportional to the square root of its molecular weight.

Herein, we study transport and accompanying separation data from 100-nm-thick NPC films prepared by pyrolyzing poly(styrene)-*block*-poly(4-vinylpyridine) (PS-*b*-P4VP) hydrogen-bonded with turanose where the latter acts as a carbon source. We probe the morphology, nanostructure, and chemical functionality of the NPC film and study the gas transport properties in the temperature range of 25 - 300 °C. We show that the gas transport from the NPC film is indeed in the Knudsen regime where permeance conforms to the $M_w^{-0.5}$ and $T^{-0.5}$ relationship, as shown in Eq. 1. Given the ultrahigh H₂ permeance (2.9 million GPU) accompanying a Knudsen selectivity for H₂/CO₂ (4.7), we carried out a techno-economic evaluation of NPC film for H₂ purification from its mixture with CO₂ and show that the area needed for NPC film is negligible compared to those for the state-of-the-art membranes for this separation.

2. Methods

2.1. Synthesis of nanoporous carbon film

The synthesis of the NPC film was carried out using a modified method reported by Rodriguez et al.²²¹ Typically, 0.2 g of turanose (Sigma Aldrich) was mixed with 0.1 g of PS-*b*-P4VP (Polymer Source Inc., $M_n^{PS} = 11800 \text{ g mol}^{-1}$; $M_n^{PVP} = 12300 \text{ g mol}^{-1}$; polydispersity index of 1.08), and stirred in 2 g of dimethylformamide (DMF, Sigma Aldrich) for 1 h at 40 °C. The solution was then heat treated in a Teflon-lined autoclave at 180 °C for 3 h to improve the hydrogen bonding between turanose and the P4VP domain. The resulting solution was spin-coated on a smoothened 25- μm -thick copper foil (99.98% purity, Alpha Aesar) at 1500 rpm to form a thin film. The coated film was dried at ambient conditions for 10 min and was subsequently pyrolyzed at 500 °C for 1 h in a reducing atmosphere (87% v/v Ar and 13 % v/v H₂) with heating and cooling rates of 1 °C min⁻¹. The wet-transfer technique was used to transfer the resulting carbon film from the Cu foil to a porous substrate.²²² Briefly, a 20% (w/w) aqueous solution of sodium persulphate (Sigma Aldrich) was used to etch the foil. The floating NPC film was rinsed several times with deionized water to eliminate the residues from the etching step. Finally, the NPC film was scooped with a target membrane support (either a 50- μm -thick tungsten foil comprising of 2500 5- μm -sized holes in 1

mm² area or a large-area polyethersulfone (PES) support with a pore size of 100 nm). The scooped films were dried overnight at room temperature.

2.2. Characterization

Scanning electron microscopy (SEM) images were taken with an FEI Teneo microscope operating with an acceleration voltage of 1-2 kV and a working distance of 2-6 mm. The NPC films were imaged without any conductive coating. Pore-size-distribution was done using ImageJ by analyzing 370 pores imaged by SEM. Transmission electron microscopy (TEM) images were obtained with an FEI Tecnai G2 Spirit Twin microscope operating with a 120 kV incident electron beam.

Thermogravimetric analysis (TGA) was performed with a Perkin Elmer TGA 8000 with heating and cooling rates that simulated the pyrolysis experiment. Due to the low concentrations of the carbohydrate and the copolymer in DMF, the TGA experiment was carried out by first evaporating DMF at room temperature. The Fourier transform infrared (FTIR) measurements were carried out with a Perkin Elmer Spectrum Two spectrometer in which both the background and sample spectra were recorded 16 times. The X-ray photoelectron spectroscopy (XPS) analysis was conducted on the NPC film using the monochromated K α line of an aluminum X-ray source (1486.6 eV). The analyzer was set at a pass energy of 20 eV. During the measurements, the samples were electrically connected to the sample stage. The peak fitting was performed after a Shirley background was subtracted. X-ray diffraction (XRD) was performed with a Bruker D8 Advance instrument using CuK α radiation (λ = 1.5406 Å). UV-Vis analysis was performed on a PerkinElmer LAMBDA 365 spectrophotometer. Rejection was calculated as $(1 - C_{perm}/C_{ret}) \times 100$, where C_{perm} and C_{ret} are the concentration of the permeate and retentate streams, respectively.

2.3. Gas permeation measurements

Single gas permeation measurements were performed with a constant-pressure variable-volume setup (Figure 4.1). The feed side of the membrane was maintained at a fixed pressure with a backpressure regulator (Swagelok), and the volumetric flow rate of the permeate stream was measured with a bubble flow meter. Temperature-dependent permeation studies, in the range of 25-300 °C, were carried out by placing the membrane module in a convection oven. The permeances of H₂, He, CH₄, N₂, CO₂, and SF₆ were obtained by measuring the time, t_v , needed to have a certain volume of gas, V_i , in the bubble flowmeter using Eq. 2:

$$N_i = \frac{V_i}{\tilde{V} A t_v \Delta P} \quad (2)$$

where \tilde{V} is the molar volume of the permeate, A is the membrane area, and ΔP the transmembrane pressure difference. The selectivity between gases i and j , α_{ij} , was obtained using Eq. 3.

$$\alpha_{ij} = \frac{N_i}{N_j} \quad (3)$$

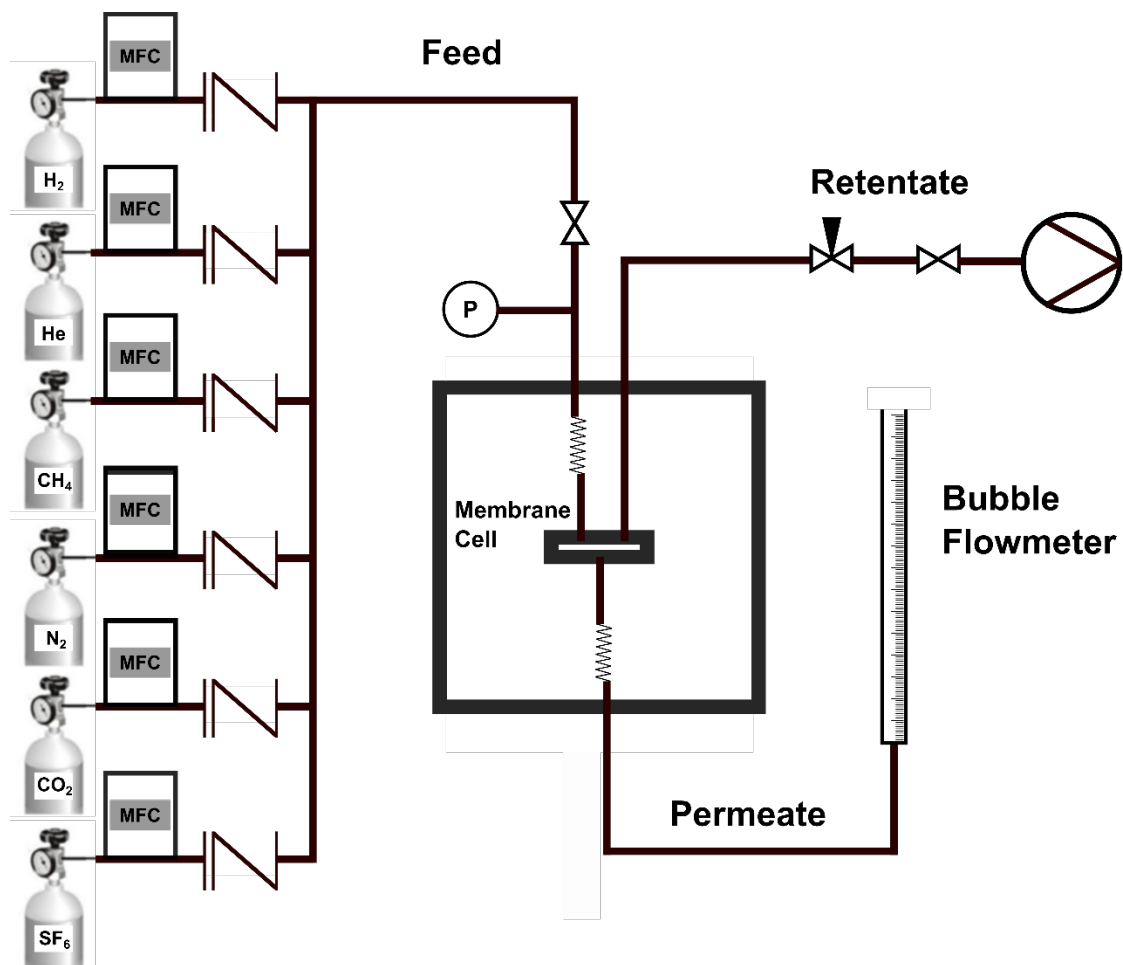


Figure 4.1. Schematic of the home-made permeation setup.

2.4. Method for techno-economic analysis

2.4.1. Model

The NPC membranes are investigated for pre-combustion carbon capture in the integrated gasification combined cycle (IGCC) process. The IGCC power plant operates with an air separation unit to produce oxygen. O_2 and H_2O are then fed to a fossil fuel gasifier at high temperature and pressure. The syngas produced in this way undergoes a number of treatment processes to remove the contaminants, i.e., particulate and sulfur compounds, and to convert CO and H_2O into CO_2 and H_2 . Finally, the treated gas is fed to the burner, which produces a hot, high-pressure gaseous stream that is sent to a gas turbine to generate electricity. However, burning the gas with high content of CO_2 contributes to carbon emissions. This is typically avoided by carrying out H_2/CO_2 separation (pre-combustion capture) before the gas enters the burner. This leads to an H_2 -rich stream for combustion and a CO_2 -rich stream, which is then cooled and compressed to obtain a liquid CO_2 stream for storage. The pre-combustion capture works in favorable conditions for membranes as the concentration and pressure of the feed stream are high. Therefore, membrane-based separation processes have been proposed in the literature as an alternative to the state-of-art physical absorption processes such as Rectisol[®] or Selexol[™] to reduce the capital investment.^{78,223,224}

To design and simulate NPC-membrane-based H_2/CO_2 separation process, we adapted a technical model reported by our group.²²⁵ The model simulates different system configurations, e.g., single-stage, double-stage with either an enricher cascade or a stripper cascade, and estimates the amount of each component recovered and their purity for a given membrane geometry. Conversely, for a given target value of recovery and purity of one component, the model calculates the needed membrane area for the selected configuration at the fixed operating conditions (pressures, temperature) to achieve the targets.

Each stage of the membrane system is composed of a membrane unit with cross-flow configuration, which is discretized along the length in N discretization elements. The membrane unit is modeled under the following assumptions: (i) the transmembrane flux does not depend on the mixed composition in the permeate channel since the flux is collected immediately in each discretization element; (ii) the permeance of each component is independent of pressure; (iii) pressure drops and concentration polarization are negligible; (iv) the process is isothermal.

In each discretization element, the flux J_i [mol/(m²s)] of each component i through the membrane is defined as in equation (4), where N_i [mol/(m²sPa)] is the permeance of the component, P_{feed} [Pa] and P_{perm} [Pa] are the total pressures in the feed and permeate channel, respectively, and x_i^f

$[-]$ and $x_i'^p [-]$ are the molar fractions of the component in the feed channel and in the permeate channel, just after crossing the membrane:

$$J_i = N_i (P_{feed} x_i^f - P_{perm} x_i'^p) \quad (4)$$

Starting from the definition of the transmembrane flux in each discretization element, the model can estimate the profiles of total molar flow rates and molar fractions of each component in the permeate and feed channels by mass balances.

The simulation of double-stage systems is based on the combination of the models of two single stages where the feed flow rate and the composition of the second stage are either those of the permeate produced by the first stage in the case of the enricher cascade or those of the first-stage retentate in the case of the stripper cascade. In addition, the double-stage systems investigated in this work include a recycle stream to improve the recovery. In the case of the enricher cascade, the second-stage retentate is recycled and mixed with the feed, whereas, in the stripper cascade, the second-stage permeate is recycled. To simulate a system with recycle, the model presents an iterative procedure that runs until the convergence criteria are fulfilled. In particular, the differences between the calculated and the guess recycle flow rate and composition have to be lower than a set tolerance.

Finally, for the design of a system to achieve the given recovery and purity targets, the model has an optimization procedure that finds the membrane area for each stage corresponding to the minimization of the sum of the squared errors between the calculated and the required recovery and purity.

Apart from the membrane area, another important term for the economic assessment is the electric power consumption of the membrane system. The power consumption is given by the sum of the compression and the cooling power. The compression power depends on the operating pressures in the channels of each membrane stage and in the down-stream operations (the H_2 -rich stream is sent to combustion, and the CO_2 -rich stream is sent to a condenser to obtain liquid CO_2). The cooling power is required to cool down the CO_2 -rich stream before the condenser because the typical release temperature of the feed gas, is between 150 and 200 °C. The power consumption of each compressor is defined in Eq. 5 where $Q_{in,compr}$ [mol/s] is the molar flow rate entering the compressor, η_{compr} [-] is the efficiency of the compressor, γ [-], R [J/(mol K)] and T [K] are the

adiabatic index of the inlet stream, the gas constant, and the temperature, respectively, and P_{high} [Pa] and P_{low} [Pa] are the outlet and the inlet pressures of the compressor.

$$P_{compr} = \frac{Q_{in,compr}}{\eta_{compr}} \frac{\gamma}{\gamma - 1} RT \left[\left(\frac{P_{high}}{P_{low}} \right)^{\frac{\gamma-1}{\gamma}} - 1 \right] \quad (5)$$

The main outputs of the technical model are used for the economic assessment, to estimate the capital and operating costs of the membrane process, the specific CO₂ capture cost and the increase in the levelized cost of electricity (LCOE) due to the CO₂ capture. The capital costs include the cost for the membranes and for the compressor, and the operating costs account for the cost of the total electricity demand and maintenance. The equations used for these estimations are reported in Micari et al.²²⁵ The CO₂ specific cost, C_{CO_2} [\$/tonCO₂], is calculated as per Eq. 6 where CAPEX and OPEX [\$/y] are the annualized capital and operating expenses and CO_{2prod} [ton/y] is the amount of CO₂ produced per year.

$$C_{CO_2} = \frac{CAPEX + OPEX}{CO_{2prod}} \quad (6)$$

The LCOE with CO₂ capture is calculated by taking into account the additional expenses due to the separation process and the net power produced, given by subtracting the power demand of the membrane system from the total power produced by the power plant.

2.4.2. Inputs and parameters

The simulations have been performed with reference to an IGCC power plant producing 556 MW_{el} where the gas feed flow rate to be treated in the membrane unit is 565 ton/h.⁷⁸ For simplicity, the feed gas has been considered as a binary mixture of CO₂ and H₂ with fractions equal to 40% and 60%, respectively. The feed temperature and pressure are 150 °C and 50 bar, respectively, as reported in the literature.⁷⁸ The operating pressures in the membrane stages are optimized to reduce the specific CO₂ cost while fulfilling the criteria concerning the recovery and purity targets. The membrane performance is simulated with H₂ permeance of 4.5×10⁶ GPU and the H₂/CO₂ selectivity of 4.7 in agreement with the experimental data. The power of the compressors is calculated with an efficiency factor of 85%.

Once the CO₂-rich and the H₂-rich stream are produced by the membrane process, these have to be compressed for the downstream steps. In particular, the CO₂-rich stream is compressed up to 110 bar and cooled down to 20 °C to be condensed, and the H₂-rich stream is compressed up to 32 bar for the combustion. For the economic parameters, the membrane cost including the module, the housing, the piping and instrumentation, is considered as 100 \$/m². Also, the lifetime for membranes and compressors are taken as 5 and 25 years, respectively, and the electricity cost is taken as 0.05 \$/kWh.

3. Results and discussions

3.1. Fabrication of nanoporous carbon membranes

The NPC films were prepared by the soft-templating of the carbon precursor, turanose, using block-copolymer (PS-*b*-P4VP) on a Cu foil.²²¹ For this, first, a transparent solution of precursors in DMF was heat-treated at 180 °C for 3 h to promote the hydrogen-bonding interaction between turanose and the pyridine group of the P4VP block, upon which the color of the solution turned black. A control experiment where only turanose, dissolved in DMF, was heated at 180 °C for 3 h, the same color transition could be observed, indicating a partial degradation of the carbohydrate. The heat treatment step to promote hydrogen bonding of turanose and block-copolymer is crucial for controlling the morphology of the resulting films prepared by spin coating.²²⁶ NPC films prepared without this heat-treatment yielded non-uniform morphology (Figure 4.2), and ordered as well as disordered domains could be observed.

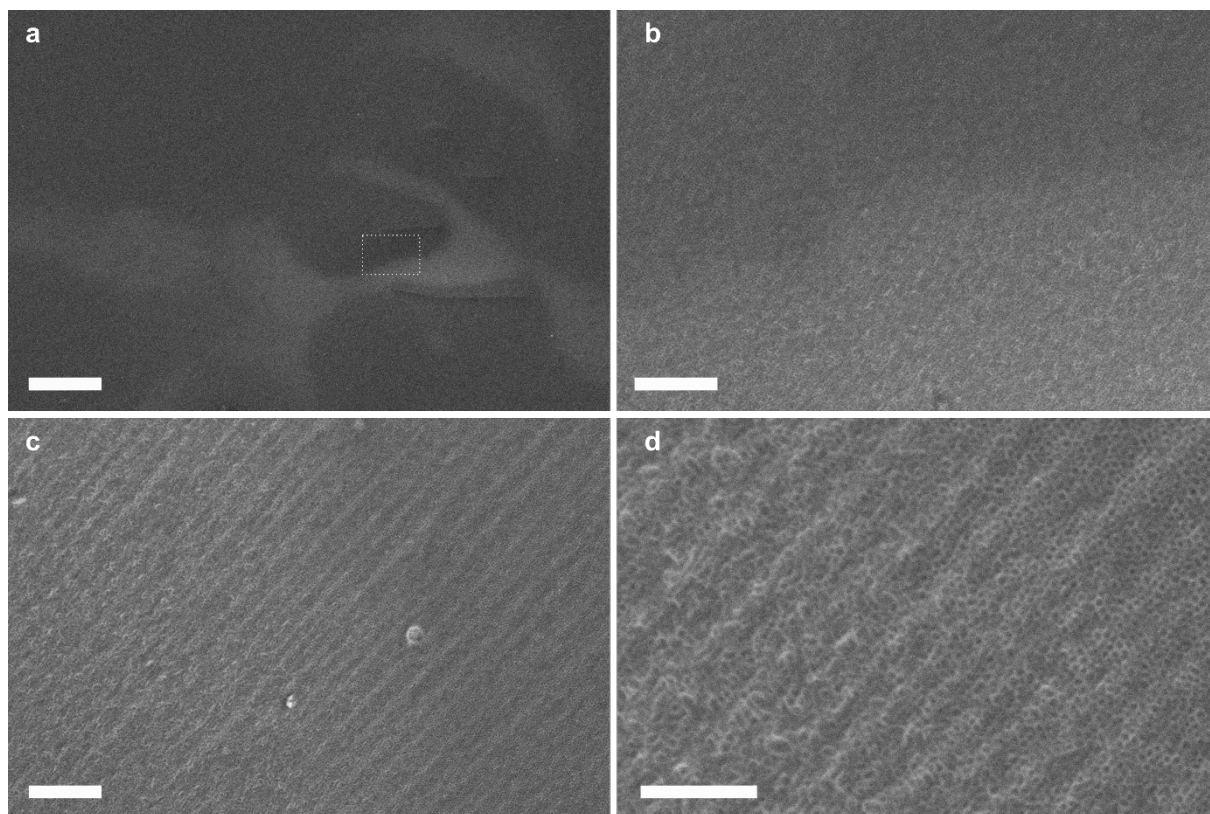


Figure 4.2. SEM images of the NPC film without the 180 °C heating step. a) Low-magnification showing white and black regions consisting in uniform and non-uniform NPC patterns, respectively. b) Zoomed image of the rectangular region in (a). c) and d) show the pattern transition from uniform (top-right) to irregular (bottom-left). Scale bars are 10 μm in (a), 1 μm in (b) and (c), 500 nm in (d).

Thin films were prepared on a smoothened Cu foil where, upon drying, the hydrophobic and hydrophilic components are expected to undergo phase-separation.^{227,228} The pyrolysis of the precursor film gave way to a uniform NPC film (Figure 4.3a). The degree of order in the pyrolyzed structure depends on the capacity of the precursors to arrange in ordered and oriented nanostructure before the pyrolysis step. Russel and coworkers reported tunable ordering of the phase-separated domains by controlling the solvent evaporation from the casted polymer film by exposing the casted film to various solvent mixtures at high temperature.²²⁹ However, this process is complex and time-consuming, and therefore, we decided to directly pyrolyze the casted film.

Figure 4.3b shows the top-view SEM image of the pyrolyzed films. The film was uniform over the entire coated surface (10 cm^2) without any signs of cracks or defects. Pore opening, with an average size of ~ 20 nm (Figure 4.3f), could be observed on the top surface of the film. To probe asymmetry in the morphology of the NPC film due to evaporation-induced variation of DMF concentration at the drying front, the backside, and the cross-section of the NPC film were imaged. For imaging the

backside, the NPC film was suspended over a window of a TEM grid (Figure 4.3c). Corresponding images revealed that the backside also had a pore opening of ~ 20 nm. A cross-section image of the film indicated that the film was only 100-nm-thick (Figure 4.3d). Interestingly, the image indicated the presence of a lamellar morphology where porous sheets of carbon are arranged on top of each other. This was also evident from the TEM study where the sample was tilted by 60° with respect to the focal plane of the beam (Figure 4.3b) and is further confirmed by X-ray diffraction where a Bragg peak is observed (XRD, discussed later). This likely has origin in the perforated lamellar (PL) morphology reported for PS-*b*-P4VP films with P4VP phase hydrogen-bonded to a homopolymer. It is reported that PL morphology for block copolymer is stabilized by the hydrogen bonding with the homopolymer.^{230,231} We speculate that turanose stabilizes the PL morphology by hydrogen bonding with the P4VP block. Given that turanose (i) yields the majority of the carbon in the final film and (ii) degrades faster than the block-copolymer (TGA data, discussed later), the templating effect (PL morphology) is mimicked in the pyrolyzed carbon film.

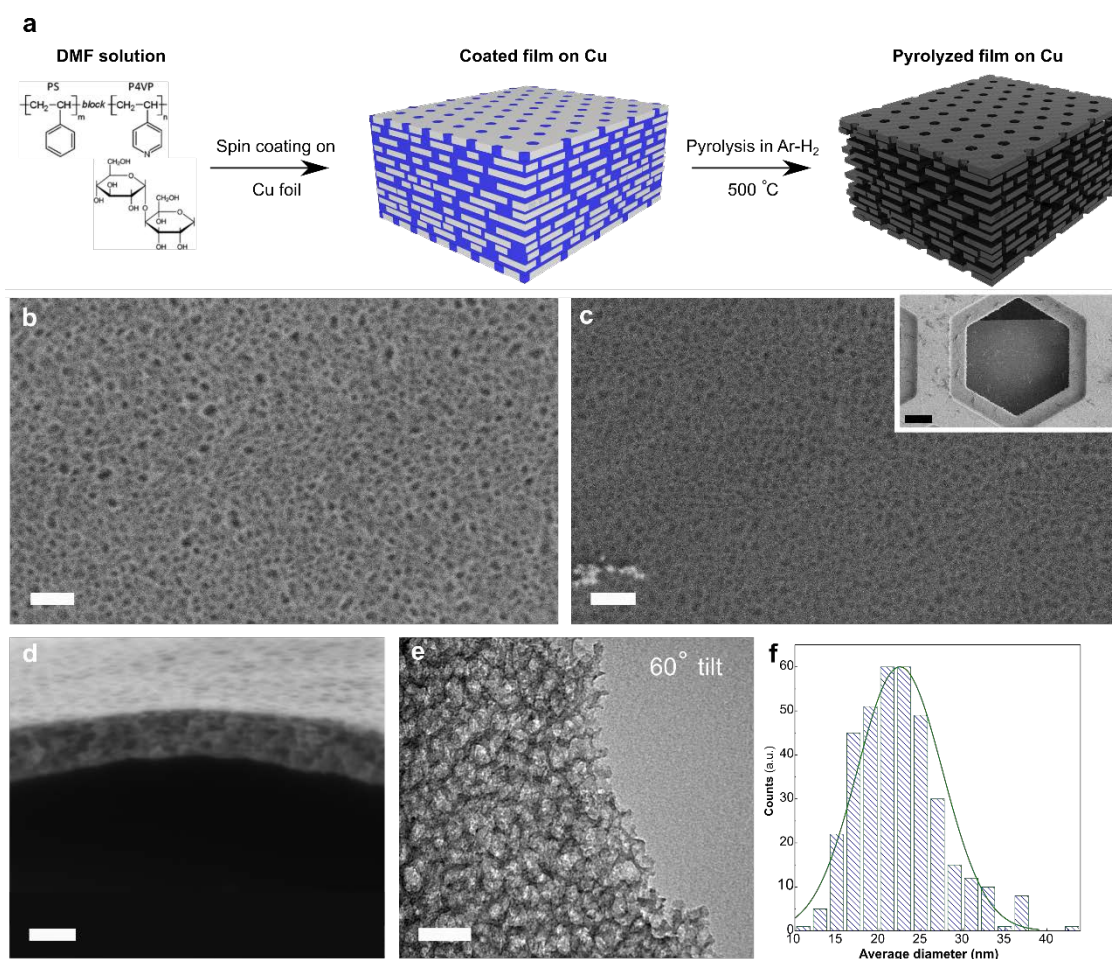


Figure 4.3. a) Schematic illustration of the process for preparing the NPC membrane, including dissolution and heat-treatment of the carbohydrate and the block-copolymer in DMF, spin-coating on Cu foil, and pyrolysis at 500 °C in a reducing atmosphere. Blue domains are rich in the PS phase, while the grey domains are rich in the P4VP-turanose. b) Top-view SEM image of the NPC showing its nanoporous structure. c) SEM image of the

backside of the NPC film that was contacted the Cu foil. Inset shows the transferred film on the TEM grid, which was flipped to image the backside. d) Cross-sectional SEM image revealing a thickness of ~100 nm. e) TEM image of the edge of NPC tilted at an angle of 60° with respect to the back focal plane. f) Pore-size-distribution showing an average pore opening of ~22 nm. Scale bars are 200 nm in (b) and (c), 10 μ m in the inset of (c), 100 nm in (d), and 50 nm in (e).

3.2. NPC morphology as a function of turanose/copolymer ratio

The synthesis of a porous carbon film by the pyrolysis of a block copolymer film is highly challenging.²³² This is mainly because most block copolymers yield a low residual carbon mass upon pyrolysis. An additive that can preferentially interact with one of the blocks and has a high carbon yield can enable block copolymer as a template for the fabrication of a nanostructured carbon film. In the presented system, turanose has such a function. It preferentially interacts with the P4VP block via hydrogen bonding and has a high carbon yield upon pyrolysis. Therefore, choosing the right ratio between turanose and the block-copolymer is crucial to obtain a continuous, porous, and mechanically-sturdy structure.

TEM images in Figure 4.4a-d reveal the morphological changes in the NPC film as a function of the turanose/block-copolymer ratio. As expected, when the ratio was decreased from 2:1 (w/w) to 0.25:1, the film thickness reduced, and the porosity increased. However, even with the ratio of 1:1, the uniformity in the porous structure was reduced (Figure 4.3b). This indicates that the templating is not effective at the ratio 1:1 or below, likely from the structural collapse of the block-copolymer near the pyrolysis temperature. Indeed, the TGA data shows that the block-copolymer is removed at temperatures higher than 450 °C (see next section).

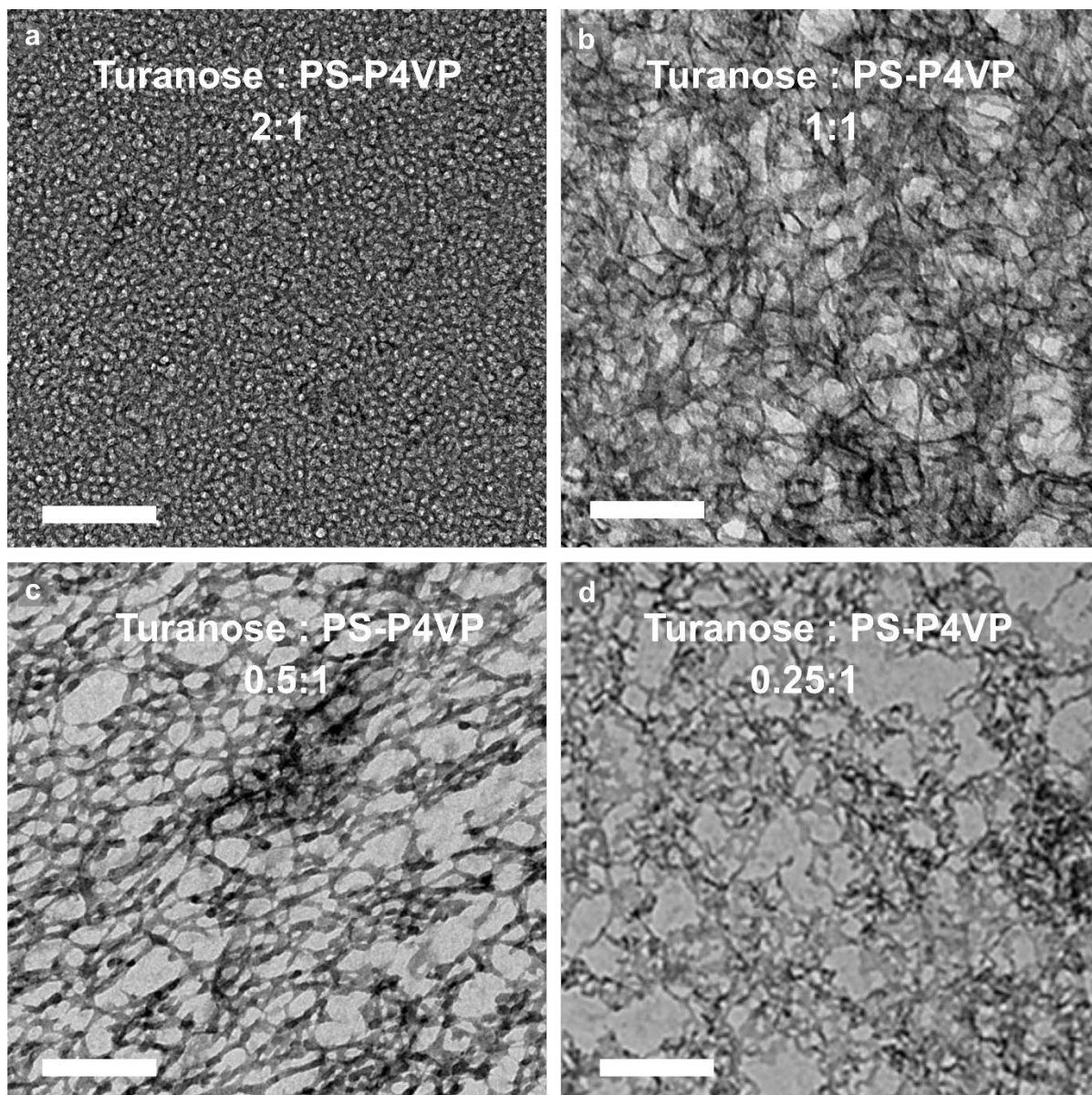


Figure 4.4. TEM images showing the morphological changes in the NPC film as a function of the turanose/PS-*b*-P4VP ratio. Scale bars correspond to 250 nm.

3.3. Chemical composition and structure of the NPC film

To understand the pyrolysis behavior of turanose and the block copolymer, TGA of precursor film as well as of turanose and block-copolymer powders were carried out with a heating rate of 1 °C/min, similar to that for the synthesis of the NPC film. For the former, the solvent was evaporated before conducting the TGA to obtain a reasonable amount of starting material in the TGA pan for pyrolysis. In this case, the weight loss below 200 °C can be mainly attributed to the removal of residual DMF, while above 200 °C, weight loss kicks off from turanose degradation. It seems that hydrogen bonding of turanose with the block-copolymer delays the degradation of the block-

copolymer from ~350 to ~400 °C. At 500 °C, the degradation of turanose/block copolymer was complete, which results in a carbon framework of the NPC film.

XRD data of the NPC films confirms our microscopy-based observation of a lamellar structure. An interlayer spacing of 5 nm, comprising of the thickness of individual lamella and the interlamellar spacing, is revealed (Figure 4.5b). Given the likely origin of the nanostructure with the PL phase of block-copolymer/turanose film, the thickness of the lamella is expected in the range of 2-4 nm, consistent with the thickness of the pore wall observed by TEM (Figure 4.3e and Figure 4.4). According to this, the interlamellar spacing is expected to be in the range of 1-3 nm. The absence of a strong Bragg peak in the wide-angle region confirms the absence of significant graphitic domains. This indicates that NPC film is composed of amorphous carbon.²³³

FTIR spectroscopy was carried out to understand the chemical composition of the NPC film (Figure 4.5c). The stretching vibration peaks around 1580 cm⁻¹ can be assigned to the C=C bond of the aromatic ring²³⁴, while the peak around 1700 cm⁻¹ indicates the presence of C=O bond²³⁵, likely originating from the opening of an aromatic ring. The ensemble of peaks in the range of 900-700 cm⁻¹ is related to the bending vibration of C-H bond.²³⁵ The peak at ~1063 cm⁻¹ was ascribed to the stretching vibration mode of the C-O bond.²³⁶ The very broad peak in the region of 1400-1150 cm⁻¹ hindered the identification of aromatic amine groups. This was resolved by the XPS data, which clearly showed the presence of C-N and C=N functional groups (Figure 4.5e) and confirmed the findings on C=O and C-O (Figure 4.5d, f) from the FTIR study. The concentration of O bonded as C=O and C-O was 1.86 and 5.25%, respectively. The concentration of N was 5.54%. The presence of these oxygen and nitrogen functional groups in the NPC film makes it hydrophilic.

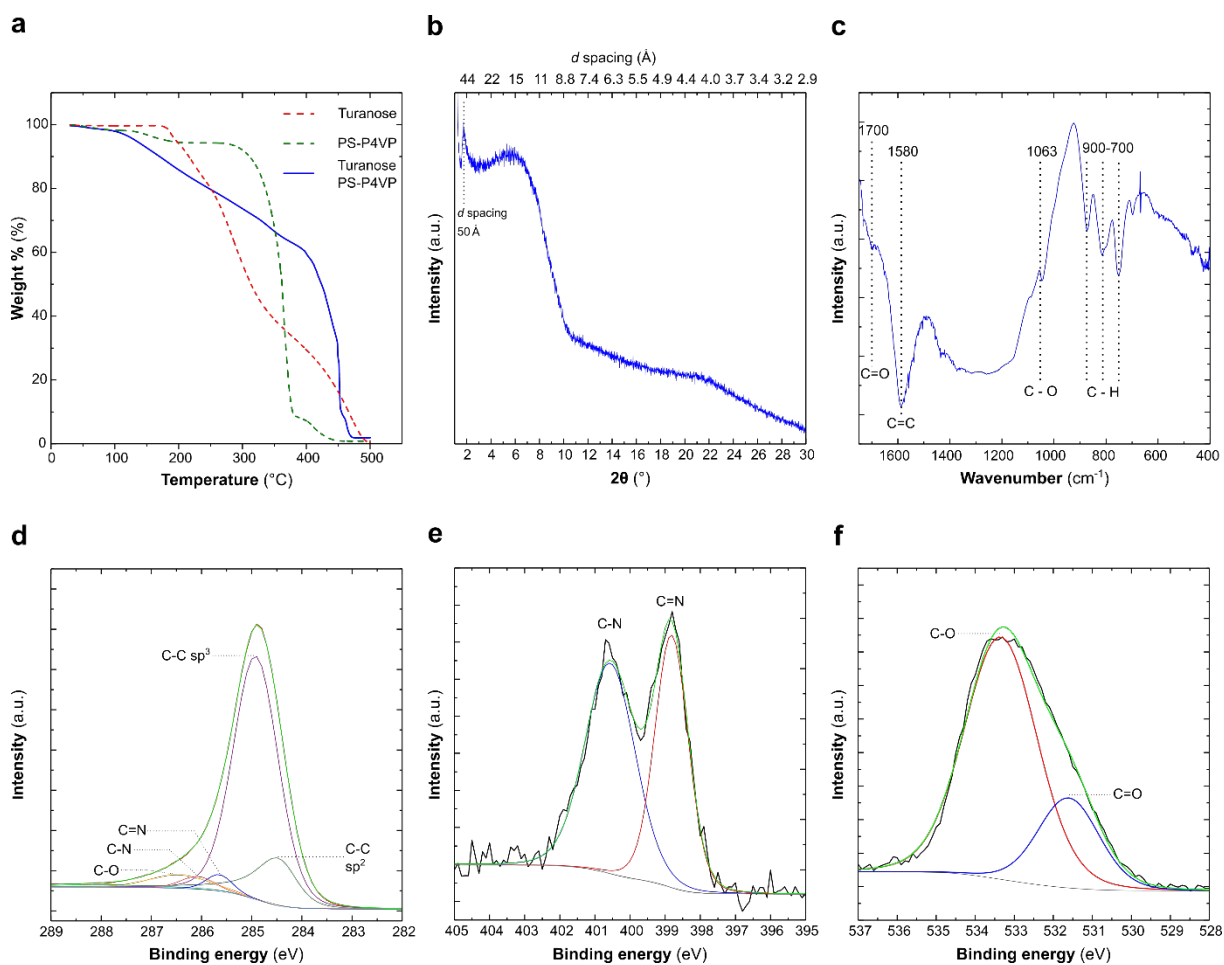


Figure 4.5. a) Thermogravimetric analysis of turanose and PS-P4VP powder as well as that of precursor film of NPC. The final weights of the three curves are reported in Figure 4.6. X-ray diffraction (b) and FTIR (c) of the NPC film. XPS of the NPC film with spectra for C1s (d), N1s (e), and O1s (f).

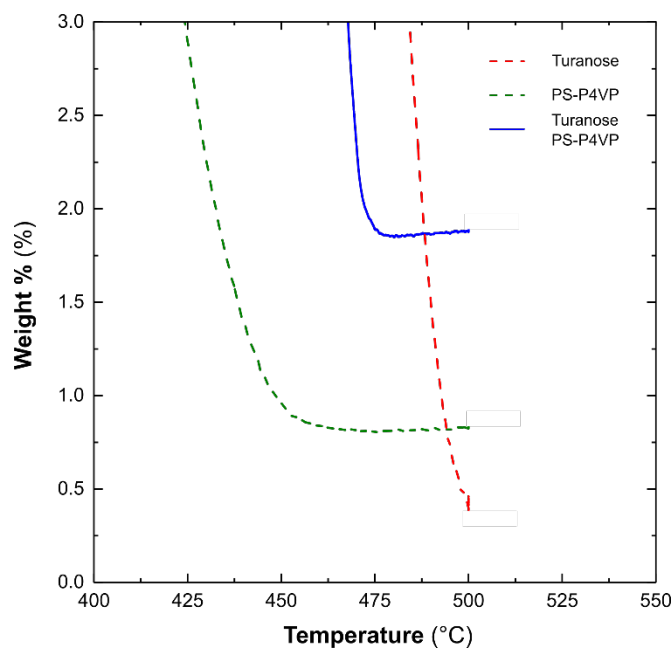


Figure 4.6. Zoomed TGA data from Figure 4.5a.

3.4. Gas transport properties from NPC membrane

The permeation properties of H₂, He, CH₄, N₂, CO₂, and SF₆ through NPC membranes, prepared by transferring the film on a macroporous tungsten support hosting 5- μ m-sized laser-drilled holes, were analyzed using a permeation setup based on constant-pressure variable-volume measurement (Figure 4.1). Given that the pore openings in the NPC films are ~20 nm in size and the interlamellar spacing is expected around 1-3 nm, the transport of gases considered in this study is expected to take place by the Knudsen diffusion mechanism where the permeance of gas scales as $M_w^{-1/2}$ and $T^{1/2}$ (Eq. 1). Indeed, we found this relationship between these parameters suggesting a primarily Knudsen transport (Figure 4.7).

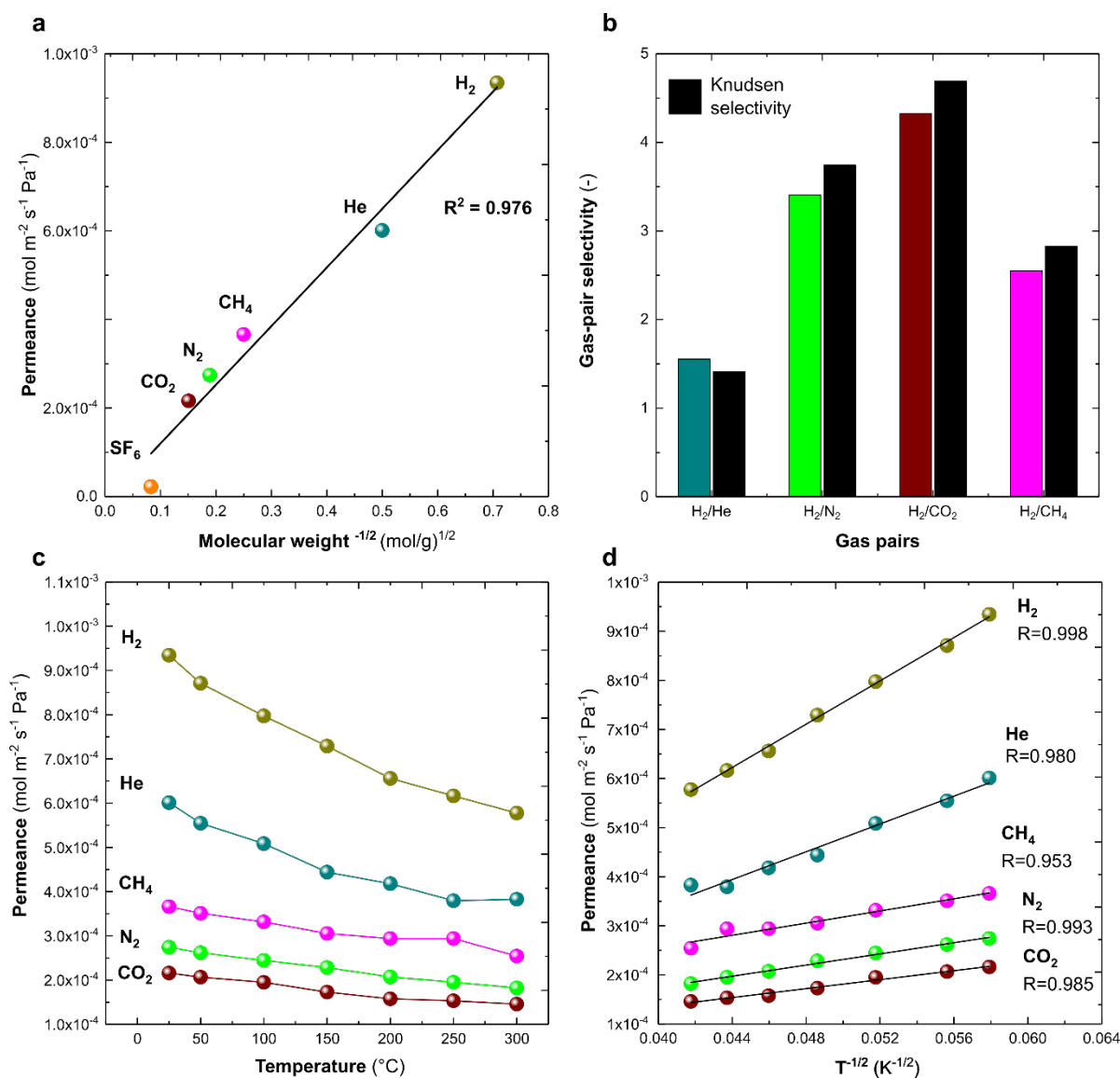


Figure 4.7. a) Permeance of gases as a function of $M_w^{-1/2}$. b) Ideal selectivities of H₂ with respect to various gases and comparison with the Knudsen predicted values (black bars). c) Permeance of gases as a function of

temperature in the range of 25-300 °C. d) Permeance of gases from (c) displayed as a function of $T^{-1/2}$. All data were collected at 3.2 bar feed pressure.

A linear regression of the permeance with $M_w^{-1/2}$ and $T^{-1/2}$ led to values of goodness of fit, R^2 , close to 1 (0.983 and 0.989, respectively, Figure 4.7a, d). As a result, the transport rate decreased for the gases with a higher M_w ($H_2 > He > CH_4 > N_2 > CO_2 > SF_6$) and upon increasing the temperature (25-300 °C). H_2 permeance decreased by more than 1.6-fold when the temperature was increased from 25 to 300 °C. A similar decrease was observed for CO_2 and the rest of the gases (Figure 4.7c). Figure 4.7b shows a comparison between the theoretical Knudsen gas selectivities and those obtained from the NPC film. The experimental and theoretical values are in good agreement for all the gas pairs. This led to the realization of attractive gas pair selectivities (H_2/SF_6 , H_2/CO_2 , H_2/N_2 , H_2/CH_4 , and H_2/He selectivities of 8.8, 4.3, 3.4, 2.6, and 1.6, respectively). A large H_2 permeance of ~2.9 million GPU was achieved, attributing to the small thickness (100 nm) of the NPC film in combination with its porous nanostructure. The enormous H_2 permeance of ~2.9 million GPU positions NPC membrane as one of the most permeable membranes suited for H_2/CO_2 separation among membranes in the literature with selectivity > 4 (Figure 4.8). The only material that yields a higher H_2 permeance (~22 million GPU) and close to Knudsen H_2/CO_2 selectivity (3.8) is nanoporous single-layer graphene membrane, reported by Park and coworkers in 2014.²³⁷

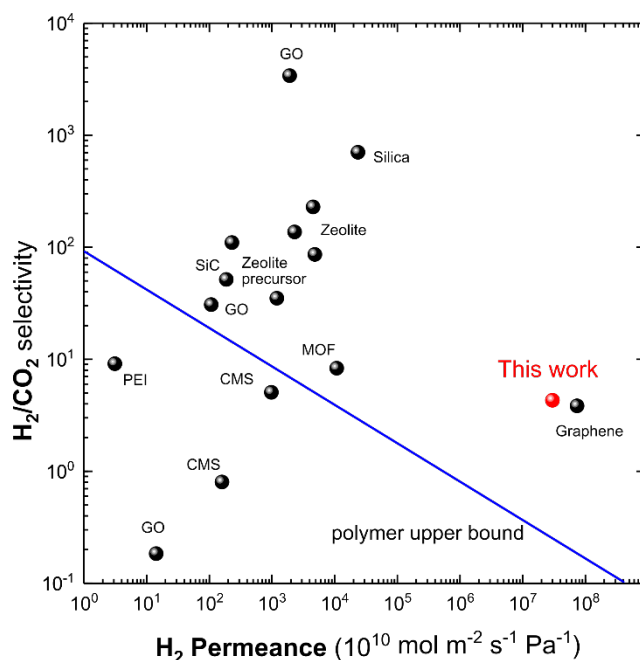


Figure 4.8. Robeson plot for H_2/CO_2 comparing various types of membranes in literature. GO,^{30,238} PTMSP,²³⁹ PEI,²⁴⁰ CMS,²⁴¹ zeolite,^{242,243} zeolite precursor,⁹² graphene,²³⁷ silica,²⁴⁴ MOF,²⁴⁵ and SiC.²⁴⁶

3.5. Interlamellar liquid transport

To understand the limiting transport channel in NPC in the context of PL microstructure, we carried out molecular cut-off experiments probing the transport of solvents and molecules dissolved in a solvent. Water permeation behavior was measured by pressurizing the feed to 6 bar and measuring the volume of the permeate as a function of time. Interestingly, the water permeance was extremely high at the start of the measurement ($8400 \text{ L m}^{-2} \text{ h}^{-1} \text{ bar}^{-1}$) but dropped to a stable value of $\sim 100 \text{ L m}^{-2} \text{ h}^{-1} \text{ bar}^{-1}$ within an hour (Figure 4.13a). A similar behavior was observed for an organic solvent, hexane (Figure 4.9).

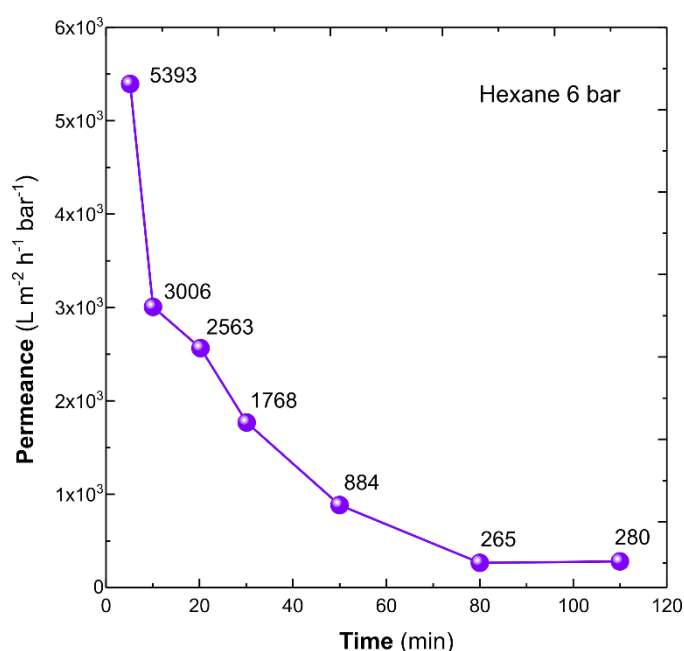


Figure 4.9. Hexane permeance as a function of time with a feed pressure of 6 bar at 25 °C.

This behavior indicates that the 20-nm-sized pore opening at the NPC surface of the film does not necessarily continue as cylindrical channel across the entire thickness of the film. Rather, they open to the underlying lamella, and in this way, the transport is limited by the interlamellar spacing. Given that the transport of liquid solvents takes place with the viscous diffusion regime where the flow rate is a quadratic function of the pore area (Eq. 7), a slight decrease in channel size upon compression can explain the permeance decrease.

$$Q = \frac{A_{pore}^2}{8 \pi \mu L} \Delta P \quad (7)$$

where Q , A_{pore} , μ , and L are the volumetric flow rate, the cross-sectional area of the transport channel, dynamic viscosity, and the film thickness, respectively.

To understand the interlamellar spacing, we conducted filtration experiments probing size cut-off. When 6-nm-sized CdSe nanoparticles with a concentration of 30 mg L^{-1} in hexane were used, we observed a significant deposition of nanoparticles on top of the film, making it difficult to predict rejection (Figure 4.10 and Figure 4.11). Therefore, we filtered a smaller molecule, acid fuchsin dye (585.45 Da), with an approximate size of 1.5 nm ²⁴⁷.

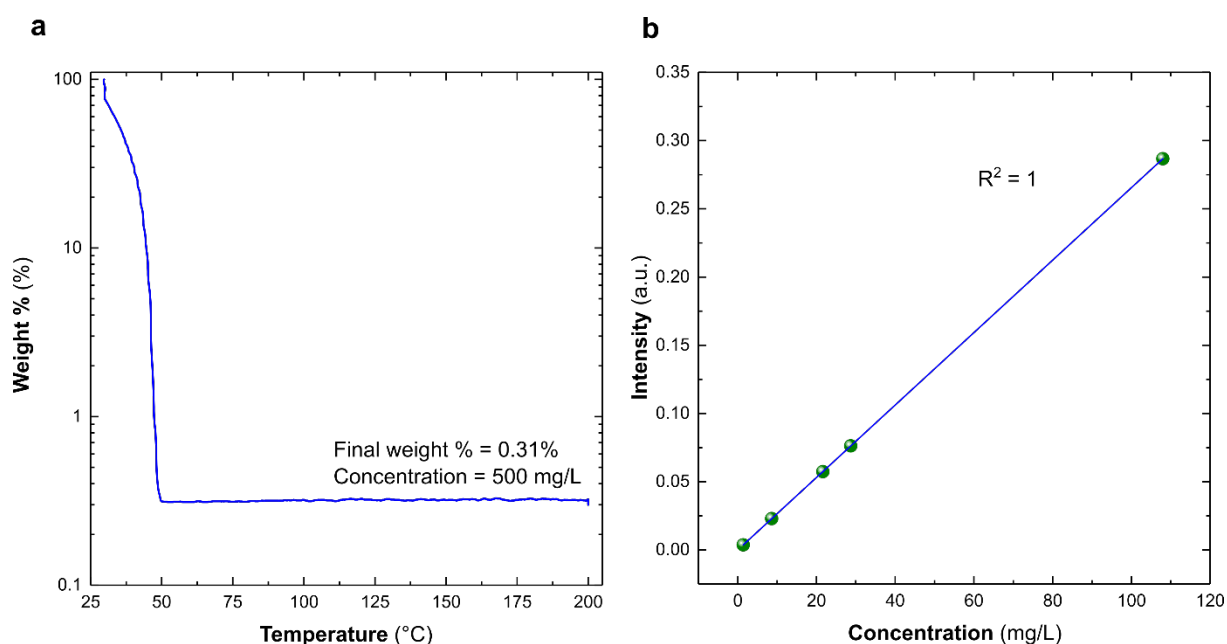


Figure 4.10. a) Thermogravimetric analysis of the quantum dots dispersion (QDs) in hexane with a heating rate of $5^\circ\text{C}/\text{min}$. b) UV-Vis calibration curve of the QDs in hexane.

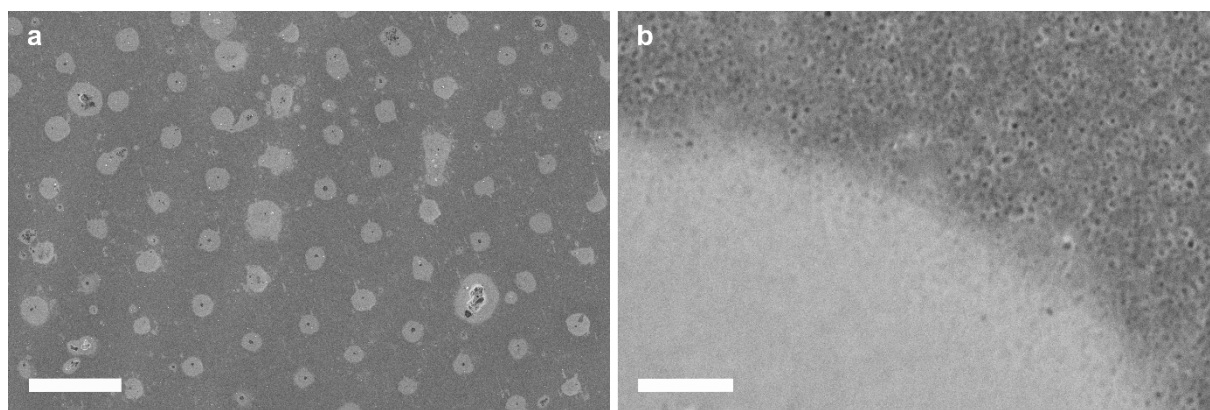


Figure 4.11. Low a) and high b) magnification SEM images of NPC membrane supported on tungsten after the cut-off experiment with quantum dots (QDs). The agglomeration of the QDs at the tungsten pores was evident

from the brighter contrast given by the QDs metallic phase compared to the NPC phase. Scale bars are 30 μm in (a) and 500 nm in (b).

To obtain a sufficient quantity of permeate volume, a large-area (~ 0.5 cm in diameter) NPC film was used. These membranes were prepared by transferring the NPC film on a self-standing PES support with an average pore size of ~ 1 μm (Figure 4.12). The dye was dissolved in acetonitrile with a feed concentration of 32 μM .

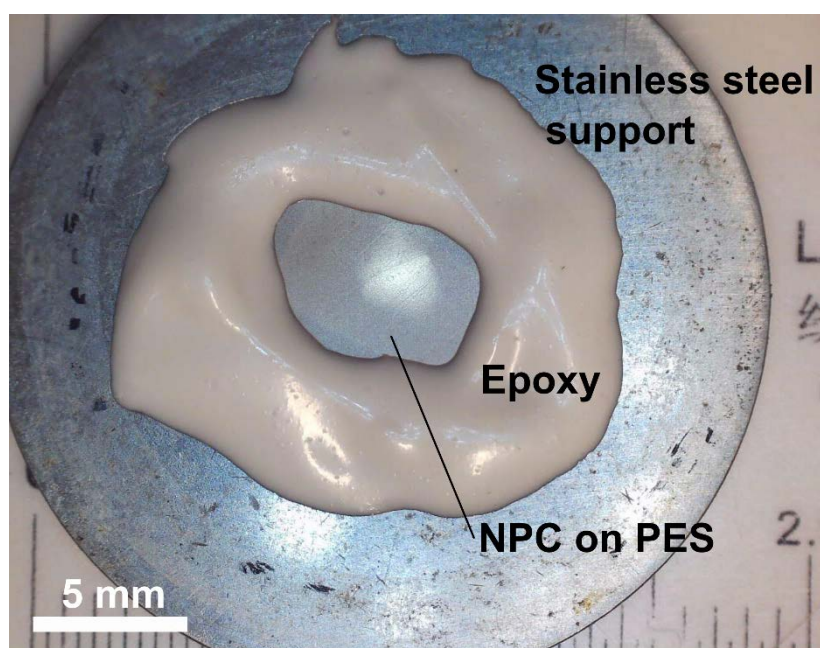


Figure 4.12. NPC membrane supported on polyethersulfone (PES) membrane with an average pore size of 1 μm . The NPC-PES system was supported on a stainless steel mesh to provide mechanical reinforcement, as reported in our previous work.²⁴⁸ The gas sealing was ensured by using an epoxy resin.

According to our calibration of dye concentration based on UV-Vis spectroscopy, the concentration of the dye in the permeate was 7.5 mM, corresponding to a rejection of 76% (Figure 4.13b). Given the small size of the dye, this experiment confirms that the 20 nm pores in NPC do not connect the top and bottom sides of the films and that the transport is limited by the interlamellar spacing of the NPC film. Based on the size of the dye, it is likely that the interlamellar spacing is ~ 2.0 nm in size.

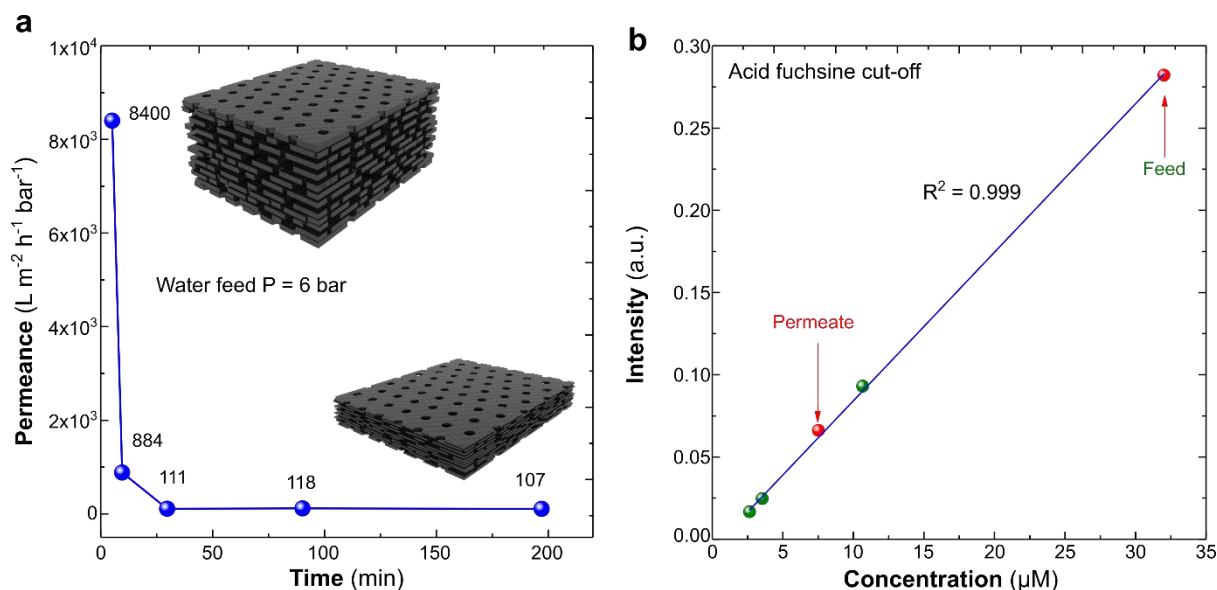


Figure 4.13. a) H₂O permeance as a function of time with a feed pressure of 6 bar at 25 °C. Top and bottom schematics represent the potential configuration of the NPC at the start and end of the experiment. b) Cut-off experiment with fuchsine acid in acetonitrile. The green spheres and blue lines are the calibration data and the fitting, respectively. The red spheres represent the data from the filtration experiments.

3.6. Techno-economic analysis for pre-combustion carbon capture

As mentioned above, the NPC membranes with an H₂ permeance of ~2.9 million GPU appear to be extremely attractive for high throughput H₂/CO₂ separation. Motivated by this, we carried out a techno-economic analysis to better understand the opportunities in deploying the NPC membrane for the pre-combustion carbon capture. The schematics of a single-stage process and a double-stage process with an enricher cascade considered in this study are shown in Figure 4.14a and b. We also considered the case of double stage with stripper cascade; however, our preliminary analysis showed that the enricher cascade allows to cut down the membrane area and power consumption for the target CO₂ recovery and purity. Therefore, only the double-stage process with an enricher cascade has been taken into account for comparison with the single-stage process.

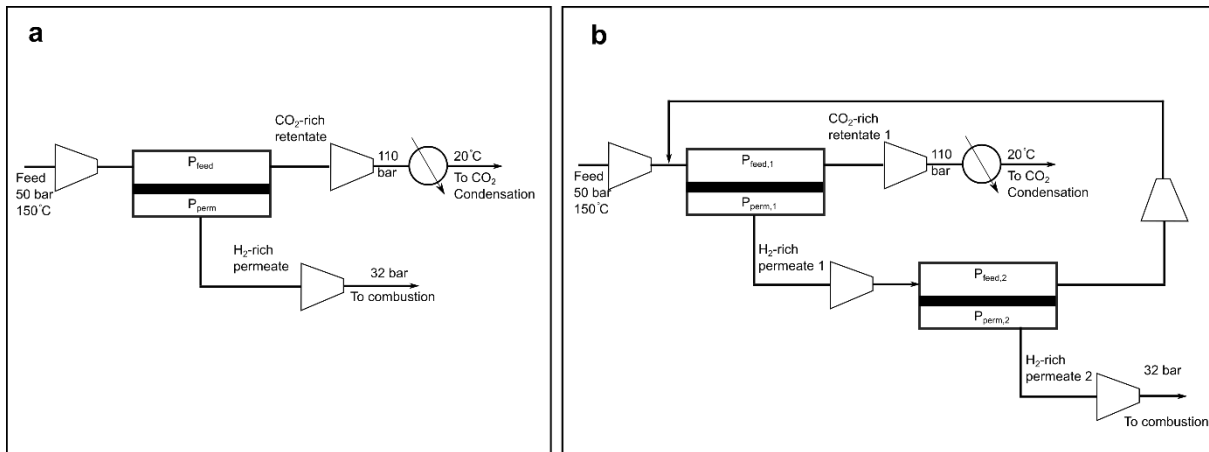


Figure 4.14. a) Single stage and b) Double stage membrane with enricher cascade for the techno-economic analysis for the Integrated Gasification Combined Cycle (IGCC) processes.

Table 4.1 lists the key findings of the analysis for both the single- and double-stage processes. Briefly, H₂ and CO₂ recoveries close to or higher than 70% could be obtained with the single stage. These are increased to 80% with the double stage. The biggest advantage of using the NPC membranes is reflected by the fact that a very small membrane area is required for the process (specific area of 0.0135 and 0.076 m² kgCO₂⁻¹ s⁻¹ for single stage and double stage, respectively). As a result, while the literature reports total membrane area in the order of 20000 m² for state-of-the-art membranes H₂ permeance of 300 GPU^{78,223} for producing 0.5 million tons of H₂-rich permeate per annum, in our case, the total area is only of the order of 10 m². This is extremely attractive to cut down the capital cost and reduce the size of the capture unit. This makes it interesting to deploy these membranes for H₂ separation where the footprint is a critical issue. Moreover, it makes it easier to scale-up the membrane for large-scale processes because the needed membrane area is extremely low.

We note that a lower selectivity from NPC membrane in comparison with polymeric membranes (H₂/CO₂ selectivity in the range of 6-15) leads to a lower purity of the H₂ and CO₂ streams in the single stage. The purities are improved in the case of double stage; however, it leads to a higher power consumption as the required flow rate of the recycled stream increases. As a result, the LCOE increase changes from 14.5% for the single stage to 36.7% for the double stage. In comparison, the LCOE increase from the Selexol process is estimated to be 31%.¹⁸⁶ Yet, as mentioned above, these membranes can be attractive when the footprint is an issue, e.g., separation processes in ocean or space

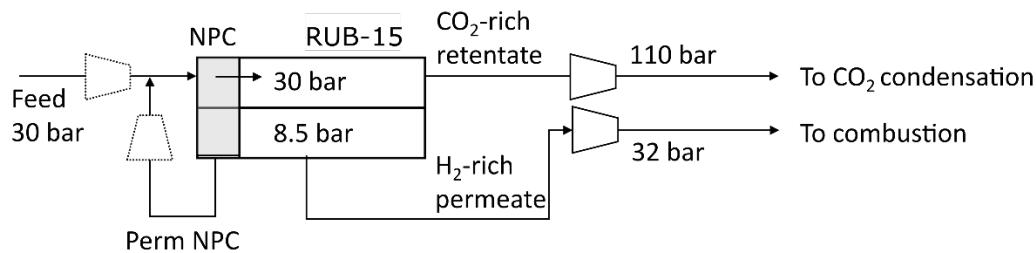
Table 4.1. Table reporting the comparison between the single and double configurations.

	Single stage $P_{\text{feed}} = 50 \text{ bar}$, $P_{\text{perm}} = 8.5 \text{ bar}$	Double stage $P_{\text{feed},1} = 50 \text{ bar}$, $P_{\text{perm},1} = 11 \text{ bar}$ $P_{\text{feed},2} = 20 \text{ bar}$, $P_{\text{perm},2} = 11 \text{ bar}$
Spec. area [$\text{m}^2 \text{ kg}^{-1} \text{ CO}_2 \text{ s}^{-1}$]	0.0135	0.076
Recovery CO_2 [-]	0.69	0.81
Purity CO_2 [-]	0.64	0.75
Recovery H_2 [-]	0.74	0.82
Purity H_2 [-]	0.78	0.87
Total power [MW_{el}]	34.0	75.2
CO_2 cost [$\$/\text{ton}$]	5.7	11.8
LCOE increase [%]	14.5	36.7

To achieve higher CO_2 recovery and H_2 purity, we coupled RUB-15 membranes in two different configurations, as reported in Figure 4.15. The first one (Figure 4.15a) employs a single stage that combines both NPC and RUB-15 membranes, while the second configuration (Figure 4.15b) uses two different stages where the first one is NPC membrane and the second is RUB-15. The permeate from the RUB-15 stage is recycled back to the NPC stage.

When a single stage was employed, targeted purity and recovery of hydrogen were achievable (Table 4.2); however, the minimization of the objective cost function was finding its minimum when the NPC area was tending to zero. This behavior is understandable since, at any increase of NPC area, the purity in the permeate was dropping dramatically due to the lower selectivity on NPC compared to RUB-15 membranes. Attempts to tackle this issue were performed by recycling the permeate in the NPC section, but no significant change was observed because all the separation duties were carried on by the RUB-15 section.

a



b

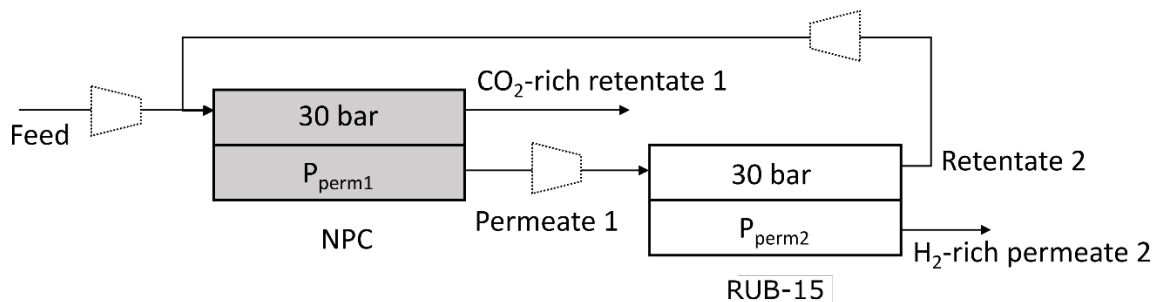


Figure 4.15. a) NPC and RUB-15 membranes combined in a single-stage configuration. b) NPC and RUB-15 membranes combined in a two-stage configuration with recycling of permeate from the second stage to the feed of stage 1.

Table 4.2. Data are relative to single-stage configuration with NPC and RUB-15 membranes.

	NPC + RUB-15
Spec. area [$\text{m}^2 \text{kg}^{-1} \text{CO}_2 \text{s}^{-1}$]	470
Recovery CO_2 [-]	0.88
Purity CO_2 [-]	0.83
Recovery H_2 [-]	0.88
Purity H_2 [-]	0.92
Total power [MW]	67.4
CO_2 cost [\$/ton]	9.1
LCOE increase [%]	31.1

For the double-stage configuration, two operating conditions were explored, with the permeates pressure having the same values of 13 bar (Table 4.3 third column) and different values (Table 4.3 second column) with the aim of achieving CO_2 recovery and H_2 purity of 90%. When the permeate pressure was equal, the driving force across the membrane was lower compared to the case with different permeate pressure. The lower driving force resulted in recoveries and purities below the target value; on the other hand, when the driving force was increased, both recovery and purity of 90% were achieved. However, a higher increase in LCOE was observed, up to 40.3%.

Table 4.3. Data are relative to double-stage configuration with NPC and RUB-15 membranes.

	$P_{\text{perm1}}=7, P_{\text{perm2}}=10$ bar	$P_{\text{perm1}}=P_{\text{perm2}}=13$ bar
Spec. area [$\text{m}^2 \text{kg}^{-1} \text{CO}_2 \text{s}^{-1}$]	434	743
Recovery CO_2 [-]	0.9	0.85
Purity CO_2 [-]	0.85	0.74
Recovery H_2 [-]	0.9	0.8
Purity H_2 [-]	0.93	0.89
Compr. – cooling power [MW]	81.9 – 3.3	54.7 – 3.5
CO_2 cost without – with cooling [\$/ton]	10.6 – 11.0	8.4 – 8.8
LCOE increase without – with cooling [%]	38.6 – 40.3	26.0 – 27.6

4. Conclusions

Overall, we report a detailed characterization of NPC membranes and show that they are extremely attractive for ultrafast transport of gases and can be useful for pre-combustion capture and hydrogen production, especially where a small membrane footprint is highly desirable. The rapid transport is attributed to Knudsen diffusion mechanism through the perforated lamellar nanostructure of the NPC film, originating from the phase separation of PS-*b*-P4VP hydrogen-bonded with turanose. Because of its chemical and thermal robustness, a smooth surface, and small pore opening (20 nm) at the top surface, the NPC film is also attractive as high-flux support for the fabrication of ultrathin membranes. These properties also make NPC film a top choice for the mechanical reinforcement for high permeance two-dimensional membranes such as those made of nanoporous single-layer graphene.

Chapter 5: Summary and perspective

1. Summary of the thesis

Climate change and resource scarcity are clear signs that a fundamental change is needed in the production process of any type of commodity. While it is well-acknowledged the importance of developing low-energy alternatives to thermally-driven processes, advancements in low energy-separation technologies are highly dependent on the existence of suitable and performing materials. Zeolites have shown tremendous advancement in the catalysis field, dominating the market in recent years (15% market share).⁷⁹ In contrast, only a few industrial applications in the dehydration of organic solvents have seen zeolites flourish as membranes.^{81,82} Two-dimensional zeolite-based membranes are extremely attractive for industrial separations since 1) they possess ordered nanopores that allow for high purities, 2) they can be assembled into very thin films that increase the productivity, and 3) they are thermally and mechanically stable under harsh operating conditions.

However, the synthesis of cost-effective zeolitic membranes capable of yielding high-performance separations and that possess essential industrial features such as scalability and reproducibility are still a grand challenge. The major bottlenecks that have limited the commercialization of zeolite membranes for gas separation are:

- i) *Fabrication method.* The synthesis of high-performance zeolite membranes is generally obtained using a seeded secondary growth, where small crystals of the aimed zeolite are carefully deposited onto a porous support and hydrothermally re-grown to fill the gaps between the crystals. The secondary growth process is hard to control and presents reproducibility issues. The only strategy available to minimize the defects generated within the membrane is the fabrication of thicker films at the expense of low productivity and higher manufacturing costs.
- ii) *Cost of the support.* Up to 90% of the zeolite membrane cost is represented by the underlying inorganic support.^{27,83,172} Expensive and difficult to process ceramics and metals are generally used for supporting thin zeolite films.⁸³ Moreover, the fragile nature of inorganic support represents many technical and engineering challenges for the scale-up.

While a plethora of excellent reports on a lab-scale has demonstrated the potential of zeolite membranes in the gas separation field, their spread to the industrial scale has been hampered by the listed challenges.

In this thesis, we have identified H_2/CO_2 separation, which plays a central role in the industry (pre-combustion capture, membrane reactor in water-gas shift reaction, etc.) and could grant zeolite membranes a window of opportunity where the polymeric membranes cannot be used because the operating conditions are too harsh for the majority of polymers. Yet, the synthesis of zeolitic films capable of H_2/CO_2 separation for high-temperature applications remains a grand challenge.^{92,249} Zeolite frameworks possessing 6-MRs of SiO_4 tetrahedra (e.g., sodalite) have the potential to sieve H_2 from CO_2 due to the appropriate gap in the 6-MRs, which falls between the kinetic diameters of H_2 and CO_2 .^{92,99,100} However, membranes based on 6-MRs of sodalite framework for gas separation have not been reported yet. The main reason is that during the synthesis of sodalite films, the organic structure-directing agent (OSDA) gets trapped in the sodalite cage, and attempts to remove the OSDA tend to collapse the structure.^{107,108}

The tremendous potential of the sodalite framework, along with the scarcity of literature data exploiting the 6-MR for H_2/CO_2 separation, stimulated us to address this challenge. In this thesis, we circumvented these issues and were able to avoid the tedious hydrothermal synthesis (secondary growth) route by starting from the layered precursor of sodalite. Ultrathin zeolitic membranes were developed by first synthesizing 0.8-nm-thick crystalline nanosheets from the sodalite precursor RUB-15. The isolation of layers allowed for the removal of the OSDA prior to the condensation of the nanosheets to form sodalite. This strategy allows the compact assembly of the layers by filtration effectively and rendering the OSDA-free SOD framework available for H_2/CO_2 separation for the first time. The proposed strategy was secondary-growth-free and highly reproducible.

RUB-15 is a hydrous layered silicate composed of chains of 4-MRs of SiO_4 tetrahedra that connect to form 6-MRs windows. The layered form of RUB-15 was hydrothermally synthesized. The OSDA could be easily replaced by a cationic surfactant which enlarged the d spacing of the layers from 14 to 30 Å facilitating the subsequent exfoliation process. A low-molecular-weight polymer was intercalated between the layers, and the external application of shear stress via melt-compounding technique exfoliated RUB-15 layers into single layers. Our efforts contributed to expanding the limited library of exfoliated zeolitic nanosheets since this was the first report of the exfoliation of the sodalite precursor.

Well-dispersed and stable suspension of RUB-15 nanosheets was obtained in an environmentally friendly solvent, which allowed for the fabrication of ultrathin (300 nm) membranes onto porous supports. Detailed transport study of the as-filtered membranes revealed the presence of two different pathways: (i) through 6-MRs and (ii) through the intersheet galleries. The latter dominated the transport and yielded a molecular cut-off of 3.6 Å with H₂/N₂ and H₂/CH₄ selectivities above 20.

The intersheet gallery spacing was diminished by condensation of the terminal silanol groups present in the RUB-15 nanosheets. Upon calcination, defective [SiO₃][O⁻] units were converted into silicon tetrahedra [SiO₄], eliminating the interlayer transport pathway. Attractive H₂/CO₂ selectivities (above 100) demonstrated an effective suppression of the interlayer transport and highlighted the H₂-selective nature of 6-MRs in the temperature range of 25-300 °C. Overall, this represented the first report of high-performance two-dimensional zeolitic membranes without resorting to the secondary growth process and able to efficiently sieve light gases. Chemically and thermally robust RUB-15 films are likely to find application in pre-combustion carbon capture, as the selective layer in the catalytic membrane reactors for the water–gas shift reaction, as well as the protective overlayer for palladium membranes. Our work lays a strong foundation in the formation of secondary growth-free zeolitic membranes and could be applied to a wide range of layered zeolite frameworks (MWW, MFI, NSI, UTL, RWR, etc.).

With regard to the support challenge, we have identified in polymers a potential solution for zeolite membranes. Polymeric supports are cheap, easily scalable, and could be engineered into suitable configurations (spiral wound, hollow fibers, etc.) based on the required separation criteria. However, polymeric materials cannot withstand the high temperatures and the oxidative atmospheres (required for most of the zeolite frameworks) for the detemplation process needed to free the zeolitic pores from the OSDA. High-temperature stable polymers such as polybenzimidazole are promising candidates to fabricate supports for zeolite membranes. However, their thermal stability, although high for polymeric standards, is not sufficient to sustain the current detemplation processes, which typically require temperatures of ~500 °C. The development of a milder detemplation process is imperative to enable the use of high-temperature polymers as supports. In line with this challenge, we have developed a new PBI-based support from commercially available PBI-AM FUMION[®] using the NIPS process on a commercial stainless steel mesh. PBI-AM overcomes many of the challenges faced by the conventional PBI, such as high degrees of shrinkage, problematic dissolution into organic solvents, and short-term stability of the dope solutions. To the best of our knowledge, this represents the first report of a polymeric

membrane made by NIPS using PBI-AM polymer. The quality of the support in terms of narrow and uniform pores (20 nm), smooth surface, low-transport resistance, thermal, chemical and mechanical stability, and ease of processing could span its use over other membrane-based materials. The maximum temperature at which the support could be used safely was 330 °C. This was still too low to be used in combination with the RUB-15 membranes, which are typically calcined at 500 °C. To overcome this, we fabricated thin RUB-15 films on the PBI-AM support and developed a milder calcination temperature at 330 °C for 8 h, which was sufficient to remove the occluded organic molecules and convert defective silanol nests into silicon tetrahedra [SiO₄], yielding membranes with H₂/CO₂ in the range of 20-35 and permeances up to 400 GPU in the temperature range of 25-250 °C.

To completely avoid the calcination procedure for the nanosheets detemplation, we employed a room-temperature, liquid-extraction-based detemplation method, where diluted solutions of acetic acid in ethanol were directly filtered on a preformed film to remove the occluded organic molecules. First, nanosheets dispersed in toluene were filtered on the polymeric PBI-AM support, and subsequently, the acidic solution was filtered on top. XRD investigation demonstrated the successful removal of the surfactant CTAB and the decrease of the interlayer spacing to 8 Å, which was equivalent to the thickness of the nanosheet. Preliminary results on gas separation performance displayed attractive H₂/CO₂ selectivities up to 15 and permeance up to 300 GPU.

In the final part of the thesis, we highlighted the importance of membrane process simulation, which should serve as a guideline in the development of specific membrane performance. We explored the use of a carbon-based membrane that possessed over 2 million GPU of H₂ permeance and a H₂/CO₂ Knudsen selectivity for pre-combustion capture in different configurations and in combination with RUB-15 membranes. The nanoporous carbon (NPC) membrane was fabricated by the pyrolysis of phase-separated block-copolymer/turanose film coated on a sacrificial support. The pyrolysis generated a 100 nm-thick film with high porosity and average pore size of 22 nm and could be tested in the temperature range of 25-300 °C. Techno-economic analysis of the NPC membranes in the pre-combustion capture with a two-stages membrane configuration yielded extremely low specific areas for H₂ purification, which can significantly cut down the footprint of the separation process and the associated capital cost. At the same time, the coupling with RUB-15 membranes allowed the achievement of the targeted purity and recovery, albeit at a higher LCOE increase. The great potential of the NPC membrane has also found extensive application in the single-layer graphene transfer, acting as a mechanical reinforcement for the graphene layer.

2. Perspective

This thesis dealt with membrane-based gas separation by investigating the major key aspects such as the sieving material (top layer composed of RUB-15 nanosheets), the underlying support (bottom layer represented by PBI-AM polymer), and the process simulation to identify suitable operating conditions and the optimal membrane configurations.

Large scale synthesis of zeolite membranes: Although we have provided tools to tackle each of the weak aspects in zeolite membranes helping to bring their commercialization one step closer, many efforts are still needed to bring their development to a real industrial scale. Successful centimeter-scale membranes were reported on a lab scale; however, they are still far from the meter-scale needed for industrial applications. In addition, their performances have to be evaluated under real operating conditions where traces of other components (H_2S , CO , etc.) and high pressure might compromise the lab-demonstrated performance.

The synthesis of inorganic membranes on a large scale is very challenging because the presence of defects within the membrane is inevitable. At the same time, we should remember that the first polymeric membrane commercialized for gas separation (PRISM) used a defect-sealing layer to clog inevitable defects. The use of a rubber layer on the inorganic membrane could compromise their advantage of higher flux. In this thesis, we suggested a refiltering process where defects were selectively blocked by the same nanosheets zeolitic phase without affecting the flux of the non-defective regions.

Hollow fiber configuration: The developed polymeric support had high porosity and flux, smooth surface, ease of scalability, and thermal and mechanical stability, which make it ideal for many membranes-based materials. In our work, it was used in a flat-sheet configuration. However, for industrial applications, where high-pressures are used, a hollow-fiber configuration is highly desired. Thanks to the filtration-based fabrication method of RUB-15 membranes, the preparation on a curved surface should not represent a major hurdle.

The ultimate zeolite membrane: The use of crystalline building blocks for membrane fabrication gives a higher degree of freedom compared to *in-situ* crystallized films. The rational tuning of the membrane thickness can be achieved by adjusting the solution concentration or by using a layer-

by-layer deposition. The latter is extremely convenient when the deposition of a single layer of nanosheets is required.⁵¹

Figure 5.1 shows a preliminary result that was obtained using Langmuir-Schaefer deposition of 10 layers of RUB-15 nanosheets.

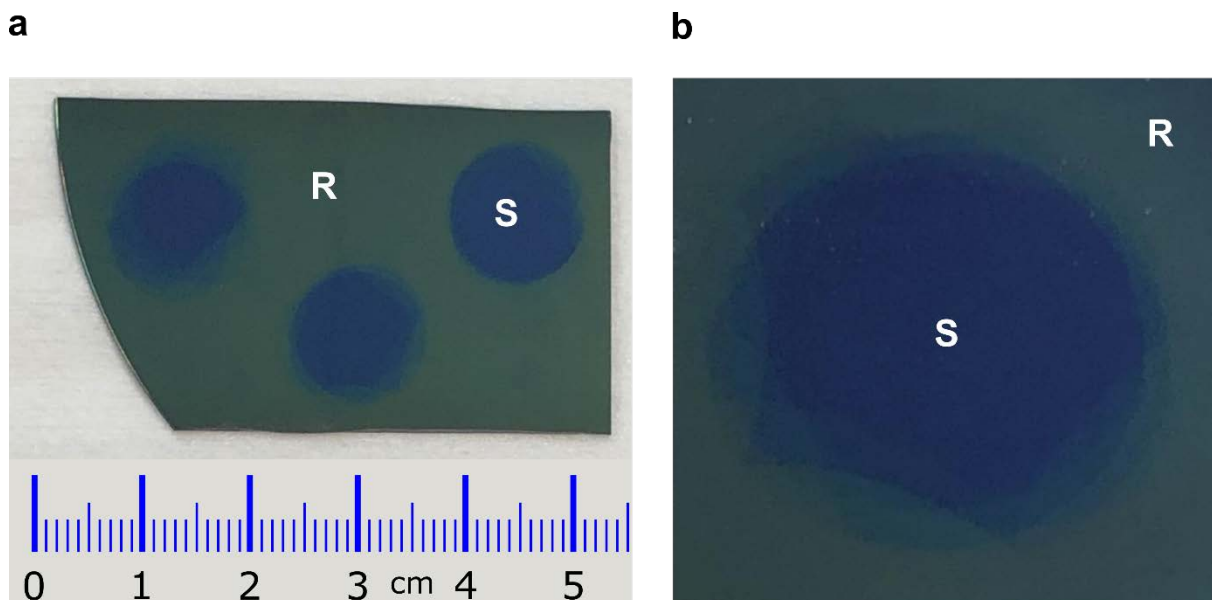


Figure 5.1. a) Photographs of Layer-by-layer deposition of RUB-15 nanosheets on a silicon wafer. b) Zoom of the central disc in (a). R and S letters indicate the region with RUB-15 coverage and bare silicon wafer, respectively.

The yellowish region (indicated by R) is composed of ten layers of RUB-15, while the blue region (indicated by S) is the bare silicon wafer support. The difference in color between blue and yellowish was obtained by using geometrically irregular masks that after each deposition were rotated. The different gradients in colors at the boundary between R and S region highlight the different deposited layers. The SEM image of the deposited nanosheets (image taken after 3 layers deposition) of Figure 5.1 is shown in Figure 5.2.

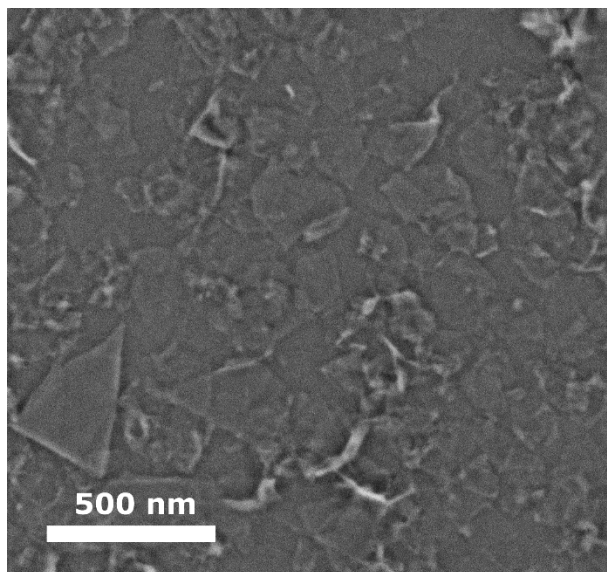


Figure 5.2. SEM image of RUB-15 nanosheets deposited *via* Langmuir-Schaefer on a silicon wafer.

Future optimization work on layer-by-layer deposition could enable the synthesis of sub-10 nm membranes resulting in an order of magnitude higher permeance compared to the present work. On the other hand, thinner films would be more affected by the presence of defects; hence, extra care needs to be given to solution preparation and deposition environment, which should be dust-free.

Optimization of the fabrication process: Zeolitic nanosheets-based membranes require a long processing time and tens of steps to obtain the final solution with dispersed nanosheets. A time- and energy-consuming step is the centrifugation-based purification that occurs at 40000 g-force for 3 h to isolate the nanosheets from the polystyrene matrix (Figure 1.12). For the potential scale-up, centrifugation might represent a hurdle in the processing chain, and the development of other purification-based methods is highly encouraged.

A promising route that seemed to be successful from preliminary results is the use of a dialysis-based purification. RUB-15 nanosheets are embedded in the polystyrene matrix and dispersed in toluene, where the polystyrene is dissolved. The hydraulic diameter of the polymer is orders of magnitude smaller than the average size of the nanosheets, which could freely diffuse through a 100 nm porous membrane. By employing a system as in Figure 5.3a-c, we could continuously wash away the polystyrene as shown by the UV-Vis, where the peak characteristic of polystyrene (294 nm) decreased continuously with time. This method yielded well-dispersed nanosheets in toluene. This new process, together with the new detemplation method that uses extraction rather than the preliminary acid treatment on the nanosheets followed by calcination, could drastically cut down

the processing time and energy and the number of steps to reach the final filtration-based fabrication step.

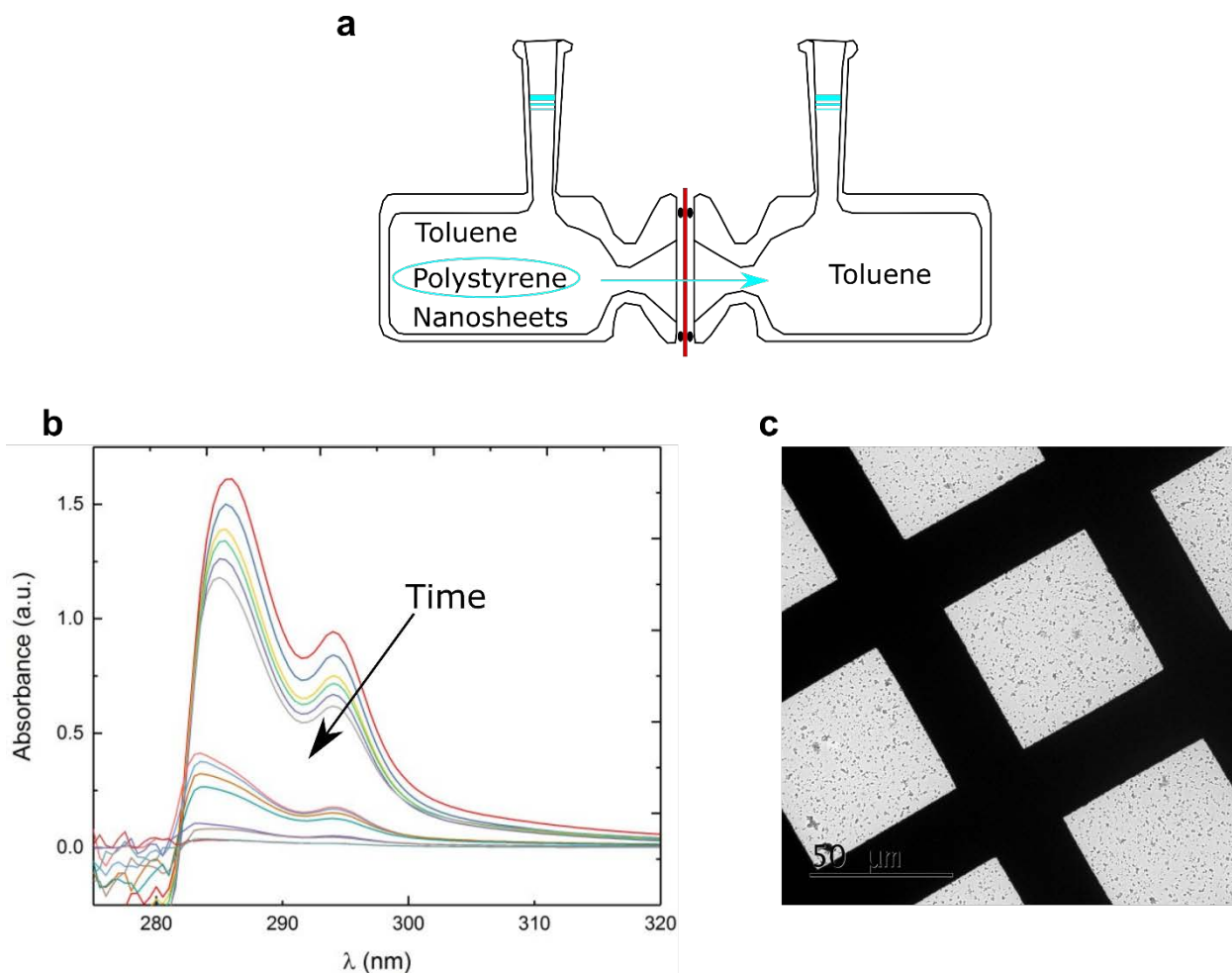


Figure 5.3. a) Diffusion cell for RUB-15 nanosheets purification from the polymeric matrix using AAO membrane with pores of 100 nm. b) UV-Vis experiment on the solution containing toluene, polymer, and nanosheets showing the gradual decrease to ca. zero of the polymer concentration. c) TEM image of the purified nanosheets highlighting their good dispersion.

Other promising applications for RUB-15 membranes: Besides membrane-based applications, RUB-15 nanosheets could be potentially used in catalysis and adsorption. Layered (unexfoliated) RUB-15 was previously used as a support for the loading of various metal nanoparticles displaying their excellent catalytic activity.^{250,251} In adsorption, layered RUB-15 was employed for the remediation of water streams containing radionuclides and heavy metals.²⁵² Since both adsorption and heterogeneous catalysis are highly affected by the exposed surface area, the employment of exfoliated RUB-15 nanosheets would grant access to a higher population of active/adsorption sites.

Recently, a relatively new concept in catalysis looks at the increase of catalytic reaction rate constants by engineering the chemical environment around the catalytic site rather than focusing

on the catalytic site itself. Higher orders of magnitude in constant rates could be achieved by engineering hydrophobic zeolitic pores in which the disruption of the order generated by a hydrophilic solvent could boost the energetics of adsorption and catalysis, yielding remarkable performance.^{253–255} Preliminary results of the layer-by-layer deposition showed that RUB-15 nanosheets could be deposited on a flat surface (Figure 5.1 and Figure 5.2), and this could be used to reproduce the order disruption created in a zeolite pore. RUB-15 nanosheets could be deposited on a flat surface on which a metal nanoparticle was previously deposited, and the van der Waals gap between the hydrophilic RUB-15 nanosheet and the substrate would allow the intercalation of a single layer of ordered hydrophobic solvents. When the thermal/electrochemical reaction has initiated, the disruption of the order of the hydrophobic solvent layer around the active site could generate a similar effect. A similar concept using other 2D layered materials has been successfully employed.^{256,257}

References

1. Elimelech, M. & Phillip, W. A. The future of seawater desalination: Energy, technology, and the environment. *Science* 333, 712–717 (2011).
2. ORNL,. *Materials for Separation Technologies. Energy and Emission Reduction Opportunities*. (2005). doi:10.2172/1218755
3. Kiss, A. A. Distillation technology - still young and full of breakthrough opportunities. *J. Chem. Technol. Biotechnol.* 89, 479–498 (2014).
4. Van Miltenburg, A., Zhu, W., Kapteijn, F. & Moulijn, J. A. Adsorptive separation of light olefin/paraffin mixtures. *Chem. Eng. Res. Des.* (2006). doi:10.1205/cherd05021
5. AIChE, F. N.-A. I. of C. E. & 2001. New challenges and innovations in separations technology.
6. Dutta, B. K. Principles of mass transfer and separation processes. *Can. J. Chem. Eng.* 87, 818–819 (2009).
7. Park, H. B., Kamcev, J., Robeson, L. M., Elimelech, M. & Freeman, B. D. Maximizing the right stuff: The trade-off between membrane permeability and selectivity. *Science*, 356, eaab0530 (2017).
8. Sholl, D. S. & Lively, R. P. Seven chemical separations to change the world. *Nature* 532, 435–437 (2016).
9. Service, R. F. Desalination Freshens Up. *Science*, 313, 1088–1090 (2006).
10. Strathmann, H. Membrane separation processes: Current relevance and future opportunities. *AIChE J.* 47, 1077–1087 (2001).
11. Li, X. & Li, J. Fluxes and Driving Forces in Membrane Separation Processes. in *Encyclopedia of Membranes* 1–3 (Springer Berlin Heidelberg, 2015). doi:10.1007/978-3-642-40872-4_2197-1
12. Micari, M., Dakhchoune, M. & Agrawal, K. V. Techno-economic assessment of postcombustion carbon capture using high-performance nanoporous single-layer graphene membranes. *J. Memb. Sci.* 624, 119103 (2021).
13. Loeb, S. & Sourirajan, S. Sea Water Demineralization by Means of an Osmotic Membrane. in 117–132 (1963). doi:10.1021/ba-1963-0038.ch009
14. Henis, J. M. S. & Tripodi, M. K. A novel approach to gas separations using composite hollow fiber membranes. *Sep. Sci. Technol.* 15, 1059–1068 (1980).
15. Henis, J. M. S. & Tripodi, M. K. Composite hollow fiber membranes for gas separation: the resistance model approach. *J. Memb. Sci.* 8, 233–246 (1981).
16. Baker, R. W. & Low, B. T. Gas separation membrane materials: A perspective. *Macromolecules* 47, 6999–7013 (2014).

17. Lin, Y. S. Inorganic Membranes for Process Intensification: Challenges and Perspective. *Ind. Eng. Chem. Res.* 58, 5787–5796 (2019).
18. Lin, Y. S. Inorganic Membranes for Process Intensification: Challenges and Perspective. *Ind. Eng. Chem. Res.* 58, 5787–5796 (2019).
19. Caro, J. Hierarchy in inorganic membranes. *Chem. Soc. Rev* 45, 3468 (2016).
20. Ghosal, K. & Freeman, B. D. Gas separation using polymer membranes: an overview. *Polym. Adv. Technol.* 5, 673–697 (1994).
21. Luo, S. *et al.* Highly Selective and Permeable Microporous Polymer Membranes for Hydrogen Purification and CO₂ Removal from Natural Gas. *Chem. Mater.* 30, 5322–5332 (2018).
22. Galizia, M. *et al.* 50th Anniversary Perspective : Polymers and Mixed Matrix Membranes for Gas and Vapor Separation: A Review and Prospective Opportunities. *Macromolecules* 50, 7809–7843 (2017).
23. Robeson, L. M. The upper bound revisited. *J. Memb. Sci.* 320, 390–400 (2008).
24. Li, S., Falconer, J. L. & Noble, R. D. SAPO-34 membranes for CO₂/CH₄ separation. *J. Memb. Sci.* 241, 121–135 (2004).
25. Lin, Y. S., Kumakiri, I., Nair, B. N. & Alsyouri, H. Microporous inorganic membranes. *Sep. Purif. Methods* 31, 229–379 (2002).
26. Burggraaf, A. J. & Cot, L. Fundamentals of inorganic membrane science and technology. *Membr. Sci. Technol.* 4, 3 (1996).
27. Kosinov, N., Gascon, J., Kapteijn, F. & Hensen, E. J. M. Recent developments in zeolite membranes for gas separation. *J. Memb. Sci.* 499, 65–79 (2016).
28. Novoselov, K. S. *et al.* Electric field in atomically thin carbon films. *Science*, 306, 666–669 (2004).
29. Koenig, S. P., Wang, L., Pellegrino, J. & Bunch, J. S. Selective molecular sieving through porous graphene. *Nat. Nanotechnol.* 7, 728–732 (2012).
30. Li, H. *et al.* Ultrathin, molecular-sieving graphene oxide membranes for selective hydrogen separation. *Science*, 342, 95–98 (2013).
31. Ding, L. *et al.* MXene molecular sieving membranes for highly efficient gas separation. *Nat. Commun.* 9, 1–7 (2018).
32. Grayfer, E. D., Kozlova, M. N. & Fedorov, V. E. Colloidal 2D nanosheets of MoS₂ and other transition metal dichalcogenides through liquid-phase exfoliation. *Advances in Colloid and Interface Science* 245, 40–61 (2017).
33. Liu, Y., Wang, N., Cao, Z. & Caro, J. Molecular sieving through interlayer galleries. *J. Mater. Chem. A* 2, 1235–1238 (2014).
34. Huang, S. *et al.* Single-layer graphene membranes by crack-free transfer for gas mixture

- separation. *Nat. Commun.* 9, 1–11 (2018).
35. Varoon, K. *et al.* Dispersible Exfoliated Zeolite Nanosheets and Their Application as a Selective Membrane. *Science*, 334, 72–75 (2011).
 36. Peng, Y. *et al.* Metal-organic framework nanosheets as building blocks for molecular sieving membranes. *Science*, 346, 1356–1359 (2014).
 37. Côté, A. P. *et al.* Chemistry: Porous, crystalline, covalent organic frameworks. *Science*, 310, 1166–1170 (2005).
 38. Villalobos, L. F. *et al.* Large-scale synthesis of crystalline g-C₃N₄ nanosheets and high-temperature H₂ sieving from assembled films. *Sci. Adv.* 6, eaay9851 (2020).
 39. Li, G., Zhang, K. & Tsuru, T. Two-Dimensional Covalent Organic Framework (COF) Membranes Fabricated via the Assembly of Exfoliated COF Nanosheets. *ACS Appl. Mater. Interfaces* 9, 8433–8436 (2017).
 40. Wang, X. *et al.* Reversed thermo-switchable molecular sieving membranes composed of two-dimensional metal-organic nanosheets for gas separation. *Nat. Commun.* 8, 14460 (2017).
 41. Li, P. Z., Maeda, Y. & Xu, Q. Top-down fabrication of crystalline metal-organic framework nanosheets. *Chem. Commun.* 47, 8436–8438 (2011).
 42. Rodenas, T. *et al.* Metal-organic framework nanosheets in polymer composite materials for gas separation. *Nat. Mater.* 14, 48–55 (2015).
 43. Makiura, R. *et al.* Surface nano-architecture of a metal-organic framework. *Nat. Mater.* 9, 565–571 (2010).
 44. Chen, Z. *et al.* N, P, and S Codoped Graphene-Like Carbon Nanosheets for Ultrafast Uranium (VI) Capture with High Capacity. *Adv. Sci.* 5, 1800235 (2018).
 45. Evans, A. M. *et al.* Seeded growth of single-crystal two-dimensional covalent organic frameworks. *Science*, 361, 52–57 (2018).
 46. Li, F. L. *et al.* Large-Scale, Bottom-Up Synthesis of Binary Metal-Organic Framework Nanosheets for Efficient Water Oxidation. *Angew. Chemie - Int. Ed.* 58, 7051–7056 (2019).
 47. Zheng, Q. *et al.* Transparent conductive films consisting of ultralarge graphene sheets produced by Langmuir-Blodgett assembly. *ACS Nano* 5, 6039–6051.
 48. Xia, S., Ni, M., Zhu, T., Zhao, Y. & Li, N. Ultrathin graphene oxide nanosheet membranes with various d-spacing assembled using the pressure-assisted filtration method for removing natural organic matter. *Desalination* 371, 78–87 (2015).
 49. Ibrahim, A. F. M. & Lin, Y. S. Synthesis of graphene oxide membranes on polyester substrate by spray coating for gas separation. *Chem. Eng. Sci.* 190, 312–319 (2018).
 50. Akbari, A. *et al.* Large-area graphene-based nanofiltration membranes by shear alignment of discotic nematic liquid crystals of graphene oxide. *Nat. Commun.* 7, 1–12 (2016).

51. Rangnekar, N. *et al.* 2D zeolite coatings: Langmuir-Schaefer deposition of 3 nm thick MFI zeolite nanosheets. *Angew. Chemie - Int. Ed.* 54, 6571–6575 (2015).
52. Peng, Y. *et al.* Metal-organic framework nanosheets as building blocks for molecular sieving membranes. *Science*, 346, 1356–1359 (2014).
53. Nair, R. R., Wu, H. A., Jayaram, P. N., Grigorieva, I. V. & Geim, A. K. Unimpeded permeation of water through helium-leak-tight graphene-based membranes. *Science*, 335, 442–444 (2012).
54. Zhou, F. *et al.* Ultrathin graphene oxide-based hollow fiber membranes with brush-like CO₂-philic agent for highly efficient CO₂ capture. *Nat. Commun.* 8, 1–8 (2017).
55. Tsapatsis, M. 2-dimensional zeolites. *AIChE J.* 60, 2374–2381 (2014).
56. Davis, M. E. Ordered porous materials for emerging applications. *Nature* 417, 813–821 (2002).
57. Caro, J., Noack, M. & Kölsch, P. Zeolite membranes: From the laboratory scale to technical applications. *Adsorption* 11, 215–227 (2005).
58. Wenten, I. G., Dharmawijaya, P. T., Aryanti, P. T. P., Mukti, R. R. & Khoiruddin. LTA zeolite membranes: Current progress and challenges in pervaporation. *RSC Advances* 7, 29520–29539 (2017).
59. Morigami, Y., Kondo, M., Abe, J., Kita, H. & Okamoto, K. The first large-scale pervaporation plant using tubular-type module with zeolite NaA membrane. *Sep. Purif. Technol.* 25, 251–260 (2001).
60. Choi, J. & Tsapatsis, M. MCM-22/silica selective flake nanocomposite membranes for hydrogen separations. *J. Am. Chem. Soc.* 132, 448–449 (2010).
61. Agrawal, K. V. *et al.* Oriented MFI membranes by gel-less secondary growth of sub-100 nm MFI-nanosheet seed layers. *Adv. Mater.* 27, 3243–3249 (2015).
62. Kim, D., Jeon, M. Y., Stottrup, B. L. & Tsapatsis, M. para-Xylene Ultra-selective Zeolite MFI Membranes Fabricated from Nanosheet Monolayers at the Air–Water Interface. *Angew. Chemie - Int. Ed.* 57, 480–485 (2018).
63. Jeon, M. Y. Synthesis of Zeolite Nanosheets and Applications in Membranes and Adsorption Separation Processes. (PhD dissertation, University of Minnesota, 2016).
64. Jeon, M. Y. *et al.* Ultra-selective high-flux membranes from directly synthesized zeolite nanosheets. *Nature* 543, 690–694 (2017).
65. Zhou, H. C., Long, J. R. & Yaghi, O. M. Introduction to metal-organic frameworks. *Chemical Reviews* 112, 673–674 (2012).
66. Cheetham, A. K., Rao, C. N. R. & Feller, R. K. Structural diversity and chemical trends in hybrid inorganic-organic framework materials. *Chemical Communications* 0, 4780–4795 (2006).
67. Li, Y., Liu, H., Wang, H., Qiu, J. & Zhang, X. GO-guided direct growth of highly oriented

- metal-organic framework nanosheet membranes for H₂/CO₂ separation. *Chem. Sci.* 9, 4132–4141 (2018).
68. Hummers, W. S. & Offeman, R. E. Preparation of Graphitic Oxide. *J. Am. Chem. Soc.* 80, 1339 (1958).
 69. Shen, J. *et al.* Subnanometer Two-Dimensional Graphene Oxide Channels for Ultrafast Gas Sieving. *ACS Nano* 10, 3398–3409 (2016).
 70. Bunch, J. S. *et al.* Impermeable atomic membranes from graphene sheets. *Nano Lett.* 8, 2458–2462 (2008).
 71. Paglieri, S. N. & Way, J. D. Innovations in palladium membrane research. *Separation and Purification Methods* 31, 1–169 (2002).
 72. Hu, L., Bui, V. T., Huang, L., Singh, R. P. & Lin, H. Facilely Cross-Linking Polybenzimidazole with Polycarboxylic Acids to Improve H₂/CO₂ Separation Performance. *ACS Appl. Mater. Interfaces* 13, 12521–12530 (2021).
 73. Zhu, L., Swihart, M. T. & Lin, H. Tightening polybenzimidazole (PBI) nanostructure via chemical cross-linking for membrane H₂/CO₂ separation. *J. Mater. Chem. A* 5, 19914–19923 (2017).
 74. Stevens, K. A. *et al.* Influence of temperature on gas transport properties of tetraaminodiphenylsulfone (TADPS) based polybenzimidazoles. *J. Memb. Sci.* 593, 117427 (2020).
 75. IEA (2019), The Future of Hydrogen, IEA, Paris <https://www.iea.org/reports/the-future-of-hydrogen>.
 76. Voldsund, M., Jordal, K. & Anantharaman, R. Hydrogen production with CO₂ capture. *Int. J. Hydrogen Energy* 41, 4969–4992 (2016).
 77. Ku, A. Y., Kulkarni, P., Shisler, R. & Wei, W. Membrane performance requirements for carbon dioxide capture using hydrogen-selective membranes in integrated gasification combined cycle (IGCC) power plants. *J. Memb. Sci.* 367, 233–239 (2011).
 78. Merkel, T. C., Zhou, M. & Baker, R. W. Carbon dioxide capture with membranes at an IGCC power plant. *J. Memb. Sci.* 389, 441–450 (2012).
 79. Mamudu, A., Emetere, M., Ishola, F. & Lawal, D. The Production of Zeolite Y Catalyst From Palm Kernel Shell for Fluid Catalytic Cracking Unit. *Int. J. Chem. Eng.* 2021, 1–8 (2021).
 80. Vermeiren, W. & Gilson, J. P. Impact of zeolites on the petroleum and petrochemical industry. *Top. Catal.* 52, 1131–1161 (2009).
 81. Wenten, I. G., Dharmawijaya, P. T., Aryanti, P. T. P., Mukti, R. R. & Khoiruddin. LTA zeolite membranes: Current progress and challenges in pervaporation. *RSC Advances* 7, 29520–29539 (2017).
 82. Morigami, Y., Kondo, M., Abe, J., Kita, H. & Okamoto, K. The first large-scale pervaporation plant using tubular-type module with zeolite NaA membrane. *Sep. Purif.*

- Technol.* 25, 251–260 (2001).
83. Gascon, J. *et al.* Practical approach to zeolitic membranes and coatings: State of the art, opportunities, barriers, and future perspectives. *Chem. Mater.* 24, 2829–2844 (2012).
 84. Suzuki, H. & 12-11, N. Composite membrane having a surface layer of an ultrathin film of cage-shaped zeolite and processes for production thereof.
 85. Lin, Y. S., Kumakiri, I., Nair, B. N. & Alsyouri, H. Microporous inorganic membranes. *Sep. Purif. Methods* 31, (2002).
 86. Jia, M. D., Chen, B., Noble, R. D. & Falconer, J. L. Ceramic-zeolite composite membranes and their application for separation of vapor/gas mixtures. *J. Memb. Sci.* 90, 1–10 (1994).
 87. Cussler, E. L. Membranes containing selective flakes. *J. Memb. Sci.* 52, 275–288 (1990).
 88. Agrawal, K. V. *et al.* Solution-processable exfoliated zeolite nanosheets purified by density gradient centrifugation. *AIChE J.* 59, 3458–3467 (2013).
 89. Zhang, H. *et al.* Open-Pore Two-Dimensional MFI Zeolite Nanosheets for the Fabrication of Hydrocarbon-Isomer-Selective Membranes on Porous Polymer Supports. *Angew. Chemie Int. Ed.* 55, 7184–7187 (2016).
 90. Kim, D., Jeon, M. Y., Stottrup, B. L. & Tsapatsis, M. *para*-Xylene Ultra-selective Zeolite MFI Membranes Fabricated from Nanosheet Monolayers at the Air-Water Interface. *Angew. Chemie Int. Ed.* 57, 480–485 (2018).
 91. Zhang, H. Fabrication of Zeolite MFI Membranes on Low Cost Polymer Supports. (PhD dissertation, University of Minnesota, 2017).
 92. Dakhchoune, M. *et al.* Gas-sieving zeolitic membranes fabricated by condensation of precursor nanosheets. *Nat. Mater.* 20, 362–369 (2021).
 93. Kirshna, R. Multicomponent surface diffusion of adsorbed species: a description based on the generalized Maxwell-Stefan equations. *Chem. Eng. Sci.* 45, 1779–1791 (1990).
 94. Bakker, W. J. W., Van Den Broeke, L. J. P., Kapteijn, F. & Moulijn, J. A. Temperature Dependence of One-Component Permeation through a Silicalite-1 Membrane. *AIChE J.* 43, 2203–2214 (1997).
 95. Korelskiy, D. *et al.* Efficient ceramic zeolite membranes for CO₂/H₂ separation. *J. Mater. Chem. A* 3, 12500–12506 (2015).
 96. Hong, M., Li, S., Falconer, J. L. & Noble, R. D. Hydrogen purification using a SAPO-34 membrane. *J. Memb. Sci.* 307, 277–283 (2008).
 97. Zito, P. F., Caravella, A., Brunetti, A., Drioli, E. & Barbieri, G. CO₂/H₂ Selectivity Prediction of NaY, DD3R, and Silicalite Zeolite Membranes. *Ind. Eng. Chem. Res.* 57, 11431–11438 (2018).
 98. Zito, P. F., Caravella, A., Brunetti, A., Drioli, E. & Barbieri, G. CO₂/H₂ Selectivity Prediction of NaY, DD3R, and Silicalite Zeolite Membranes. *Ind. Eng. Chem. Res.* 57, 11431–11438 (2018).

99. Van Den Berg, A. W. C. *et al.* Molecular-dynamics analysis of the diffusion of molecular hydrogen in all-silica sodalite. *J. Chem. Phys.* 120, 10285–10289 (2004).
100. van den Berg, A. W. C., Bromley, S. T., Flikkema, E. & Jansen, J. C. Effect of cation distribution on self-diffusion of molecular hydrogen in Na₃Al₃Si₃O₁₂ sodalite: A molecular dynamics study. *J. Chem. Phys.* 121, 10209–10216 (2004).
101. Khajavi, S., Jansen, J. C. & Kapteijn, F. Production of ultra pure water by desalination of seawater using a hydroxy sodalite membrane. *J. Memb. Sci.* 356, 52–57 (2010).
102. Khajavi, S., Kapteijn, F. & Jansen, J. C. Synthesis of thin defect-free hydroxy sodalite membranes: New candidate for activated water permeation. *J. Memb. Sci.* 299, 63–72 (2007).
103. Khajavi, S., Jansen, J. C. & Kapteijn, F. Application of hydroxy sodalite films as novel water selective membranes. *J. Memb. Sci.* 326, 153–160 (2009).
104. Wang, N., Liu, Y., Huang, A. & Caro, J. Supported SOD membrane with steam selectivity by a two-step repeated hydrothermal synthesis. *Microporous Mesoporous Mater.* 192, 8–13 (2014).
105. Khajavi, S., Jansen, J. C. & Kapteijn, F. Performance of hydroxy sodalite membranes as absolute water selective materials under acidic and basic conditions. *J. Memb. Sci.* 356, 1–6 (2010).
106. Xu, X. *et al.* Microwave-assisted hydrothermal synthesis of hydroxy-sodalite zeolite membrane. *Microporous Mesoporous Mater.* 75, 173–181 (2004).
107. Moteki, T., Chaikittisilp, W., Shimojima, A. & Okubo, T. Silica sodalite without occluded organic matters by topotactic conversion of lamellar precursor. *J. Am. Chem. Soc.* 130, 15780–15781 (2008).
108. Bibby, D. M. & Dale, M. P. Synthesis of silica-sodalite from non-aqueous systems. *Nature* 317, 157–158 (1985).
109. Oberhagemann, U., Bayat, P., Marler, B., Gies, H. & Rius, J. A Layer Silicate: Synthesis and Structure of the Zeolite Precursor RUB-15—[N(CH₃)₄]₈[Si₂₄O₅₂(OH)₄]·20 H₂O. *Angew. Chemie Int. Ed. English* 35, 2869–2872 (1996).
110. Moteki, T., Chaikittisilp, W., Sakamoto, Y., Shimojima, A. & Okubo, T. Role of acidic pretreatment of layered silicate RUB-15 in its topotactic conversion into pure silica sodalite. *Chem. Mater.* 23, 3564–3570 (2011).
111. Koike, M. *et al.* Topotactic conversion of layered silicate RUB-15 to silica sodalite through interlayer condensation in N-methylformamide. *Dalt. Trans.* 46, 10232–10239 (2017).
112. Woodcock, D. A. *et al.* Negative thermal expansion in the siliceous zeolites chabazite and ITQ-4: A neutron powder diffraction study. *Chem. Mater.* 11, 2508–2514 (1999).
113. Caro, J. & Noack, M. Zeolite membranes - Status and prospective. in *Advances in Nanoporous Materials* 1, 1–96 (Elsevier B.V., 2010).
114. Zhang, Y., Tokay, B., Funke, H. H., Falconer, J. L. & Noble, R. D. Template removal from

- SAPO-34 crystals and membranes. *J. Memb. Sci.* 363, 29–35 (2010).
115. Hu, L., Bui, V. T., Huang, L., Singh, R. P. & Lin, H. Facilely Cross-Linking Polybenzimidazole with Polycarboxylic Acids to Improve H₂/CO₂ Separation Performance. *ACS Appl. Mater. Interfaces* 13, 12521–12530 (2021).
 116. Li, Q., Amweg, M. L., Yee, C. K., Navrotsky, A. & Parikh, A. N. Photochemical template removal and spatial patterning of zeolite MFI thin films using UV/ozone treatment. *Microporous Mesoporous Mater.* 87, 45–51 (2005).
 117. Wang, L. *et al.* Preparation of defect-free DDR zeolite membranes by eliminating template with ozone at low temperature. *J. Memb. Sci.* 539, 152–160 (2017).
 118. Choi, J. *et al.* Grain boundary defect elimination in a zeolite membrane by rapid thermal processing. *Science* 325, 590–3 (2009).
 119. Lami, E. B., Fajula, F., Anglerot, D. & Des Courieres, T. Single step dealumination of zeolite beta precursors for the preparation of hydrophobic adsorbents. *Microporous Mater.* 1, 237–245 (1993).
 120. Severance, M. *et al.* Rapid crystallization of faujasitic zeolites: Mechanism and application to zeolite membrane growth on polymer supports. *Langmuir* 30, 6929–6937 (2014).
 121. Ge, Q., Wang, Z. & Yan, Y. High-performance zeolite NAA membranes on polymer-zeolite composite hollow fiber supports. *J. Am. Chem. Soc.* 131, 17056–17057 (2009).
 122. Xu, J. *et al.* Post-combustion CO₂ capture with membrane process: Practical membrane performance and appropriate pressure. *J. Memb. Sci.* 581, 195–213 (2019).
 123. Sablani, S., Goosen, M., Al-Belushi, R. & Wilf, M. Concentration polarization in ultrafiltration and reverse osmosis: A critical review. *Desalination* 141, 269–289 (2001).
 124. Gabrielli, P., Gazzani, M. & Mazzotti, M. On the optimal design of membrane-based gas separation processes. *J. Memb. Sci.* 526, 118–130 (2017).
 125. Rangnekar, N., Mittal, N., Elyassi, B., Caro, J. & Tsapatsis, M. Zeolite membranes - a review and comparison with MOFs. *Chem. Soc. Rev.* 44, 7128–7154 (2015).
 126. Yu, M., Noble, R. D. & Falconer, J. L. Zeolite Membranes: Microstructure Characterization and Permeation Mechanisms. *Acc. Chem. Res.* 44, 1196–1206 (2011).
 127. Pham, T. C. T., Kim, H. S. & Yoon, K. B. Growth of Uniformly Oriented Silica MFI and BEA Zeolite Films on Substrates. *Science*, 334, 1533–1538 (2011).
 128. Caro, J. & Noack, M. Zeolite membranes – Recent developments and progress. *Microporous Mesoporous Mater.* 115, 215–233 (2008).
 129. Hedlund, J. *et al.* High-flux MFI membranes. *Microporous Mesoporous Mater.* 52, 179–189 (2002).
 130. Ishikawa, A., Chiang, T. H. & Toda, F. Separation of water–alcohol mixtures by permeation through a zeolite membrane on porous glass. *J. Chem. Soc., Chem. Commun.* 764–765 (1989). doi:10.1039/C39890000764

131. Tosheva, L. & Valtchev, V. P. Nanozeolites: Synthesis, crystallization mechanism, and applications. *Chem. Mater.* 17, 2494–2513 (2005).
132. Corma, A., Fornes, V., Pergher, S. B., Maesen, T. L. M. & Buglass, J. G. Delaminated zeolite precursors as selective acidic catalysts. *Nature* 396, 353–356 (1998).
133. Choi, M. *et al.* Stable single-unit-cell nanosheets of zeolite MFI as active and long-lived catalysts. *Nature* 461, 246–249 (2009).
134. Ogino, I. *et al.* Delamination of Layered Zeolite Precursors under Mild Conditions: Synthesis of UCB-1 via Fluoride/Chloride Anion-Promoted Exfoliation. *J. Am. Chem. Soc.* 133, 3288–3291 (2011).
135. Zanardi, S. *et al.* Crystal structure determination of zeolite Nu-6(2) and its layered precursor Nu-6(1). *Angew. Chemie - Int. Ed.* 43, 4933–4937 (2004).
136. Roth, W. J. *et al.* A family of zeolites with controlled pore size prepared using a top-down method. *Nat. Chem.* 5, 628–633 (2013).
137. Cussler, E. L. Membranes containing selective flakes. *J. Memb. Sci.* 52, 275–288 (1990).
138. Liu, L. *et al.* Generation of subnanometric platinum with high stability during transformation of a 2D zeolite into 3D. *Nat. Mater.* 16, 132–138 (2017).
139. Mazur, M. *et al.* Synthesis of ‘unfeasible’ zeolites. *Nat. Chem.* 8, 58–62 (2016).
140. Zhang, X. Y. *et al.* Synthesis of self-pillared zeolite nanosheets by repetitive branching. *Science*, 336, 1684–1687 (2012).
141. Yuan, Z. *et al.* A Highly Ion-Selective Zeolite Flake Layer on Porous Membranes for Flow Battery Applications. *Angew. Chemie* 128, 3110–3114 (2016).
142. Chen, Z. *et al.* Nafion/zeolite nanocomposite membrane by in situ crystallization for a direct methanol fuel cell. *Chem. Mater.* 18, 5669–5675 (2006).
143. Choi, M. *et al.* Stable single-unit-cell nanosheets of zeolite MFI as active and long-lived catalysts. *Nature* 461, 246–249 (2009).
144. Sabnis, S. *et al.* Exfoliation of two-dimensional zeolites in liquid polybutadienes. *Chem. Commun.* 53, 7011–7014 (2017).
145. Corma, A., Diaz, U., Domine, M. E. & Fornes, V. AlITQ-6 and TiITQ-6: Synthesis, Characterization, and Catalytic Activity. *Angew. Chemie - Int. Ed.* 39, 1499–1501 (2000).
146. Ding, L. *et al.* A Two-Dimensional Lamellar Membrane: MXene Nanosheet Stacks. *Angew. Chemie Int. Ed.* 56, 1825–1829 (2017).
147. Wang, H., Dong, X. & Lin, Y. S. Highly stable bilayer MFI zeolite membranes for high temperature hydrogen separation. *J. Memb. Sci.* 450, 425–432 (2014).
148. Gu, X., Tang, Z. & Dong, J. On-stream modification of MFI zeolite membranes for enhancing hydrogen separation at high temperature. *Microporous Mesoporous Mater.* 111, 441–448 (2008).

149. Hong, Z. *et al.* Improvement of hydrogen-separating performance by on-stream catalytic cracking of silane over hollow fiber MFI zeolite membrane. *Int. J. Hydrogen Energy* 38, 8409–8414 (2013).
150. Karimi, S. *et al.* A simple method for blocking defects in zeolite membranes. *J. Memb. Sci.* 489, 270–274 (2015).
151. Pines, A., Gibby, M. G. & Waugh, J. S. Proton-enhanced NMR of dilute spins in solids. *J. Chem. Phys.* 59, 569–590 (1973).
152. Hartmann, S. R. & Hahn, E. L. Nuclear double resonance in the rotating frame. *Phys. Rev.* 128, 2042–2053 (1962).
153. Sindorf, D. W. & Maciel, G. E. ²⁹Si NMR Study of Dehydrated/Rehydrated Silica Gel Using Cross Polarization and Magic-Angle Spinning. *J. Am. Chem. Soc.* 105, 1487–1493 (1983).
154. Kopelevich, D. I. & Chang, H. C. Diffusion of inert gases in silica sodalite: Importance of lattice flexibility. *J. Chem. Phys.* 115, 9519–9527 (2001).
155. Giannozzi, P. *et al.* Quantum ESPRESSO: a modular and open-source software project for quantum simulations of materials. *J. Phys. Condens. Matter* 21, 395502 (2009).
156. Perdew, J. P., Burke, K. & Ernzerhof, M. Generalized gradient approximation made simple. *Phys. Rev. Lett.* 77, 3865–3868 (1996).
157. Grimme, S. Semiempirical GGA-type density functional constructed with a long-range dispersion correction. *J. Comput. Chem.* 27, 1787–1799 (2006).
158. Henkelman, G., Uberuaga, B. P. & Jónsson, H. Climbing image nudged elastic band method for finding saddle points and minimum energy paths. *J. Chem. Phys.* 113, 9901–9904 (2000).
159. Maheshwari, S. *et al.* Layer structure preservation during swelling, pillaring, and exfoliation of a zeolite precursor. *J. Am. Chem. Soc.* 130, 1507–1516 (2008).
160. Zhang, D. *et al.* Atomic-resolution transmission electron microscopy of electron beam-sensitive crystalline materials. *Science*, 679, eaao0865 (2018).
161. Zhu, Y. *et al.* Unravelling surface and interfacial structures of a metal-organic framework by transmission electron microscopy. *Nat. Mater.* 16, 532–536 (2017).
162. Aguiar, H., Serra, J., González, P. & León, B. Structural study of sol-gel silicate glasses by IR and Raman spectroscopies. *J. Non. Cryst. Solids* 355, 475–480 (2009).
163. Karimi, S. *et al.* A simple method for blocking defects in zeolite membranes. *J. Memb. Sci.* 489, 270–274 (2015).
164. Martínez Galeano, Y., Cornaglia, L. & Tarditi, A. M. NaA zeolite membranes synthesized on top of APTES-modified porous stainless steel substrates. *J. Memb. Sci.* 512, 93–103 (2016).
165. Liu, B. S. & Au, C. T. A La₂NiO₄-Zeolite Membrane Reactor for the CO₂ Reforming of Methane to Syngas. *Catal. Letters* 77, 67–74 (2001).

166. Günther, C., Richter, H. & Voigt, I. Zeolite membranes for hydrogen and water separation under harsh conditions. *Chem. Eng. Trans.* 32, 1963–1968 (2013).
167. Huang, A. & Caro, J. Steam-stable hydrophobic ITQ-29 molecular sieve membrane with H₂ selectivity prepared by secondary growth using Kryptofix 222 as SDA. *Chem. Commun.* 46, 7748 (2010).
168. Yuan, W., Wang, D. & Li, L. MFI-type zeolite membrane on hollow fiber substrate for hydrogen separation. *Chinese Sci. Bull.* 56, 2416–2418 (2011).
169. Huang, A. & Caro, J. Highly oriented, neutral and cation-free AlPO₄ LTA: from a seed crystal monolayer to a molecular sieve membrane. *Chem. Commun.* 47, 4201 (2011).
170. Zhang, S. *et al.* Penta-graphene: A new carbon allotrope. *Proc. Natl. Acad. Sci.* 112, 2372–2377 (2015).
171. Lin, Y. & Duke, M. C. Recent progress in polycrystalline zeolite membrane research. *Current Opinion in Chemical Engineering* 2, 209–216 (2013).
172. Caro, J. & Noack, M. Zeolite membranes - Status and prospective. in *Advances in Nanoporous Materials* 1, 1–96 (Elsevier B.V., 2010).
173. Villalobos, L. F., Hilke, R., Akhtar, F. H. & Peinemann, K.-V. Fabrication of Polybenzimidazole/Palladium Nanoparticles Hollow Fiber Membranes for Hydrogen Purification. *Adv. Energy Mater.* 8, 1701567 (2018).
174. Park, H. C. *et al.* Effect of solvent exchange on the morphology of asymmetric membranes. *Membrane Formation and Modification* 744, 110–124 (Oxford University Press, 1999).
175. Macdonald, W. & Pan, C. US3842515A - Method for drying water-wet membranes - Google Patents. (1973).
176. Yang, T., Shi, G. M. & Chung, T.-S. Symmetric and Asymmetric Zeolitic Imidazolate Frameworks (ZIFs)/Polybenzimidazole (PBI) Nanocomposite Membranes for Hydrogen Purification at High Temperatures. *Adv. Energy Mater.* 2, 1358–1367 (2012).
177. Villalobos, L. F., Hilke, R., Akhtar, F. H. & Peinemann, K.-V. Fabrication of Polybenzimidazole/Palladium Nanoparticles Hollow Fiber Membranes for Hydrogen Purification. *Adv. Energy Mater.* 8, 1701567 (2018).
178. Jeon, M. Y. *et al.* Ultra-selective high-flux membranes from directly synthesized zeolite nanosheets. *Nature* 543, 690–694 (2017).
179. Pesiri, D. R., Jorgensen, B. & Dye, R. C. Thermal optimization of polybenzimidazole meniscus membranes for the separation of hydrogen, methane, and carbon dioxide. *J. Memb. Sci.* 218, 11–18 (2003).
180. Powers, E. J. & Serad, G. A. History and development of polybenzimidazoles. in 355–373 (Elsevier, 1986). doi:10.1007/978-94-011-7073-4_34
181. Valtchev, V., Majano, G., Mintova, S. & Pérez-Ramírez, J. Tailored crystalline microporous materials by post-synthesis modification. *Chem. Soc. Rev.* 42, 263–290 (2013).

182. Jones, C. W., Tsuji, K., Takewaki, T., Beck, L. W. & Davis, M. E. Tailoring molecular sieve properties during SDA removal via solvent extraction. *Microporous Mesoporous Mater.* 48, 57–64 (2001).
183. Chung, T. S. & Xu, Z. L. Asymmetric hollow fiber membranes prepared from miscible polybenzimidazole and polyetherimide blends. *J. Memb. Sci.* 147, 35–47 (1998).
184. Hosseini, S. S., Teoh, M. M. & Chung, T. S. Hydrogen separation and purification in membranes of miscible polymer blends with interpenetration networks. *Polymer.* 49, 1594–1603 (2008).
185. Li, Z., Marler, B. & Gies, H. A new layered silicate with structural motives of silicate zeolites: Synthesis, crystals structure, and properties. *Chem. Mater.* 20, 1896–1901 (2008).
186. Merkel, T. C., Zhou, M. & Baker, R. W. Carbon dioxide capture with membranes at an IGCC power plant. *J. Memb. Sci.* 389, 441–450 (2012).
187. Martínez Galeano, Y., Cornaglia, L. & Tarditi, A. M. NaA zeolite membranes synthesized on top of APTES-modified porous stainless steel substrates. *J. Memb. Sci.* 512, 93–103 (2016).
188. Liu, B. S. & Au, C. T. A La₂NiO₄-zeolite membrane reactor for the CO₂ reforming of methane to syngas. *Catal. Letters* 77, 67–74 (2001).
189. Huang, A. & Caro, J. Highly oriented, neutral and cation-free AlPO₄ LTA: From a seed crystal monolayer to a molecular sieve membrane. *Chem. Commun.* 47, 4201–4203 (2011).
190. Stein, A., Wang, Z. & Fierke, M. A. Functionalization of porous carbon materials with designed pore architecture. *Advanced Materials* 21, 265–293 (2009).
191. Shiflett, M. B. & Foley, H. C. Ultrasonic deposition of high-selectivity nanoporous carbon membranes. *Science*, 285, 1902–1905 (1999).
192. Wu, M. S. & Lin, K. H. One-step electrophoretic deposition of Ni-decorated activated-carbon film as an electrode material for supercapacitors. *J. Phys. Chem. C* 114, 6190–6196 (2010).
193. Huang, S. *et al.* Ultrathin Carbon Molecular Sieve Films and Room-Temperature Oxygen Functionalization for Gas-Sieving. *ACS Appl. Mater. Interfaces* 11, 16729–16736 (2019).
194. Wang, J., Chen, Q., Renschler, C. L. & White, C. Ultrathin Porous Carbon Films as Amperometric Transducers for Biocatalytic Sensors. *Anal. Chem.* 66, 1988–1992 (1994).
195. Jones, C. W. & Koros, W. J. Carbon molecular sieve gas separation membranes-II. Regeneration following organic exposure. *Carbon*, 32, 1427–1432 (1994).
196. Shah, T. N., Foley, H. C. & Zydney, A. L. Development and characterization of nanoporous carbon membranes for protein ultrafiltration. *J. Memb. Sci.* 295, 40–49 (2007).
197. Mariwala, R. K. & Foley, H. C. Evolution of Ultramicroporous Adsorptive Structure in Poly(furfuryl alcohol)-Derived Carbogenic Molecular Sieves. *Ind. Eng. Chem. Res.* 33, 607–615 (1994).

198. Rungta, M. *et al.* Carbon molecular sieve structure development and membrane performance relationships. *Carbon*, 115, 237–248 (2017).
199. Koh, D. Y., McCool, B. A., Deckman, H. W. & Lively, R. P. Reverse osmosis molecular differentiation of organic liquids using carbon molecular sieve membranes. *Science*, 353, 804–807 (2016).
200. Sazali, N. A comprehensive review of carbon molecular sieve membranes for hydrogen production and purification. *International Journal of Advanced Manufacturing Technology* 107, 2465–2483 (2020).
201. Wenz, G. B. & Koros, W. J. Tuning carbon molecular sieves for natural gas separations: A diamine molecular approach. *AIChE J.* 63, 751–760 (2017).
202. Ma, Y. *et al.* Creation of Well-Defined “Mid-Sized” Micropores in Carbon Molecular Sieve Membranes. *Angew. Chemie* 131, 13393–13399 (2019).
203. Singh, R. & Koros, W. J. Carbon molecular sieve membrane performance tuning by dual temperature secondary oxygen doping (DTSOD). *J. Memb. Sci.* 427, 472–478 (2013).
204. Xu, L., Rungta, M. & Koros, W. J. Matrimid® derived carbon molecular sieve hollow fiber membranes for ethylene/ethane separation. *J. Memb. Sci.* 380, 138–147 (2011).
205. Hou, J. *et al.* Carbon Nanotube Networks as Nanoscaffolds for Fabricating Ultrathin Carbon Molecular Sieve Membranes. *ACS Appl. Mater. Interfaces* 10, 20182–20188 (2018).
206. Ogieglo, W., Puspasari, T., Ma, X. & Pinnau, I. Sub-100 nm carbon molecular sieve membranes from a polymer of intrinsic microporosity precursor: Physical aging and near-equilibrium gas separation properties. *J. Memb. Sci.* 597, 117752 (2020).
207. Ogieglo, W. *et al.* Thin Composite Carbon Molecular Sieve Membranes from a Polymer of Intrinsic Microporosity Precursor. *ACS Appl. Mater. Interfaces* 11, 18770–18781 (2019).
208. Turchanin, A. & Götzhäuser, A. Carbon Nanomembranes. *Advanced Materials* 28, 6075–6103 (2016).
209. Yang, Y. *et al.* Ultrahigh Ionic Exclusion through Carbon Nanomembranes. *Adv. Mater.* 32, 1907850 (2020).
210. Angelova, P. *et al.* A universal scheme to convert aromatic molecular monolayers into functional carbon nanomembranes. *ACS Nano* 7, 6489–6497 (2013).
211. Turchanin, A. *et al.* Conversion of self-assembled monolayers into nanocrystalline graphene: Structure and electric transport. *ACS Nano* 5, 3896–3904 (2011).
212. Ai, M. *et al.* Carbon Nanomembranes (CNMs) Supported by Polymer: Mechanics and Gas Permeation. *Adv. Mater.* 26, 3421–3426 (2014).
213. Rao, M. B. & Sircar, S. Nanoporous carbon membranes for separation of gas mixtures by selective surface flow. *J. Memb. Sci.* 85, 253–264 (1993).
214. Yoshimune, M., Yamamoto, T., Nakaiwa, M. & Haraya, K. Preparation of highly mesoporous carbon membranes via a sol-gel process using resorcinol and formaldehyde.

- Carbon*, 46, 1031–1036 (2008).
215. Wang, X., Zhu, Q., Mahurin, S. M., Liang, C. & Dai, S. Preparation of free-standing high quality mesoporous carbon membranes. *Carbon* 48, 557–560 (2010).
 216. Tanaka, S., Nakatani, N., Doi, A. & Miyake, Y. Preparation of ordered mesoporous carbon membranes by a soft-templating method. *Carbon*, 49, 3184–3189 (2011).
 217. Li, J. *et al.* Fabrication of ordered mesoporous carbon hollow fiber membranes via a confined soft templating approach. *J. Mater. Chem. A* 2, 4144–4149 (2014).
 218. Qin, G., Wang, C. & Wei, W. Preparation of a mesoporous carbon membrane from resorcinol and formaldehyde. *Carbon* 48, 4206–4208 (2010).
 219. Liang, C., Li, Z. & Dai, S. Mesoporous carbon materials: Synthesis and modification. *Angew. Chemie - Int. Ed.* 47, 3696–3717 (2008).
 220. Knudsen, M. & Partington, J. R. The Kinetic Theory of Gases. Some Modern Aspects. *J. Phys. Chem.* 39, 307–307 (1935).
 221. Rodriguez, A. T., Li, X., Wang, J., Steen, W. A. & Fan, H. Facile synthesis of nanostructured carbon through self-assembly between block copolymers and carbohydrates. *Adv. Funct. Mater.* 17, 2710–2716 (2007).
 222. Suk, J. W. *et al.* Transfer of CVD-grown monolayer graphene onto arbitrary substrates. *ACS Nano* 5, 6916–6924 (2011).
 223. Giordano, L., Gubis, J., Bierman, G. & Kapteijn, F. Conceptual design of membrane-based pre-combustion CO₂ capture process: Role of permeance and selectivity on performance and costs. *J. Memb. Sci.* 575, 229–241 (2019).
 224. Lin, H. *et al.* CO₂-selective membranes for hydrogen production and CO₂ capture - Part II: Techno-economic analysis. *J. Memb. Sci.* 493, 794–806 (2015).
 225. Micari, M., Dakhchoune, M. & Agrawal, K. V. Techno-economic assessment of postcombustion carbon capture using high-performance nanoporous single-layer graphene membranes. *J. Memb. Sci.* 624, (2021).
 226. Evans, K. & Xu, T. Self-Assembly of Supramolecular Thin Films: Role of Small Molecule and Solvent Vapor Annealing. *Macromolecules* 52, 639–648 (2019).
 227. Liang, C., Hong, K., Guiochon, G. A., Mays, J. W. & Dai, S. Synthesis of a large-scale highly ordered porous carbon film by self-assembly of block copolymers. *Angew. Chemie - Int. Ed.* 43, 5785–5789 (2004).
 228. Sidorenko, A., Tokarev, I., Minko, S. & Stamm, M. Ordered reactive nanomembranes/nanotemplates from thin films of block copolymer supramolecular assembly. *J. Am. Chem. Soc.* 125, 12211–12216 (2003).
 229. Kim, S. H., Misner, M. J., Xu, T., Kimura, M. & Russell, T. P. Highly oriented and ordered arrays from block copolymers via solvent evaporation. *Adv. Mater.* 16, 226–231 (2004).
 230. Vukovic, I., Ten Brinke, G. & Loos, K. Hexagonally perforated layer morphology in PS-b-

- P4VP(PDP) supramolecules. *Macromolecules* 45, 9409–9418 (2012).
231. Valkama, S. *et al.* Self-assembled structures in diblock copolymers with hydrogen-bonded amphiphilic plasticizing compounds. *Macromolecules* 39, 9327–9336 (2006).
 232. Kowalewski, T., Tsarevsky, N. V. & Matyjaszewski, K. Nanostructured carbon arrays from block copolymers of polyacrylonitrile. *J. Am. Chem. Soc.* 124, 10632–10633 (2002).
 233. Kim, C. H., Lee, D. K. & Pinnavaia, T. J. Graphitic mesostructured carbon prepared from aromatic precursors. *Langmuir* 20, 5157–5159 (2004).
 234. Peng, W. chao, Chen, Y. & Li, X. yan. MoS₂/reduced graphene oxide hybrid with CdS nanoparticles as a visible light-driven photocatalyst for the reduction of 4-nitrophenol. *J. Hazard. Mater.* 309, 173–179 (2016).
 235. Park, J. *et al.* A facile synthesis tool of nanoporous carbon for promising H₂, CO₂, and CH₄ sorption capacity and selective gas separation. *J. Mater. Chem. A* 6, 23087–23100 (2018).
 236. Aguilar-Bolados, H. *et al.* Facile and Scalable One-Step Method for Amination of Graphene Using Leuckart Reaction. *Chem. Mater.* 29, 6698–6705 (2017).
 237. Celebi, K. *et al.* Ultimate permeation across atomically thin porous graphene. *Science*, 344, 289–292 (2014).
 238. Kim, H. W. *et al.* Selective Gas Transport Through Few-Layered Graphene and Graphene Oxide Membranes. *Science*, 342, 91–95 (2013).
 239. Nagai, K., Higuchi, A. & Nakagawa, T. Gas permeability and stability of poly(1-trimethylsilyl-1-propyne-co-1-phenyl-1-propyne) membranes. *J. Polym. Sci. Part B Polym. Phys.* 33, 289–298 (1995).
 240. Rezac, M. E. & Schöberl, B. Transport and thermal properties of poly(ether imide)/acetylene-terminated monomer blends. *J. Memb. Sci.* 156, 211–222 (1999).
 241. Shekhawat, D., Luebke, D. R. & Pennline, H. W. *A Review of Carbon Dioxide Selective Membranes: A Topical Report.* (2003). doi:10.2172/819990
 242. Tang, Z., Dong, J. & Nenoff, T. M. Internal surface modification of MFI-type zeolite membranes for high selectivity and high flux for hydrogen. *Langmuir* 25, 4848–4852 (2009).
 243. Li, Y., Liang, F., Bux, H., Yang, W. & Caro, J. Zeolitic imidazolate framework ZIF-7 based molecular sieve membrane for hydrogen separation. *J. Memb. Sci.* 354, 48–54 (2010).
 244. de Vos, R. M. High-Selectivity, High-Flux Silica Membranes for Gas Separation. *Science*, 279, 1710–1711 (1998).
 245. Guo, H., Zhu, G., Hewitt, I. J. & Qiu, S. “Twin Copper Source” Growth of Metal–Organic Framework Membrane: Cu₃(BTC)₂ with High Permeability and Selectivity for Recycling H₂. *J. Am. Chem. Soc.* 131, 1646–1647 (2009).
 246. Elyassi, B., Sahimi, M. & Tsotsis, T. T. Silicon carbide membranes for gas separation applications. *J. Memb. Sci.* 288, 290–297 (2007).

247. Hori, T., Mizuno, M. & Shimizu, T. Dye diffusion in water-swollen cellulose membranes and in bulk water. *Colloid Polym. Sci. Kolloid-Zeitschrift Zeitschrift für Polym.* 258, 1070–1076 (1980).
248. Lee, W.-C. *et al.* Centimeter-scale gas-sieving nanoporous single-layer graphene membrane. *J. Memb. Sci.* 618, (2021).
249. Liu, M., Gurr, P. A., Fu, Q., Webley, P. A. & Qiao, G. G. Two-dimensional nanosheet-based gas separation membranes. (2018). doi:10.1039/c8ta09070j
250. Chen, Z. *et al.* In situ generation of highly dispersed metal nanoparticles on two-dimensional layered SiO₂ by topotactic structure conversion and their superior catalytic activity. *Appl. Surf. Sci.* 434, 1137–1143 (2018).
251. Hao, J., Cui, Z. M., Cao, C. Y. & Song, W. A Pd/silica composite with highly uniform Pd nanoparticles on silica lamella via layered silicate. *Chem. Phys. Lett.* 658, 88–91 (2016).
252. Chen, Z. *et al.* Layered silicate RUB-15 for efficient removal of UO₂²⁺ and heavy metal ions by ion-exchange. *Environ. Sci. Nano* 4, 1851–1858 (2017).
253. Di Iorio, J. R., Johnson, B. A. & Román-Leshkov, Y. Ordered hydrogen-bonded alcohol networks confined in lewis acid zeolites accelerate transfer hydrogenation turnover rates. *J. Am. Chem. Soc.* 142, 19379–19392 (2020).
254. Bregante, D. T. *et al.* Cooperative effects between hydrophilic pores and solvents: Catalytic consequences of hydrogen bonding on alkene epoxidation in zeolites. *J. Am. Chem. Soc.* 141, 7302–7319 (2019).
255. Vega-Vila, J. C., Harris, J. W. & Gounder, R. Controlled insertion of tin atoms into zeolite framework vacancies and consequences for glucose isomerization catalysis. *J. Catal.* 344, 108–120 (2016).
256. Luo, Y. *et al.* Two-Dimensional MoS₂ Confined Co(OH)₂ Electrocatalysts for Hydrogen Evolution in Alkaline Electrolytes. *ACS Nano* 12, 4565–4573 (2018).
257. Boscoboinik, J. A. Chemistry in confined space through the eyes of surface science - 2D porous materials. *J. Phys. Condens. Matter* 31, (2019).



Dakhchoune

Mostapha

Ph.D. Material Science - Chemical Engineering

REASEARCH SKILLS

Characterization

SEM, TEM, EDX, XRD (in/out-of-plane, GID, XRR), NMR, MAS SS NMR, UV-Vis, FT-IR, Gas sorption Chemisorption

Advanced skills

High-Resolution TEM, Focused Ion Beam, building of home-made setups for liquid and gas separation testing

Thin film preparation

Knowledge of multiple coating techniques (spin-coating, vacuum-pressure filtration, hot-drop coating, layer-by-layer deposition, Langmuir-Blodgett and Schaefer, dip-coating)

Synthesis skills

Low pressure/atmospheric chemical vapor deposition of single layer graphene on copper and nickel foil catalysts. Hydrothermal synthesis of zeolites. Non-Solvent Induced Phase Separation (NIPS) to fabricate polymeric supports with 20 nm average pore size



mostapha.dakhchoune@epfl.ch



+39 320 69815277

+41 779 77 43 52



Rue du Scex, 18, Sion, Valais, CH



Italian Citizen



November, 2nd, 1989



mosta.dakhchoune



linkedin.com/in/dakhchoune

LANGUAGES

	Basic	Fluent	Mother tongue
English			
Italian			
Arabic			
French			
Spanish			

SOFTWARES

Aspen Plus	Inkscape
Aspen Hysys	Microsoft
Matlab	Office 3D max
Python	UiPath
AutoCad	OriginPro

AWARDS

Swiss Chemical Society Best poster prize award (September 2019, Zurich, Switzerland)

EDUCATION

12/16-05/21	<i>Ph.D Fellow in Material science and Chemical Engineering</i> École Polytechnique Fédérale de Lausanne (EPFL) Advisor: Kumar Varoon Agrawal Thesis: Two-dimensional atomically bridged nanoporous silicate-based membranes for gas separation
10/13-03/16	<i>M.S, Chemical and Process Engineering</i> Alma Mater Studiorum University of Bologna Advisors: Prof. Giulio Cesare Sarti and Prof. Ingo Pinnau King Abdullah University of Science and Technology (KAUST University) Thesis: polymeric membranes-based polyimides for the natural gas separation. GPA: 4/4
10/09-02/13	<i>B.S., Environmental Engineering</i> University of Florence Advisor: Claudio Lubello Civil and Environmental Engineering Department Thesis: Reactor aspects of fungal biomass for the treatment of waste from the rubber industry. GPA: 4/4

TEACHING ACTIVITIES

- Math-101 Analys I (EPFL)
- ChE-409 Chemical Engineering lab (EPFL)
- ChE-310 Fundamentals of separations (EPFL)
- ChE-402 Advanced diffusion processes (EPFL)

WORK EXPERIENCE

Stagiaire

09/16-12/16 Andreotti Impianti, Florence, Italy
Project manager Assistant, engineering office,
Design of oilseeds, edible oil, and oleochemicals plants

Internship

09/15-03/16 Kaust University, Thuwal, Saudi Arabia
Department of advanced membranes porous materials center
Working in the development and testing of polymeric membranes-based polyimides for the natural gas separation

Intership

01/09-02/09 The Menarini Group, pharmaceutical industry, Florence Italy
Research objective: Chemical and physical investigation of drugs

Waiter

01/06-10/16 To sustain my studies tuition fees, I have worked for 10 years as waiter in the following restaurants in Florence: Hotel Demidoff, Bistrot Gilda, Malafemmina Restaurant

PUBLICATIONS

L. F. Villalobos, C. V. Goethem, K.-J.g Hsu, M. Moradi, K. Zhao, M. Dakhchoune, S. Huang, Y. Shen, E. Oveisi, V. Boureau, A. Bornet, K. V. Agrawal, "Bottom-up synthesis of films hosting atom-thick molecular-sieving apertures", *Proceedings of the National Academy of Sciences*, just accepted.

M. Micari, M. Dakhchoune, K. V. Agrawal, "Techno-economic assessment of postcombustion carbon capture using high-performance nanoporous single-layer graphene membranes", *Journal of Membrane Science*, 2021, 624, 119103 [Link to publication](#)

S. Huang, S. Li, L. F. Villalobos, M. Dakhchoune, D. J. Babu, M. T. Vahdat, M. Mensi, E. Oveisi, K. V. Agrawal, "Millisecond lattice gasification for high-density CO₂- and O₂-sieving nanopores in single-layer graphene", *Science Advances*, DOI: 10.1126/sciadv.abf0116 [Link to publication](#)

L. F. Villalobos, S. Huang, M. Dakhchoune, G. He, W.-C. Lee, K. V. Agrawal, "Polybenzimidazole copolymer derived lacey carbon film for graphene transfer and contamination removal strategies for imaging graphene nanopores", *Carbon* 173 (2021) 980-988 [link to publication](#)

M. Dakhchoune, L. F. Villalobos, R. Semino, L. Liu, M. Rezaei, P. Schouwink, C. E. Avalos, P. Baade, V. Wood, Y. Han, M. Ceriotti, K. V. Agrawal, "Gas sieving zeolitic membranes by the condensation of precursor nanosheets", *Nature Materials*, 2020, doi: 10.1038/s41563-020-00822-2 [link to publication](#)

W. Lee, L. Bondaz, S. Huang, G. He, M. Dakhchoune, K. V. Agrawal, "Centimeter-Scale Gas- Sieving Nanoporous Single-Layer Graphene Membrane", *Journal of Membrane Science*, 618, 118745, 2021 [link to publication](#)

M. Li, A. Borsay, M. Dakhchoune, K. Zhao, W. Luo, A. Züttel, "Thermal stability of size- selected copper nanoparticles: Effect of size, support, and CO₂ hydrogenation atmosphere", *Applied Surface Science*, 2020, 510, 145439 [link to publication](#)

M. Dakhchoune, “Two-dimensional material membranes for gas separation”, *Chimia*, 74, 4, 263-269 [link to publication](#)

L. F. Villalobos, M. T. Vahdat, M. Dakhchoune, Z. Nadizadeh, M. Mensi, E. Oveisi, D. Campi, N. Marzari, K. V. Agrawal, “Large scale synthesis of crystalline g-C₃N₄ Single-layer nanosheets and high-temperature H₂ sieving from assembled films”, *Science Advances*, 6, 1, eaay9851, 2020 [link to publication](#)

M. H. Khan, M. Moradi, M. Dakhchoune, M. Rezaei, S. Huang, J. Zhao, K. V. Agrawal, “Hydrogen Sieving from Intrinsic Defects of Benzene- Derived Single-Layer Graphene”, *Carbon*, 2019, 153, 458-456 [link to publication](#)

J. Zhao, G. He, S. Huang, L. F. Villalobos, M. Dakhchoune, H. Bassas, E. Oveisi, K. V. Agrawal, “Etching gas-sieving nanopores in single-layer graphene with an angstrom precision for high-performance gas mixture separation”, *Science Advances*, 5, 1, eaav1851, 2019 [link to publication](#)

S. Huang, M. Dakhchoune, W. Luo, E. Oveisi, G. He, M. Rezaei, J. Zhao, A. Züttel, M. S. Strano, K. V. Agrawal, “Large-area single-layer graphene membranes by crack-free transfer for gas mixture separation”, *Nature Communications*, 9, 2632, 2018 [link to publication](#)

G. He., M. Dakhchoune, J. Zhao, S. Huang, K. V. Agrawal, “Electrophoretic Nuclei Assembly for Crystallization of High-Performance Membranes on Unmodified Supports”, *Advanced Functional Materials*, 28, 1707427, 2018 [link to publication](#)

M. Dakhchoune, S. Huang, G. He, N. Dudani and K. V. Agrawal, “Ultrahigh flux gas-selective nanoporous carbon membrane and manufacturing method thereof”, WO2018/177533A1 [Patent].

Sion, June 2021

